

**DIGITAL AND OPTICAL COMPENSATION OF SIGNAL
IMPAIRMENTS FOR OPTICAL COMMUNICATION
RECEIVERS**

ADAICKALAVAN MEIYAPPAN

NATIONAL UNIVERSITY OF SINGAPORE

2014

**DIGITAL AND OPTICAL COMPENSATION OF SIGNAL
IMPAIRMENTS FOR OPTICAL COMMUNICATION
RECEIVERS**

ADAICKALAVAN MEIYAPPAN

(B.Eng.(Hons.), National University of Singapore, Singapore)

A THESIS SUBMITTED

FOR THE DEGREE OF DOCTOR OF PHILOSOPHY

DEPARTMENT OF ELECTRICAL AND COMPUTER ENGINEERING

NATIONAL UNIVERSITY OF SINGAPORE

2014

Declaration

I hereby declare that this thesis is my original work and it has been written by me in its entirety. I have duly acknowledged all the sources of information which have been used in the thesis.

This thesis has also not been submitted for any degree in any university previously.

Adaickalavan Meiyappan
1 August 2014

Acknowledgments

Foremost, I would like to express my sincere gratitude and appreciation to my Ph.D. supervisor Prof. Pooi-Yuen Kam. I am greatly indebted for the research wisdom he imparted and his invaluable guidance throughout my candidature. His countless hours spent in our research discussions helped shape this thesis.

Special thanks to Dr. Hoon Kim, who previously co-supervised my research and continuously provided helpful advice. I immensely benefited from his vast knowledge in experimental optical communications. His deep insights, into the practical aspects in research, which he shared with me improved the contributions of this thesis.

Additionally, I would like to thank my thesis committee members for their time in reviewing this work.

I gratefully acknowledge the President's Graduate Fellowship award from National University of Singapore, supported by the Singapore MoE under AcRF Tier 2 Grant MOE2010-T2-1-101, for funding this postgraduate study.

Finally, my heartfelt thanks to my parents, sister, brother-in-law, and nephew, whose unconditional support saw me through to the end of a fruitful four years of doctoral endeavor.

Contents

Declaration	i
Acknowledgments	ii
Contents	iii
Summary	iv
List of Tables	v
List of Figures	vi
List of Abbreviations	vii
1 Introduction	1
1.1 Long Haul Transmission	1
1.2 Access Networks	4
1.3 Research Contributions	8
1.4 Thesis Outline	9
2 Coherent Optical Systems	11
2.1 Modulation Formats	11
2.1.1 Several 4-, 8-, and 16-Point Constellations	11
2.1.2 BER Performance	13

2.1.3	Differential Encoding Technique	14
2.2	Coherent Optical Transmission System	16
2.2.1	Transmitter	16
2.2.2	Channel	18
2.2.3	Receiver	19
2.3	Frequency and Phase Estimators	28
2.3.1	Fast Fourier Transform based Frequency Estimator	29
2.3.2	Differential Frequency Estimator	30
2.3.3	Block M th Power Phase Estimator	30
2.3.4	Blind Phase Search	32
2.3.5	Decision-Aided Maximum-Likelihood Phase Estimator	33
3	Complex-Weighted Decision-Aided Maximum-Likelihood Phase and Frequency Estimation	35
3.1	CW-DA-ML Estimator	35
3.1.1	Principle of Operation	36
3.1.2	Implementation	38
3.1.3	Mean-Square Error Learning Curve	40
3.1.4	Adaptation of Filter Weights	42
3.1.5	Optimum Filter Length	44
3.2	Performance Analysis	46
3.2.1	Laser Linewidth Tolerance	46
3.2.2	Frequency Offset Tolerance	48
3.2.3	Acquisition Time, Accuracy, and SNR Threshold	50
3.2.4	Continuous versus Periodic Tracking	53
3.2.5	Cycle Slip Probability	55
3.3	Pilot-Assisted Carrier Estimation	59

3.4	Time-Varying Frequency Offset	61
3.5	ADC Resolution	62
3.6	Conclusion	63
4	Adaptive Complex-Weighted Decision-Aided Phase and Frequency Estimation	64
4.1	Principle of Operation	66
4.2	Adaptation of Effective Filter Length	68
4.3	Performance in Presence of Linear Phase Noise	70
4.3.1	Laser Linewidth and Frequency Offset Tolerance	71
4.3.2	Cycle Slip Probability	72
4.4	Performance in Presence of Nonlinear Phase Noise	74
4.4.1	BER Performance	75
4.4.2	Cycle Slip Probability	76
4.5	Complexity Analysis	78
4.6	Conclusion	81
5	Intensity-Modulated Direct-Detection Radio-over-Fiber System	84
5.1	Experimental Setup	85
5.2	BER Performance	87
5.3	Performance Improvement by DI	88
5.3.1	Optical Filter	89
5.3.2	Positive Chirp	90
5.4	Rayleigh Backscattering	92
5.5	Single Sideband Generation	93
5.5.1	Chromatic Dispersion Induced RF Power Fading	93
5.5.2	Sideband Suppression by DI	95
5.6	Tolerable RF Carrier Frequencies and Frequency Offsets	97

5.7 Conclusion	98
6 Conclusion	100
6.1 Summary of Main Contributions	100
6.2 Suggestions for Future Research	102
6.2.1 Carrier Estimators for Space-Division Multiplexed Systems . .	102
6.2.2 Equalizers with Adaptive Filter Length	102
6.2.3 Phase-Modulated Coherent Detection RoF System	103
A Derivation of DA-ML Phase Estimator	106
B Derivation of \hat{w} in CW-DA-ML	109
C Recursive Update of \hat{w} in CW-DA-ML	111
D Derivation of \hat{w} in Adaptive CW-DA Estimator	114
Bibliography	116
List of Publications	131

Summary

Three new receiver designs, incorporating novel digital and optical signal processing solutions, are presented for fiber-optic communication in long-haul transmissions and access networks. Firstly, a complex-weighted decision-aided maximum-likelihood joint phase noise and frequency offset estimator is derived for coherent receivers in long-haul transmissions. It achieves fast carrier acquisition, complete frequency estimation range, low cycle slip probability, low signal-to-noise ratio (SNR) operability, requires no phase unwrapping, reliably tracks time-varying frequency, and is format transparent. Additionally, the resilience of several 4-, 8-, and 16-point constellations to phase rotation and cycle slips are investigated. Secondly, the need for carrier estimators with adaptive filter lengths in coherent receivers is studied. An adaptive complex-weighted decision-aided carrier estimator is introduced, whose effective filter length automatically adapts according to the SNR, laser-linewidth-per-symbol-rate, nonlinear phase noise, and modulation format, with no preset parameters required. Besides bit-error rate, choice of filter length also affects the cycle slip probability. Thirdly, a direct-detection receiver incorporating a passive optical delay interferometer is proposed for radio-over-fiber optical backhaul employing reflective semiconductor optical amplifier (RSOA) in broadband wireless access networks. Effectiveness of the receiver in alleviating the constrained modulation bandwidth, limited transmission distance, and radio frequency signal fading, is assessed through an upstream transmission of a 2-Gb/s 6-GHz radio signal in loopback-configured network using a directly modulated RSOA.

List of Tables

2.1	SNR per bit values at $\text{BER} = 10^{-3}$	15
3.1	Symbol-by-symbol receiver employing CW-DA-ML	39
3.2	Optimal filter length for 1-dB γ_b penalty at $\text{BER} = 10^{-3}$	45
3.3	$\Delta\nu T_b$ tolerance for 1-dB γ_b penalty at $\text{BER} = 10^{-3}$	47
3.4	ΔfT tolerance for 1-dB γ_b penalty at $\text{BER} = 10^{-3}$ and $\Delta\nu = 0$	49
3.5	Carrier acquisition time	52
4.1	System parameter values used in evaluating the nonlinear phase noise and cycle slip tolerance	75
4.2	Coordinates of points at $\text{BER} = 2.5 \times 10^{-2}$ in Fig. 4.8	77
4.3	Complexity comparison of carrier estimators	79
4.4	Complexity of carrier estimators using representative parameter values	82

List of Figures

1.1	Principle of upstream transmission in an IMDD WDM RoF system.	5
1.2	Schematic diagram of an RSOA.	6
2.1	Signal constellation and bits-to-symbol mapping for (a) QPSK, (b) 8-QAM, (c) 8-PSK, (d) 16-QAM, (e) 16-Star, and (f) 16-PSK.	12
2.2	BER performance in AWGN channel with and without differential encoding.	14
2.3	Polarization multiplexed coherent optical system.	17
2.4	Fast Fourier transform based frequency estimator.	29
2.5	Differential frequency estimator.	30
2.6	Block M th power phase estimator.	31
2.7	Blind phase search estimator.	32
2.8	DA-ML phase estimator.	33
3.1	CW-DA-ML estimator.	38
3.2	Learning curves for CW-DA-ML with different values of Δf and SNR.	40
3.3	Adaptation of steady-state filter weights to different γ_b , $\Delta\nu T_b$, and $\Delta f T$.	43
3.4	SNR per bit penalty of CW-DA-ML at $\text{BER} = 10^{-3}$ versus $\Delta\nu T_b$ and filter length for (a) QPSK, (b) 8-QAM, (c) 8-PSK, (d) 16-QAM, (e) 16-Star, and (f) 16-PSK.	44
3.5	SNR per bit penalty of DiffFE-MPE at $\text{BER} = 10^{-3}$ versus $\Delta\nu T_b$ and filter length for (a) QPSK, (b) 8-PSK, (c) 16-QAM, and (d) 16-PSK.	45

3.6	Laser linewidth tolerance of carrier estimators for (a) 4-, (b) 8-, and (c) 16-point constellations.	46
3.7	Laser linewidth tolerance of 16-QAM and 16-Star, using CW-DA-ML.	47
3.8	Frequency offset tolerance of carrier estimators for (a) 4-, (b) 8-, and (c) 16-point constellations.	48
3.9	Frequency acquisition time and accuracy of FFTFE-MPE, DiffFE-MPE, and CW-DA-ML for (a) QPSK, (b) 8-QAM, and (c) 16-QAM.	51
3.10	Error variance versus γ_b with different sample size N for frequency estimation in (a) QPSK, (b) 8-QAM, and (c) 16-QAM.	54
3.11	Cycle slip in CW-DA-ML for (a) 16-QAM, and (b) 16-PSK signals.	56
3.12	Cycle slip probability of CW-DA-ML and DiffFE-MPE for QPSK signal versus (a) $\Delta\nu T_b$, and (b) γ_b	56
3.13	Cycle slip probability of DiffFE-MPE versus $\Delta\nu T_b$	57
3.14	Cycle slip probability of different modulation formats versus $\Delta\nu T_b$	58
3.15	SNR per bit penalty versus data length D , at different pilot lengths P , for (a) QPSK, (b) 8-QAM, and (c) 16-QAM.	60
3.16	BER performance of PA CW-DA-ML with ideal and actual decision feedback.	60
3.17	BER performance of PA CW-DA-ML in time-varying frequency offset experiencing (a) continuous drift, and (b) rapid jumps.	61
3.18	ADC resolution in terms of number of bits for differentially-encoded CW-DA-ML.	62
4.1	Adaptive CW-DA estimator.	67
4.2	Adaptation of the (a) magnitude of weights, $ \hat{w}_i $, and (b) phase of weights, $\arg(\hat{w}_i)$	68
4.3	BER performance of adaptive CW-DA estimator.	70
4.4	(a) Laser linewidth tolerance, with $\Delta fT = 0.1$. (b) Frequency offset tolerance, with $\Delta\nu T = 7 \times 10^{-5}$	71
4.5	Cycle slip probability versus $\Delta\nu T$ for different filter lengths.	72
4.6	Required SNR and corresponding cycle slip probability at BER = 2.5×10^{-2}	73

List of Figures

4.7	BER performance of carrier estimators in nonlinear phase noise.	76
4.8	Cycle slip probability of carrier estimators in nonlinear phase noise.	77
5.1	Experimental setup for upstream transmission of BPSK radio signals.	86
5.2	RSOA's measured (a) frequency response, and (b) L/I characteristic.	86
5.3	Measured BER as a function of OMI for 0-, 20-, 30-, and 40-km transmission over SSMF.	88
5.4	Schematic diagram of a DI.	89
5.5	Optical waveform of the radio signal captured at the input to the PIN-FET receiver (a) without DI, and (b) with DI.	90
5.6	Propagation of intensity modulated optical pulses which are (a) unchirped, (b) negatively chirped, and (c) positively chirped.	91
5.7	Effects of Rayleigh backscattering in RoF systems.	92
5.8	CD-induced RF power fading in a DSB signal.	93
5.9	RF power degradation at the receiver for optical DSB modulation as a function of (a) fiber length and (b) RF frequency.	94
5.10	Optical spectra of the signal before and after DI.	95
5.11	RF tone fading measurement setup.	96
5.12	Relative RF power of a 6-GHz sinusoidal wave as a function of transmission distance over SSMF.	96
5.13	RF carrier frequency tolerance.	97
5.14	Tolerance of frequency offset between the DI and laser diode when the RF carrier frequency is 6 GHz.	98
6.1	Phase-modulated RoF link with coherent detection.	104

List of Abbreviations

ADC	Analog-to-digital converter
APD	Avalanche photodiode
AR	Anti reflector
ASE	Amplified spontaneous emission
ASIC	Application specific integrated circuit
AWG	Arrayed waveguide grating
AWGN	Additive white Gaussian noise
BPS	Blind phase search
BPSK	Binary phase-shift keying
C-LSB	Carrier-LSB
C-USB	Carrier-USB
CD	Chromatic dispersion
CO	Central office
CRLB	Cramer-Rao lower bound
CW	Continuous wave
CW-DA	Complex-weighted decision-aided
CW-DA-ML	Complex-weighted decision-aided maximum-likelihood
DA-ML	Decision-aided maximum-likelihood
DCF	Dispersion-compensating fiber
DFB	Distributed feedback

List of Abbreviations

DGD	Differential group delay
DiffFE	Differential frequency estimator
DI	Delay interferometer
DOF	Degree of freedom
DPSK	Differential phase-shift keying
DSB	Double sideband
DSP	Digital signal processing
EDFA	Erbium-doped fiber amplifier
FEC	Forward error correction
FET	Field-effect transistor
FFT	Fast Fourier transform
FFTFE	Fast Fourier transform based frequency estimator
FIR	Finite impulse response
FSE	Fractionally spaced equalizer
GVD	Group velocity dispersion
HR	High reflector
IMDD	Intensity-modulated direct detection
ISI	Intersymbol interference
LO	Local oscillator
LSB	Lower-frequency sideband
MC	Monte Carlo
MPE	Block M th power phase estimator
MPSK	M -ary phase-shift keying
MQAM	M -ary quadrature amplitude modulation
MSE	Mean-square error
MZM	Mach-Zehnder modulator

List of Abbreviations

NDA	Non-data aided
NRZ	Non-return to zero
OBPF	Optical band-pass filter
OMI	Optical modulation index
OOK	On-off keying
OPS	Optical packet switching
PA	Pilot assisted
PBS	Polarization beam splitter
PDF	Probability density function
PDM	Polarization-division multiplexed
PIN	<i>p-i-n</i>
PLL	Phase-locked loop
PMD	Polarization-mode dispersion
PSK	Phase-shift keying
PSP	Principle states of polarization
QAM	Quadrature amplitude modulation
QPSK	Quaternary phase-shift keying
RBS	Remote base station
RF	Radio frequency
RoF	Radio over fiber
ROM	Read-only memory
RSOA	Reflective semiconductor optical amplifier
SD	Soft decision
SDM	Space-division multiplexing
SNR	Signal-to-noise ratio
SPM	Self-phase modulation

List of Abbreviations

SSB	Single sideband
SSMF	Standard single-mode fiber
SSR	Sideband suppression ratio
TDD	Turbo differential decoding
TO	Transistor outlook
Tx	Transmitter
USB	Upper-frequency sideband
WDM	Wavelength-division multiplexed
WGR	Waveguide grating router

Chapter 1

Introduction

Invention of laser by T. H. Maiman (Hughes Research Laboratories, USA) in 1960 [1] and proposition of optical fiber as the transmission medium of choice by K. C. Kao (Standard Telecommunication Laboratories, UK) in 1966 [2] started the optical communications era. Applications of optical communication in long haul transmission and access networks are considered in this thesis. The challenges in signal reception are studied, and addressed using novel digital and optical signal processing techniques in the receiver.

1.1 Long Haul Transmission

Long haul optical communication systems aim for bit rates per channel in excess of 100 Gb/s as the next interface rates are geared toward 400 Gb/s and 1 Tb/s [3, 4]. Increasing the transmission capacity, to service the growth of data traffic, at a fixed optical amplification bandwidth requires increasing the spectral efficiency. Most long-haul transmission systems are limited by inline optical amplifier noise, which is additive white Gaussian noise (AWGN) in nature [5]. The ultimate spectral efficiency for a bandwidth and power constrained AWGN channel given by Shannon's capacity

1.1 Long Haul Transmission

is [6, 7]

$$SE = \frac{B_s}{B_c} \log_2(1 + \gamma_s) \text{ bits/s/Hz} \quad (1.1)$$

where B_s/B_c is the ratio of signal bandwidth to channel bandwidth and γ_s is the signal-to-noise ratio (SNR) per symbol.

Binary modulation which encodes one bit per symbol, such as on-off keying (OOK) with direct detection or binary differential phase-shift keying (DPSK) with interferometric detection, only achieves a spectral efficiency of 0.8 bits/s/Hz per polarization [8]. Noncoherent detection with OOK and binary DPSK are attractive only at spectral efficiencies below 1 bit/s/Hz per polarization [9].

Moving to nonbinary modulations, we have optically amplified unconstrained intensity-modulated direct-detection (IMDD) systems with an asymptotic spectral efficiency of $0.5 \log_2(\gamma_s) - 0.5$ [5, 10, 11]. However, the asymptotic spectral efficiency for a constant-intensity constrained modulation, such as M -ary phase-shift keying (MPSK), with coherent detection can reach [12–14]

$$SE \sim 0.5 \log_2(\gamma_s) + 1.10 \text{ bits/s/Hz.} \quad (1.2)$$

Although both IMDD and constant-intensity modulation has only one degree of freedom (DOF) per polarization for encoding, the coherent system outperforms the non-coherent IMDD in an optical amplifier noise limited system by a spectral efficiency of 1.6 bits/s/Hz at large SNR [5]. Achievable spectral efficiencies of both IMDD and constant intensity modulation are approximately halved compared to Eq. (1.1) due to discarding of one DOF, namely, the phase and field intensity, respectively.

Further increase in spectral efficiency requires higher level modulation with coherent detection which allows information to be encoded in all four available DOF, namely, two optical field quadratures and two polarizations. Quaternary phase-shift keying (QPSK) has been suggested as the most attractive modulation for spectral effi-

1.1 Long Haul Transmission

ciency between 1 and 2 bits/s/Hz, whereas 8 phase-shift keying (PSK) and 16 quadrature amplitude modulation (QAM) are necessary for spectral efficiencies beyond 2 bits/s/Hz per polarization [9]. Coherent detection promises superior spectral efficiency, receiver sensitivity, and transmission distance compared to noncoherent systems [15], and enables the attainment of Shannon's capacity with the use of coding such as Turbo codes [16–18].

A major impediment in homodyne coherent detection is the synchronization of the local oscillator (LO) laser to the optical carrier of the received optical signal. The received signal can be perturbed by phase noise arising from nonzero laser linewidth $\Delta\nu$ and frequency offset Δf between the transmitter and LO lasers. Laser linewidth can range from the order of 10 kHz for external-cavity tunable lasers [19] and fiber lasers [20] to 10 MHz for distributed feedback (DFB) lasers [21]. Typical tunable lasers can have a frequency error of up to ± 2.5 GHz over their lifetime, leading to a possible frequency offset Δf as large as 5 GHz [22].

Traditionally, phase-locked loop (PLL) was employed for coherent demodulation of optical signals [23–25]. However, PLL is sensitive to loop propagation delay which can cause loop instability [21]. Loop delay greater than the bit duration T_b becomes nonnegligible and severely constraints the permissible laser linewidth-per-bit-rate $\Delta\nu T_b$ [26]. Moreover, PLL has a limited frequency-offset-per-symbol-rate $\Delta f T$ estimation range [27]. The tolerable $\Delta f T$ by PLL in 16-QAM signals was limited to 1.43×10^{-3} at $\Delta\nu T_b = 3.57 \times 10^{-6}$ [28], to 2.5×10^{-3} at $\Delta\nu T_b = 2.5 \times 10^{-6}$ [29] in experiments, and to 10^{-2} in simulation at $\Delta\nu T_b = 1.79 \times 10^{-5}$ [30] for reliable carrier estimation. Optimization of PLL design parameters (e.g., loop bandwidth, damping factor) between the competing demands of good BER performance and acquisition time or estimation range is complex, and needs to be evaluated numerically [8]. PLLs are unsuitable in reconfigurable optical systems as their loop parameters cannot be optimized adaptively.

Current interest lies in intradyne coherent detection using a free running LO laser, followed by sampling with high-speed analog-to-digital converter (ADC), and execution of carrier estimation in digital signal processing (DSP) modules [31]. Even when PLLs may fail due to delay constraints, DSP based carrier estimation methods can permit the use of lasers with broader linewidths such as the cost-effective DFB lasers by relaxing the laser linewidth and frequency offset requirements.

1.2 Access Networks

Sustained growth in demand for broadband multimedia services by end users in indoor and outdoor environments has fueled research in the last-mile access technology. Next generation access networks are expected to provide large data bandwidth, multiple broadband applications, high quality of service, mobility support, and ubiquitous coverage [32]. Broadband wireless access network, using a hybrid architecture comprising an untethered wireless access front-end and a high-capacity low-loss optical backhaul to transport radio over fiber (RoF), is regarded as a promising solution [33]. Here, distributed remote base stations (RBSs) serve as wireless gateways catering broadband connectivity to end users and are connected to a central office (CO) via an optical fiber network [34]. This distribution system can provide a wide service coverage area catering to a large number of fixed and mobile users, while providing a quick and cheap installation of RBSs. The RBSs can be implemented simply by using a laser diode, an optical modulator, an optical receiver, electrical amplifiers, and antennas. Since the received radio signal at each RBS is directly imposed onto the laser for transmission without any frequency translation or signal processing [34], RoF provides a transparent and homogeneous infrastructure for multiple services which can be upgraded gracefully. RoF systems allow network operators to concentrate the system intelligence and share equipments at the CO while using RBSs with low complexity.

RoF systems available today generally use IMDD links for reasons of cost and simplicity [35]. Additionally, direct detection links are inherently insensitive to phase noise [32]. In order to improve the reliability of the RoF system, to centralize channel wavelength management, and to reduce the maintenance cost of failure-prone laser diodes at the RBSs, it is highly desirable for service providers to move the light sources to the CO. Furthermore, stringent requirements on frequency stability make placing lasers at RBS expensive. Centralized light source calls for a loopback configuration.

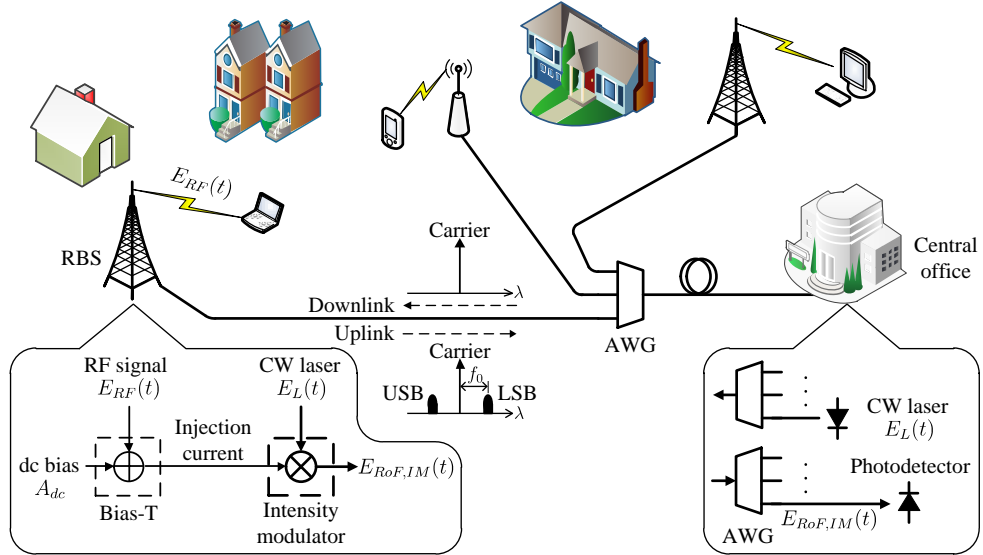


Figure 1.1: Principle of upstream transmission in an IMDD WDM RoF system.
 LSB: lower-frequency sideband, USB: upper-frequency sideband.

The principle of upstream transmission in an IMDD RoF system with multiple subscribers for a loopback access network is illustrated in Fig. 1.1 and can be explained as follows. A wavelength-division multiplexed (WDM) continuous-wave (CW) laser seed light from the CO traverses the transmission fiber, is demultiplexed by arrayed waveguide grating (AWG), and is fed to the intensity modulator at each RBS for upstream modulation. The optical field of each CW laser seed light can be modeled as $E_L(t) = \exp(j2\pi f_L t)$, where f_L is the laser diode frequency. The wireless radio

frequency (RF) signal received at the RBS can be modeled as

$$E_{RF}(t) = A(t) \cos(\phi(t) + 2\pi f_0 t), \quad (1.3)$$

where f_0 is the RF carrier frequency, and $A(t)$ and $\phi(t)$ are the amplitude and phase, respectively, of the transmitted symbol. The RF signal is level shifted with a dc bias of A_{dc} , applied through a bias-T, to avoid negative modulating values. The biased RF signal is modulated onto the envelope of the CW laser using an intensity modulator, generating an optical field of

$$E_{RoF,IM}(t) = [A_{dc} + A(t) \cos(\phi(t) + 2\pi f_0 t)] \exp(j2\pi f_L t) \quad (1.4)$$

comprising an optical carrier and two sidebands (i.e., double-sideband (DSB) modulation). These modulated $E_{RoF,IM}(t)$ signals are then multiplexed in the AWG and sent back to the CO for detection. The transmitted RF signal in each channel is recovered at the CO by a square-law photodetection, followed by a dc block to remove dc components. Since the wavelength of the seed light determines that of the upstream signal, centralized wavelength management of the channels is made possible.

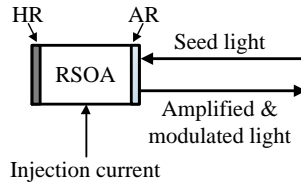


Figure 1.2: Schematic diagram of an RSOA.

The key element in a loopback network is the optical modulator at the RBS, for which a reflective semiconductor optical amplifier (RSOA) has been favorably identified [36]. Fig. 1.2 depicts a schematic diagram of a single-port RSOA. The device comprise an amplifying waveguide with an anti-reflector (AR) at the front end acting as the input/output port and a high reflector (HR) at the rear end [37]. The injected current directly modulates the gain of the RSOA and thus the intensity of the incident

light. In short, light injected into a directly-modulated RSOA is amplified, intensity modulated, and reflected back out through the same port.

RSOAs are desirable for their (i) low cost and compact size, (ii) natural combination of modulation and amplification, (iii) color-free operation (with very wide optical bandwidth of more than 60 nm), and (iv) low noise figure [38]. RSOA being a single-port device, unlike the two-port LiNbO₃ Mach-Zehnder modulators (MZMs) and electroabsorption modulators, minimizes the active fiber alignments required and has a less expensive packaging cost [36]. Inbuilt amplification gain helps overcome any coupling losses, thus relaxing fiber alignment tolerance in RSOAs. Colorless RSOAs allow wavelength-independent operation of the RBS, which enables dynamic wavelength allocation to RBSs, alleviates the inventory problem, and minimizes the deployment costs.

RSOA placed at the RBS and seeded by an optical carrier from the CO have been successfully exploited to yield reliable RBSs [39–42]. However, all previously reported RoF systems using RSOAs only accommodate RF carriers of ≤ 1 GHz, with a maximum encoded data rate of 54 Mb/s over 20-km fiber [39, 40]. This is because the modulation bandwidth of RSOAs is limited by the carrier life-time in the active layer to less than 3.5 GHz [39]. It is, therefore, challenging to accommodate higher RF carriers and data rate with the severely bandwidth-limited RSOA. Furthermore, the chirp of RSOA will hamper the transmission reach of the system [43].

A key issue in DSB optical signals is the power penalty due to chromatic dispersion (CD)-induced phase shift of the two sidebands relative to the optical carrier, which limits the transmission distance and supportable RF frequencies [44, 45]. Another drawback to be considered is the SNR degradation of the received signal in networks using centralized light sources due to crosstalk from Rayleigh backscattered light [46].

1.3 Research Contributions

This thesis contributes three new receiver designs for optical communications. They are namely, two new DSP based carrier estimators in coherent receivers for long-haul transmissions and one new optical signal processing based direct detection receiver in IMDD RoF systems for wireless broadband access networks. The new receiver designs and their improvement over prior art are as follows.

A novel complex-weighted decision-aided maximum-likelihood (CW-DA-ML) carrier estimator for joint phase and frequency estimation is derived in Chapter 3. CW-DA-ML is a decision-aided least-squares based estimator, which achieves fast carrier acquisition, complete frequency estimation range, low SNR operability, requires no phase unwrapping, reliably tracks time-varying frequency, and is format transparent. Additionally, a pilot-assisted (PA) CW-DA-ML is demonstrated with low pilot overhead. Moreover, the most desirable 4-, 8-, and 16-point constellations from the carrier recovery perspective are identified to be QPSK, 8-QAM, and 16-QAM, respectively.

A novel low-complexity adaptive complex-weighted decision-aided (CW-DA) carrier estimator with a two-tap structure is derived in Chapter 4. Unlike classical estimators with fixed-length filters, the effective filter length in adaptive CW-DA estimator is automatically optimized according to SNR, $\Delta\nu T$, nonlinear phase noise, and modulation format. No preset parameters are required. Furthermore, we demonstrate that cycle slip probability is affected by the choice of filter length. Besides inheriting the advantages of CW-DA-ML, adaptive CW-DA estimator is superior in terms of low cycle slip probability, large nonlinear phase noise tolerance, and low complexity.

A novel optical solution, where a passive optical delay interferometer (DI) is incorporated before the photodetector in the direct detection receiver, is presented for ROF receiver design in Chapter 5. DI equalizes the band-limitation of RSOA, counter-chirps the pulse to extend transmission reach, and makes the signal immune to CD-

induced fading, without any additional signal processing at the RBS. Bandwidth equalization by DI enables transmission at RF band which further increases the achievable link distance due to reduced in-band beat-noises generated by Rayleigh backscattering at the receiver, compared to baseband transmission after a downconversion at the RBS.

1.4 Thesis Outline

The remainder of this thesis is organized as follows.

In Chapter 2, we examine the merits of various 4-, 8-, and 16-point constellations in terms of their AWGN resilience, phase rotation tolerance, and transmitter implementation complexity. A comprehensive description of coherent optical transmission comprising the transmitter, channel, and receiver is given. Several popular DSP based carrier estimators in the literature are discussed.

In Chapter 3, we address the carrier estimation problem in coherent receivers for long haul transmission systems. CW-DA-ML estimator for joint phase noise and frequency offset estimation is introduced. A comprehensive performance analysis of CW-DA-ML, with respect to other estimators, for various modulation formats in a channel impaired by AWGN, phase noise, and frequency offset is performed.

In Chapter 4, we emphasize the need for adaptive filter lengths, compared to conventional fixed-length filters, in carrier estimators used for coherent receivers. Adaptive CW-DA carrier estimator with an adaptive effective filter length is introduced. Nonlinear phase noise tolerance, cycle slip probability, and complexity of carrier estimators are analyzed.

In Chapter 5, we consider upstream receiver designs at the CO in IMDD RoF systems to tackle the issues of constrained modulation bandwidth, limited transmission distance, and signal fading, due to RSOA and fiber CD. A new direct detection receiver design is proposed and experimentally demonstrated via an upstream transmission of

a 6-GHz binary phase-shift keying (BPSK) radio signal using a directly modulated RSOA.

Finally, conclusion and several suggestions for future work are presented in Chapter 6. Throughout this thesis, $\mathbb{E}[\cdot]$, $|\cdot|$, $\lfloor a \rfloor$, and $\lceil a \rceil$ are the expectation, modulus operator, largest integer smaller than a , and smallest integer larger than a , respectively. Superscript $*$, T , and H denotes conjugate, transpose, and conjugate transpose, respectively. Vectors and matrices are denoted by lowercase and uppercase bold letters, respectively. All vectors are assumed to be column vectors.

Chapter 2

Coherent Optical Systems

Various signaling schemes are first reviewed, followed by a modeling of the coherent optical transmission system and a review of popular carrier estimators from the literature.

2.1 Modulation Formats

2.1.1 Several 4-, 8-, and 16-Point Constellations

In Fig. 2.1, we consider several prospective 4-, 8-, and 16-ary discrete-point constellations which use both field quadratures. We compare the constellations in terms of:

1. minimum Euclidean distance between adjacent points d_{\min} , characterizing its resilience against AWGN,
2. minimum angular separation between adjacent points with the same radius ϕ_{\min} , characterizing its phase-rotation resilience against phase noise and frequency offset, and
3. simplicity in transmitter implementation.

The d_{\min} is computed with a unity average symbol power constraint. Larger values of d_{\min} and ϕ_{\min} imply greater AWGN and phase-rotation resilience, respectively.

2.1 Modulation Formats

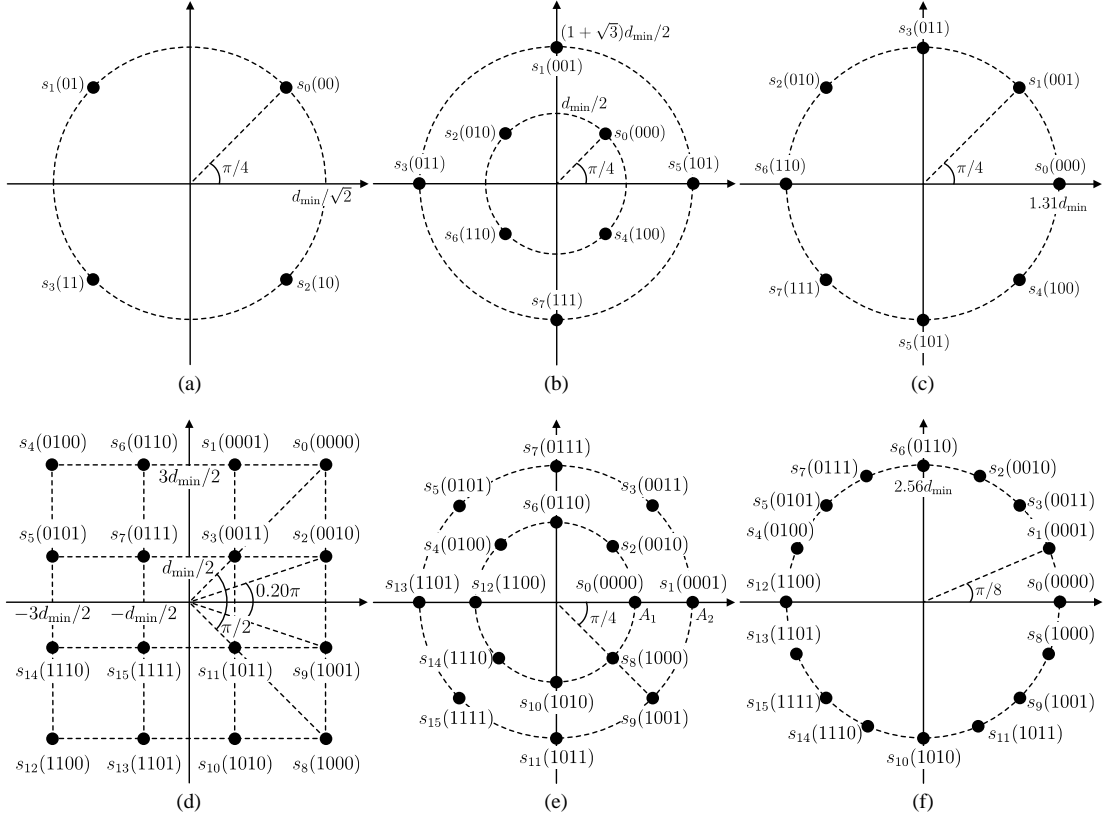


Figure 2.1: Signal constellation and bits-to-symbol mapping for (a) QPSK, (b) 8-QAM, (c) 8-PSK, (d) 16-QAM, (e) 16-Star, and (f) 16-PSK.

In 4-point constellations, we only consider QPSK as it is well established to achieve the best performance for AWGN channel with the largest $d_{\min} = \sqrt{2}$ among all 4-point constellations [7]. The QPSK signal is also easy to generate.

The 8-QAM is defined to be the constellation shown in Fig. 2.1(b). In an AWGN channel, 8-QAM ($d_{\min} = 0.919$) outperforms 8-PSK ($d_{\min} = 0.765$) but is marginally inferior to the optimum 8-point constellation, 8-Hex ($d_{\min} = 0.963$), by 0.35 dB [7, 47]. However, 8-QAM ($\phi_{\min} = \pi/2$) has better phase-rotation tolerance than 8-PSK ($\phi_{\min} = \pi/4$) and 8-Hex ($\phi_{\min} < \pi/3$). Unlike 8-Hex, 8-QAM has a simple transmitter configuration realizable with MZMs and couplers [25], and has a simple differential encoding technique as will be shown later. Hence, we only consider 8-QAM for its desirable properties as outlined above and 8-PSK for further analysis.

The optimum ring ratio, $RR = A_2/A_1$, for 16-Star in an AWGN channel maximizing the distance between adjacent points in the inner ring and that between the two rings is obtained when $RR = 1 + 2 \cos(0.375\pi) \approx 1.77$ [48]. We have used $RR = 1.77$ in this thesis, as the optimum RR with respect to phase rotations only deviate slightly from 1.77 [49]. In an AWGN channel, 16-QAM ($d_{\min} = 0.632$) outperforms 16-Star ($d_{\min} = 0.534$) and 16-PSK ($d_{\min} = 0.390$), but is second by 0.5 dB to the optimum 16-point hexagonal-like constellation [47]. 16-QAM is preferred, compared to the optimum 16-point constellation, due to its simple transmitter implementation where integrated 16-QAM modulators are already available [50] and simple differential encoding technique as will be shown later. However, in terms of phase-rotation tolerance, 16-Star ($\phi_{\min} = \pi/4$) outperforms 16-QAM ($\phi_{\min} = 0.20\pi \& \pi/2$) and 16-PSK ($\phi_{\min} = \pi/8$). Hence, we only consider 16-QAM for its desirable properties as outlined above, 16-Star for its phase rotation tolerance, and 16-PSK for further analysis.

2.1.2 BER Performance

The maximum likelihood detector in an AWGN limited and phase-rotation limited channel has a Euclidean metric with straight-line decision boundaries and a non-Euclidean metric with circular-line boundaries forming polar wedges, respectively [25]. Considering the (i) implementation difficulty of a non-Euclidean metric with circular-line boundaries which requires lookup tables, (ii) advances in laser linewidth which has made DFB lasers with 10 kHz linewidth available [51], and (iii) low SNR operating region of modern systems where AWGN is dominant; we use the Euclidean metric with straight-line decision boundaries in this thesis. The BER over an AWGN channel without differential encoding for MPSK given by [52]

$$\text{BER} = \frac{2}{\log_2 M} \cdot Q \left[\sqrt{2\gamma_b \log_2 M} \sin \left(\frac{\pi}{M} \right) \right], \quad (2.1)$$

2.1 Modulation Formats

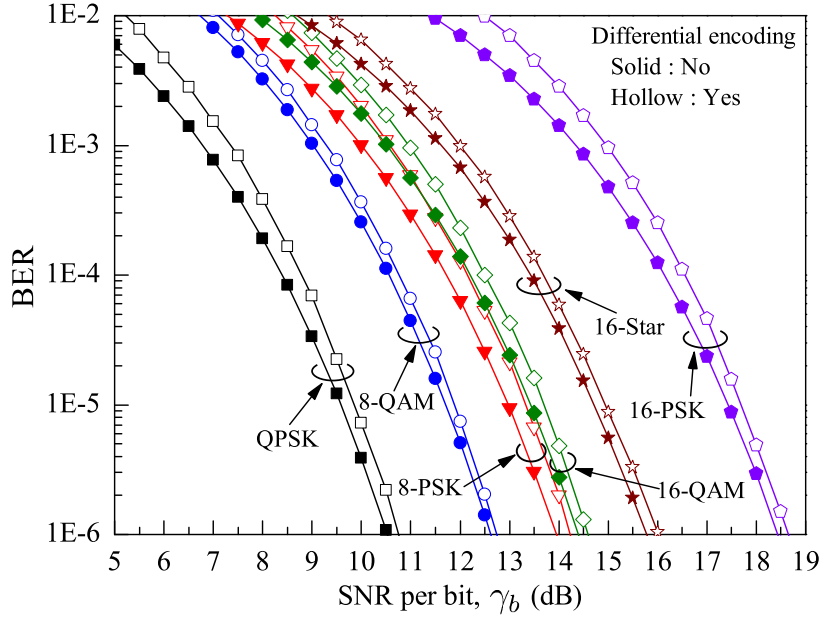


Figure 2.2: BER performance in AWGN channel with and without differential encoding.

8-QAM given by [8]

$$\text{BER} = \frac{22}{16} \cdot Q\left[\sqrt{\frac{6\gamma_b}{3 + \sqrt{3}}}\right], \quad (2.2)$$

16-QAM given by [51]

$$\text{BER} = 1 - \left[1 - \left[\frac{2}{\log_2 M}\right] \left[1 - \frac{1}{\sqrt{M}}\right] \cdot Q\left[\sqrt{\frac{3\gamma_b \log_2 M}{M - 1}}\right]\right]^2, \quad (2.3)$$

and 16-Star obtained through Monte Carlo (MC) simulation, are plotted in Fig. 2.2. Here, M is the number of signal points in the constellation and γ_b is the SNR per bit. Theoretically achievable γ_b values without differential encoding at $\text{BER} = 10^{-3}$ are given in the second column of Table 2.1.

2.1.3 Differential Encoding Technique

We present a generalized sector-based differential encoding technique, built upon the idea in [53], which is applicable to all constellations having ≥ 2 rotationally symmetric

2.1 Modulation Formats

Table 2.1: SNR per bit values at BER = 10^{-3}

Format	AWGN channel without differential encoding (dB)	AWGN channel with differential encoding (dB)	Differential encoding penalty (dB)
QPSK	6.82	7.38 (MC)	0.56
8-QAM	9.04	9.33 (MC)	0.29
8-PSK	10.01	10.60 (MC)	0.59
16-QAM	10.53	10.97 (MC)	0.44
16-Star	11.64 (MC)	11.99 (MC)	0.35
16-PSK	14.37	14.97 (MC)	0.60

MC : Result from Monte Carlo simulation.

positions and no dc signal point (i.e., no signal point at the origin). In a q -sector rotationally symmetric MPSK and M -ary QAM (MQAM) constellation, any signal point can be obtained by rotating a corresponding signal point from the first rotationally symmetric sector. Hence, the k -th information signal point $s(k)$ can be represented by $s(k) = \rho(k)d(k)$. Here $\rho(k) = e^{j2\pi i/q}$, $i \in \{0, \dots, q-1\}$, is the appropriate sector-rotation term and $d(k)$ is the corresponding constellation point of $s(k)$ in the first rotationally symmetric sector. The k th differentially-encoded symbol $m(k)$ is then obtained as $m(k) = \bar{\rho}(k)d(k)$, where $\bar{\rho}(k) = \rho(k)\bar{\rho}(k-1)$. Here, $\bar{\rho}(k)$ represents the current sector in which $m(k)$ lies. Differential decoding of the k th symbol $m(k)$ at the receiver proceeds as

$$\begin{aligned} s(k) &= \frac{m(k)}{\bar{\rho}(k-1)} \\ &= \frac{\bar{\rho}(k)d(k)}{\bar{\rho}(k-1)} \end{aligned} \tag{2.4}$$

The initial sector $\bar{\rho}(-1) = 1$.

Differential encoding increases the BER as any symbol detection error manifests itself twice through differential encoding and is depicted in Fig. 2.2. The differential encoding induced penalty at $\text{BER} = 10^{-3}$ in an AWGN channel is summarized in

column three of Table 2.1. To minimize bit errors due to symbol errors, careful bits-to-symbol mapping is needed. For constellations where $q = 2^{\bar{q}}$ for some integer \bar{q} , we adopt the following bits-to-symbol mapping scheme. All symbols within each sector are assigned the same first \bar{q} bits, in order to minimize bit errors due to adjacent symbol errors caused by AWGN. These first \bar{q} bits are differentially encoded for symbols in adjacent sectors. The last $\log_2(M) - \bar{q}$ bits of each symbol are encoded to be rotationally invariant, thus making them immune to cycle slips. The bits-to-symbol mapping for differentially encoded signals is shown in Fig. 2.1.

2.2 Coherent Optical Transmission System

Consider the dual-polarization optical transmission system with an intradyne receiver shown in Fig. 2.3. The transmission system can be divided into the transmitter, channel, and receiver portions. The receiver comprises of four key subsystems, namely, (i) optical hybrid downconverter which linearly maps the optical field into electrical signals, (ii) ADC which quantizes the analog signal into a set of discrete values, (iii) DSP modules which compensate for transmission impairments, and (iv) the symbol detector which performs coherent symbol detection.

Key DSP modules comprise of (i) clock recovery, (ii) CD compensation, (iii) polarization demultiplexing and polarization-mode dispersion (PMD) compensation, and (iv) carrier phase and frequency estimation. In principle, all linear impairments can be compensated ideally using digital filters [52].

The coherent transmission system adopted in this thesis is described in detail next.

2.2.1 Transmitter

The transmitter laser output is split into two orthogonal polarizations, \vec{x} and \vec{y} , by a polarization beam splitter (PBS). The two polarizations are modulated by separate data

2.2 Coherent Optical Transmission System

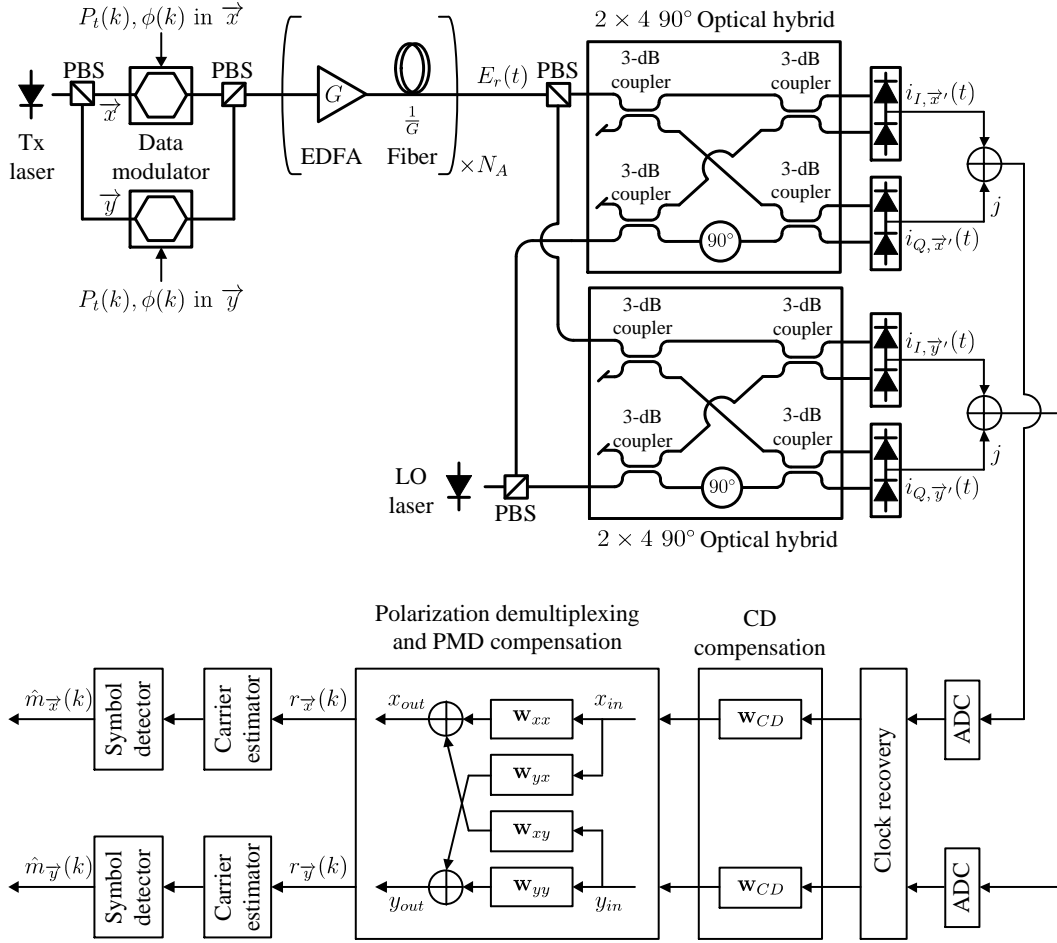


Figure 2.3: Polarization multiplexed coherent optical system. Tx: transmitter.

modulators and recombined in a polarization beam combiner. The input optical field into the fiber in each polarization can be written as

$$E_t(t) = \sum_k \sqrt{P_t(k)} e^{j\phi(k)} h(t - kT) e^{j(\theta_s(t) + \omega_s t)} \quad (2.5)$$

where T is the symbol period. $P_t(k)$ and $\phi(k)$ represents the power and phase, respectively, of the k th transmitted symbol. Here, $h(t)$ is the pulse shape, assumed to be a non-return-to-zero (NRZ) pulse with the normalization $\int |h(t)|^2 = T$. In Eq. (2.5), $\theta_s(t)$ and ω_s are the phase noise and angular frequency of the transmitter laser, respectively. The phase noise arises due to nonzero linewidth of the Lorentzian line-shaped laser.

2.2.2 Channel

- **Fiber Loss**

The channel consists of N_A fiber spans of equal length L_f . Material absorption, Rayleigh scattering, and waveguide imperfections contribute to the fiber attenuation coefficient α which reduces the signal power. If P_{in} is the input power, then the output power P_{out} at the end of a fiber of length L_f is

$$P_{out} = P_{in} e^{-\alpha L_f}. \quad (2.6)$$

It is customary to express α in units of dB/km using the relation [54]

$$\begin{aligned} \alpha(\text{dB/km}) &= -\frac{10}{L_f} \log_{10} \left(\frac{P_{out}}{P_{in}} \right) \\ &= -\frac{10}{L_f} \log_{10} (e^{-\alpha L_f}) \\ &\approx 4.343\alpha \end{aligned} \quad (2.7)$$

where Eq. (2.6) was used in the second step above and $\alpha(\text{dB/km})$ is referred to as the fiber-loss parameter. Modern day fiber loss is reduced to ~ 0.2 dB/km at an optical wavelength of 1550 nm [55].

- **Optical Amplifier**

Optical amplification is employed to avoid frequent optoelectronic regeneration along the link due to fiber loss. Fiber loss in each span is assumed to be compensated exactly by an inline erbium-doped fiber amplifier (EDFA) of gain $G = e^{\alpha L_f}$. The output and input powers of an amplifier are related by $P_{out} = G P_{in}$. Optical amplifiers produce spontaneous emission which degrades the SNR of the amplified signal. At the output of the i th EDFA, noise $n_{ASE,i}(t) \cdot e^{j\omega_s t}$ is added to the signal. Here, $n_{ASE,i}(t)$ is the low-pass representation of the amplified spontaneous emission (ASE) noise. It is white, zero-mean, and circularly symmetric complex Gaussian, with spectral density

per state of polarization given as [7]

$$S_{sp} = (G - 1) \frac{\bar{h}c}{\lambda} n_{sp}, \quad (2.8)$$

where n_{sp} is the spontaneous-emission factor, \bar{h} is the Planck's constant, c is the speed of light in vacuum, and λ is the optical carrier wavelength. The quantity $\bar{h}c/\lambda$ is the photon energy. The n_{sp} can range from 1 in an ideal amplifier to 3.15 in practical amplifiers [54]. Variance of $n_{ASE,i}$ per polarization defined over a filter bandwidth B_o matched to the signal is $\sigma_{ASE}^2 = S_{sp}B_o$.

2.2.3 Receiver

- **Optical Hybrid Downconverter**

The front end of the receiver consists of a polarization- and phase-diversity optoelectronic downconverter. The received optical field $E_r(t)$ is separated into two orthogonal polarizations and are separately mixed with a polarization-split LO laser, using two single-polarization 2×4 90° optical hybrids in parallel. Polarization-division multiplexed (PDM) signals can be demultiplexed by the ensuing DSP modules without the need for optical dynamic polarization control at the receiver front end [20]. The LO optical field per polarization state can be described as

$$E_{LO}(t) = \sqrt{P_{LO}} e^{j(\theta_{LO}(t) + \omega_{LO}t)} \quad (2.9)$$

where P_{LO} , $\theta_{LO}(t)$, and ω_{LO} are the power, phase noise, and angular frequency of the LO laser. The LO laser is free running, in contrast to a homodyne downconverter where the LO need to be phase- and frequency-locked to the incoming optical signal. As a consequence, the received optical field is downconverted to an intermediate angular frequency of $\Delta\omega = \omega_s - \omega_{LO}$. The transfer matrix of the each optical hybrid is given

by [56]

$$\mathbf{H}_{OH} = \frac{1}{2} \begin{bmatrix} 1 & 1 \\ 1 & -1 \\ 1 & j \\ 1 & -j \end{bmatrix}. \quad (2.10)$$

Note that the 3-dB fiber couplers of the optical hybrid in Fig. 2.3 functions the same as a 50/50 beam splitter. In each polarization, the outputs of $\mathbf{H}_{OH} \cdot [E_r(t), E_{LO}(t)]^T$ are square-law detected by two pairs of balanced photodetectors and their difference signal constitute the in-phase (I) and quadrature (Q) photocurrents as

$$\begin{aligned} i_I(t) &= \frac{R}{4}|E_r(t) + E_{LO}(t)|^2 - \frac{R}{4}|E_r(t) - E_{LO}(t)|^2 + i_{sh,I}(t) + i_{th,I}(t) \\ &= R\mathbf{Re}[E_r(t)E_{LO}^*(t)] + i_{sh,I}(t) + i_{th,I}(t) \end{aligned} \quad (2.11)$$

and

$$\begin{aligned} i_Q(t) &= \frac{R}{4}|E_r(t) + jE_{LO}(t)|^2 - \frac{R}{4}|E_r(t) - jE_{LO}(t)|^2 + i_{sh,Q}(t) + i_{th,Q}(t) \\ &= R\mathbf{Im}[E_r(t)E_{LO}^*(t)] + i_{sh,Q}(t) + i_{th,Q}(t), \end{aligned} \quad (2.12)$$

respectively. Here, R is the photodetector responsivity. Noises $i_{sh,I}$ and $i_{sh,Q}$ are shot noises caused by random fluctuation in number of electron-hole pairs generated within the photodetector. Assuming $P_{LO} \gg P_t$, the shot noise $i_{sh} = i_{sh,I} + i_{sh,Q}$ have a two-sided power spectral density of $S_{sh} = \varrho RP_{LO}$, where ϱ is the electron charge. The thermal noise i_{th} is caused by random thermal motion of electrons at the receiver. Typically, long-haul amplified transmission systems are ASE noise limited since ASE noise is generally much larger than shot noise and thermal noise [8, 57]. Shot noise and thermal noise are thus neglected in all our studies.

Desirable properties of photodetectors include high sensitivity, high bandwidth, low noise, and low cost. Commonly used photodetectors for lightwave systems with

wavelengths in the range of $1000 - 1700$ nm include InGaAs based *p-i-n* (PIN) photodiodes and avalanche photodiodes (APDs). Internal current gain of APDs can provide about 10 times higher responsivity R , but requires much larger bias voltage values, than PIN photodiodes [54]. Additionally, there is an inherent trade-off between the internal current gain and the bandwidth of APDs. Thermal noise remains the same for both PIN photodiodes and APDs. However, increased shot noise in APDs due to noisy avalanche-gain process can reduce the SNR by an excess noise factor compared to PIN photodiodes in the shot-noise limit [54]. APDs are generally more expensive than PIN photodiodes [58].

In an intradyne receiver, optical frequency bands around $\omega_{LO} + \Delta\omega$ and $\omega_{LO} - \Delta\omega$ will map to the same intermediate angular frequency. To avoid crosstalk in a dense WDM system and to avoid excess ASE noise from unwanted image bands, an optical filter of bandwidth B_o matched to a single channel's signal bandwidth is required before the downconverter.

- **Analog-to-Digital Converter**

The analog output of the photodetectors are digitized by ADCs at a rate of T_0/T , where T_0 is a rational oversampling rate. The optical signal and noise statistics are fully preserved in the sampled signal, when sampling the photocurrents at or above the Nyquist rate. For asynchronous sampling, an oversampling of $T_0 \geq 2$ is preferred as it enables clock recovery [59].

- **Clock Recovery**

In practice, the receiver's clock frequency may differ from the symbol rate, causing $1/T_{ADC} \neq 1/T$ where $1/T_{ADC}$ is the clock frequency of the receiver [60]. Hence, the originally digitized signal $\{x(l)\}$ at time $t = lT_{ADC}/T_0$ is resampled through interpolation to produce the samples $\{y(k)\}$ at time $t = t_0 + kT/T_0$ [59]. Here, t_0 is the timing delay and $k, l = 0, 1, 2, \dots$

Once the clock frequency is recovered, a timing-delay recovery algorithm, e.g., [61], [62], or [63], is used to produce a timing-delay estimate \hat{t}_0 . Using \hat{t}_0 , symbol synchronization can be achieved such that one sample coincides with the decision instant per symbol. This synchronization can be performed either by interpolating the samples $\{y(t_0 + kT/T_0)\}$ to obtain $\{y(t_0 - \hat{t}_0 + kT/T_0)\}$ or by directly changing the interpolation instants in the clock-frequency recovery stage above via feedback of \hat{t}_0 .

- **Dispersion Compensation and Polarization Demultiplexing**

Dispersion refers to the phenomenon where different components of an optical pulse travel at different velocities in the fiber and arrive at different times at the receiver. This would lead to a pulse broadening which causes intersymbol interference (ISI).

In CD, different spectral components of an optical pulse travel independently at different group velocities and do not arrive simultaneously at the fiber output. CD in fibers arise due to a combination of material and waveguide dispersion, where the contribution of the latter is generally smaller than the former except near the zero-dispersion wavelength [64]. Material dispersion occurs due to the wavelength-dependence of the fiber's refractive index, whereas waveguide dispersion is induced by the waveguide's structure. CD acts like an all-pass filter with a flat amplitude response and its transfer function, acting on the phase of the signal, is given by [54]

$$H_{CD}(f) = \exp(-j2\beta_2 L_f \pi^2 f^2) \quad (2.13)$$

where f is the frequency and β_2 is the group velocity dispersion (GVD) parameter. The GVD is related to the dispersion parameter D_{CD} , expressed in units of ps/(nm·km), through

$$D_{CD} = -\frac{2\pi c}{\lambda^2} \beta_2. \quad (2.14)$$

CD is a linear static effect and can be compensated optically by employing in-line

dispersion-compensating fiber (DCF) with GVD $\beta_{2,DCF}$ and fiber length $L_{f,DCF}$ such that $\beta_{2,DCF}L_{f,DCF} = \beta_2 L_f$. Nevertheless, inexact matching of β_2 and L_f would leave residual CD which necessitates electrical CD compensation at the receiver.

Another source of pulse broadening is PMD. A standard single-mode fiber (SSMF) can support two orthogonal polarization modes. Deviations from perfect cylindrical symmetry in the fiber leads to randomly changing birefringence along the fiber. Such fiber possesses a “fast axis” and a “slow axis” in orthogonal polarizations, due to a smaller and a larger associated mode index, respectively [65]. These polarization states are known as the principal states of polarization (PSP). A pulse input to a fiber, which is not polarized along any of the PSP, splits between the two PSP. Hence, different polarization components of a pulse in a SSMF travels at different group velocities and arrive with a timing offset at the receiver, called differential group delay (DGD) τ . The frequency response of the fiber with first-order PMD has the form

$$\mathbf{H}_{DGD}(f) = \begin{bmatrix} \cos \theta' & -\sin \theta' \\ \sin \theta' & \cos \theta' \end{bmatrix} \begin{bmatrix} e^{j2\pi f\tau} & 0 \\ 0 & e^{-j2\pi f\tau} \end{bmatrix} \begin{bmatrix} \cos \theta' & \sin \theta' \\ -\sin \theta' & \cos \theta' \end{bmatrix} \quad (2.15)$$

where θ' is the angle between the reference polarizations and the PSP of the fiber [66]. PMD can fluctuate on the order of a millisecond [67]; it needs continuous tracking and compensation at the receiver. PMD becomes a limiting factor for long-haul systems operating at high bit rates [54] and can cause outage if uncompensated [68]. Besides PMD-induced pulse broadening, PMD also causes crosstalk between polarizations in a PDM system which necessitates polarization demultiplexing [69].

Although electronic equalization for CD, PMD, and polarization crosstalk could be realized in a single structure, it is beneficial to partition the equalizer into static and dynamic portions [70]. Hence the equalization process consists of a linear filter to compensate for the relatively time-invariant CD, followed by a bank of four adaptive finite impulse response (FIR) filters arranged in a butterfly structure to compensate for

the time-varying PMD and polarization crosstalk [71]. The butterfly-like filter structure performs the inverse Jones matrix of the channel on the input block of samples \mathbf{x}_{in} and \mathbf{y}_{in} such that the outputs are given by

$$x_{out} = \mathbf{w}_{xx}^T \mathbf{x}_{in} + \mathbf{w}_{xy}^T \mathbf{y}_{in} \quad (2.16)$$

$$y_{out} = \mathbf{w}_{yx}^T \mathbf{x}_{in} + \mathbf{w}_{yy}^T \mathbf{y}_{in} \quad (2.17)$$

where \mathbf{w}_{xx}^T , \mathbf{w}_{xy}^T , \mathbf{w}_{yx}^T , and \mathbf{w}_{yy}^T are the FIR filter-weight vectors. Several prevalent algorithms used to adapt the filter weights of the CD, PMD, and polarization crosstalk equalizers are minimum-mean-square error [72], constant modulus algorithm [73], recursive least squares, least-mean squares, and radius directed equalization [66]. Compared to FIR filters, infinite impulse response filters require less taps but tend to be unstable especially at larger values of residual CD [74].

If the system parameters are known, the filter weights of a time-domain transversal equalizer for CD can be obtained by computing the inverse Fourier transform of the inverse CD transfer function as [75]

$$w_{CD,l} = \frac{T}{T_0} \int_{-\infty}^{\infty} H_{CD}^{-1}(f) \exp\left(j2\pi f \frac{lT}{T_0}\right) df, \quad (2.18)$$

where $l = 1, 2, \dots, L_{CD}$. A filter length of $L_{CD} = 2\pi T_0 |\beta_2| L_f / T^2$ is sufficient to fully compensate the CD present [8]. Alternatively, CD can be compensated in the frequency domain by multiplying the Fourier transform of the received signal with $H_{CD}^{-1}(f)$, and converting the output back to time domain for subsequent DSP. Taking the inverse of $H_{CD}(f)$ amounts to inverting the sign of the GVD parameter β_2 in Eq. (2.13).

Fractionally spaced equalizers (FSEs), compared to symbol spaced equalizers, can adaptively synthesize a single structure with the best combination of matched filter and equalizer [76, 77]. Unlike symbol spaced equalizers which are susceptible to sampling time errors, FSE is insensitive to sample timing [78]. FSE with an adequate filter length completely compensates unlimited amount of CD and first-order PMD,

whereas the compensable amount of dispersion only approaches an asymptote in symbol spaced equalizers [72]. An oversampling rate of $T_0 = 2$ in conjunction with FSE is preferred as it is invariably used for compensation of CD and PMD, and polarization demultiplexing in experiments [28, 75]. Insensitivity to sample timing allows FSE to be deployed ahead of the clock recovery module for dispersion mitigation in scenarios where reliable clock recovery is hampered by large dispersion values.

- **Input Samples to Carrier Estimator**

In Chapter 3 and 4, we assume ideal signal conditioning by the ADC and the preceding DSP modules, namely, clock recovery, CD compensation, and polarization demultiplexing and PMD compensation. This is equivalent to having a received optical field per state of polarization of

$$E_r(t) = \sum_k \sqrt{P_r(k)} e^{j\phi(k)} h(t - kT) e^{j(\theta_s(t) + \omega_s t)} + n_{ASE}(t) e^{j\omega_s t}. \quad (2.19)$$

where $n_{ASE} = \sum_{i=1}^{N_A} n_{ASE,i}$ is the accumulated ASE white noise with mean zero and variance $N_A \sigma_{ASE}^2$. Assuming perfect compensation by EDFA for fiber loss in each span, we have received symbol power $P_r(k) = P_t(k)$. Substituting Eq. (2.19) into Eq. (2.11) and Eq. (2.12), and sampling, we obtain the combined in-phase and quadrature photocurrents as

$$\begin{aligned} i_I(k) + j i_Q(k) &= R E_r(k) E_{LO}^*(k) \\ &= R \sqrt{P_r(k) P_{LO}} e^{j\phi(k)} e^{j(\theta_L(k) + \Delta\omega k)} \\ &\quad + R \sqrt{P_{LO}} n_{ASE}(k) e^{j(-\theta_{LO}(k) + \Delta\omega k)} \end{aligned} \quad (2.20)$$

where $\theta_L(k) = \theta_s(k) - \theta_{LO}(k)$ is the combined linear laser phase noise. We have $\Delta\omega = 2\pi\Delta f$ where Δf is the frequency offset between the transmitter and LO lasers. The first term on the right-hand side of Eq. (2.20) is the desired signal-LO beat term, and the second term is the LO-ASE beat noise. Using ideal balanced photodetection

in the receiver fully suppresses the signal-ASE and ASE-ASE beat terms.

We let the input sample $r(k)$ to the carrier estimator over the k th symbol interval $[kT, (k+1)T]$, which is clock synchronized with one complex sample per symbol, to be

$$\begin{aligned} r(k) &= i_I(k) + j i_Q(k) \\ &= m(k)e^{j(\theta(k)+\Delta\omega k)} + n(k) \end{aligned} \quad (2.21)$$

where $m(k) = R\sqrt{P_r(k)P_{LO}}e^{j\phi(k)}$ is the k th symbol and $\theta(k)$ represents the total phase noise impairment in the received sample. We have $\theta(k) = \theta_L(k)$ in the linear regime. Nonlinear phase noise impairment will be introduced in Section 4.4. The linear laser phase noise $\theta_L(k)$ is modeled as a Wiener process

$$\theta_L(k) = \sum_{l=0}^k \nu(l), \quad (2.22)$$

where $\nu(l)$'s are independent and identically distributed Gaussian random variables with mean zero and variance $\sigma_p^2 = 2\pi\Delta\nu T$ [79]. Here, $\Delta\nu$ is the sum of the 3-dB linewidth of the transmitter and LO lasers. The modulo- 2π reduced angular frequency offset $\Delta\omega$ is assumed to have a probability density function (PDF) given by $p(\Delta\omega) = 1/2\pi$ for $\Delta\omega \in [-\pi, +\pi]$, where $\Delta\omega$ is a random variable. The $\Delta\omega$ is assumed to be time invariant unless otherwise stated. In Eq. (2.21), the LO-ASE beat noise $R\sqrt{P_{LO}}n_{ASE}(k)e^{j(-\theta_{LO}(k)+\Delta\omega k)}$ is modeled by an equivalent zero-mean additive white Gaussian noise source $n(k)$ with variance $\sigma_n^2 = R^2 P_{LO} N_A \sigma_{ASE}^2$. The SNR per bit in a single polarization is defined as $\gamma_b = \mathbb{E}[|m(k)|^2]/(\sigma_n^2 \log_2 M)$.

All γ_b penalties are referenced to the γ_b of a perfectly coherent ASE-noise-limited receiver at $\text{BER} = 10^{-3}$ (without differential encoding) which is summarized in the second column of Table 2.1. Differential encoding of data is assumed in Chapter 3 and 4 to arrest cycle slips in the carrier estimators, unless otherwise stated.

- **Carrier Estimator**

In Chapter 3 and 4, we consider the detection of an uncoded data symbol sequence $\{m(k)\}$ transmitted over the channel illustrated in Fig. 2.3 with unknown carrier phase and frequency offset, as modeled by Eq. (2.21). Since the data is uncoded, the symbols of $\{m(k)\}$ are independent and each assumes one of the equally likely points in the signal set $\{s_i\}_0^{M-1}$. Elements of the phase noise sequence $\{\theta(k)\}$ are temporally correlated since $\{\theta_L(k)\}$ has an autocorrelation of

$$\mathbb{E}[\theta_L(k)\theta_L(l)] = \sigma_p^2 \cdot \min[k, l]. \quad (2.23)$$

The assumption of an AWGN channel with no ISI makes the elements of the noise sequence $\{n(k)\}$ independent. The elements of the received signal sequence $\{r(k)\}$ are rendered independent when conditioned on given values of $\{m(k)\}$, $\{\theta(k)\}$, and Δf . Hence, each symbol $m(k)$ in the sequence $\{r(k)\}$ will be detected individually, i.e., symbol-by-symbol with minimum symbol error probability. We assume mutual statistical independence among $\{m(k)\}$, $\{\theta(k)\}$, and Δf , which leads to the separation of the carrier estimation problem from the symbol detection problem [80]. Therefore, at high SNR, the optimum symbol-by-symbol receiver structure consists of a carrier estimator followed by a coherent symbol detector, as illustrated in Fig. 2.3 [80].

Carrier estimator is employed to produce an estimate $\hat{\zeta}(k)$ of the true carrier phasor $\zeta(k) = e^{j(\theta(k)+\Delta\omega k)}$ in the received sample $r(k)$. Carrier estimation and symbol detection is performed independently for each polarization channel as shown in Fig. 2.3. All equations and quantities expressed hereafter are thus meant for one polarization channel.

- **Symbol Detector**

Treating the carrier-estimate $\hat{\zeta}(k)$ generated by the carrier estimator as the true phasor $e^{j(\theta(k)+\Delta\omega k)}$, the sample $r(k)$ is multiplied by $\hat{\zeta}^*(k)$ to compensate for the carrier phase and angular frequency offset. The derotated sample $r(k)\hat{\zeta}^*(k)$ is plugged into

the maximum-likelihood minimum-Euclidean distance detector for an AWGN channel given by [52]

$$\hat{m}(k) = \arg \min_{0 \leq i \leq M-1} |r(k)\hat{\zeta}^*(k) - s_i| \quad (2.24)$$

to perform a (partially) coherent symbol detection. Here, $\arg \min_i a(i)$ selects the i that minimizes $a(i)$. Assuming unconstrained symbol energy, the symbol detector is simplified by expanding the equation, dropping terms that do not depend on the trial symbol s_i , and rearranging them to yield

$$\begin{aligned} \hat{m}(k) &= \arg \min_{0 \leq i \leq M-1} \left[|r(k)\hat{\zeta}^*(k)|^2 + |s_i|^2 - \operatorname{Re} [2r(k)\hat{\zeta}^*(k)s_i^*] \right] \\ &= \arg \min_{0 \leq i \leq M-1} \left[|s_i|^2 - \operatorname{Re} [2r(k)\hat{\zeta}^*(k)s_i^*] \right] \\ &= \arg \max_{0 \leq i \leq M-1} \operatorname{Re} \left[r(k)\hat{\zeta}^*(k)s_i^* - \frac{1}{2}|s_i|^2 \right]. \end{aligned} \quad (2.25)$$

The (partially) coherent symbol detector declares the signal s_i from the signal set $\{s_i\}_{i=0}^{M-1}$ which maximizes $\operatorname{Re}[r(k)\hat{\zeta}^*(k)s_i^* - (1/2)|s_i|^2]$ as the symbol decision $\hat{m}(k)$.

2.3 Frequency and Phase Estimators

Here, clock-aided discrete-time observation based carrier estimation algorithms are considered, i.e., the receiver has perfect knowledge of symbol timing and uses digitized signal. Carrier estimators available in the literature consists of a two stage sequential process of frequency offset compensation followed by phase noise compensation, as phase estimators are only unbiased in the absence of frequency offset [59].

We review several popular phase and frequency estimators next. The statistical models of the phase noise $\theta(k)$, and angular frequency offset $\Delta\omega$, are not known to the receiver. All phase quantities $\theta(k)$ are treated modulo- 2π and frequency offset quantities Δf are treated modulo- $1/T$ to account for their circular nature.

2.3.1 Fast Fourier Transform based Frequency Estimator

A family of non-data aided (NDA) frequency estimators achieving the modified Cramer Rao bound at high SNR [81] was proposed in [82] and later applied to optical communications in [83]. The frequency estimate $\hat{\Delta f}$ is given by

$$\hat{\Delta f} = \frac{1}{q} \arg \max_{|\Delta \bar{f}| < 1/2T} \left| \sum_{k=0}^{N-1} r^q(k) e^{-j2\pi \Delta \bar{f} T k} \right| \quad (2.26)$$

where N is the received sample size over which the frequency acquisition is performed and is illustrated in Fig. 2.4.

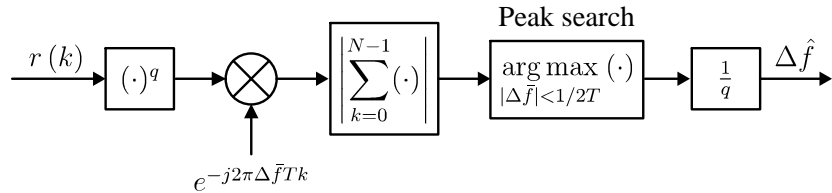


Figure 2.4: Fast Fourier transform based frequency estimator.

Cyclostationary statistics is exploited for modulation removal by raising the received signal to the q th power, where $q = M$ in MPSK and $q = 4$ in 16-QAM. Equation (2.26) leads to a computationally intensive peak search in the periodogram of $r^q(k)$. The peak search can be implemented by fast Fourier transform (FFT) technique [84].

The frequency estimate resolution is limited by N to $1/qNT$. A larger N improves the frequency estimate accuracy, but increases the acquisition time and FFT complexity. These conflicting requirements call for a trade-off but no automatic optimization method is known. FFT based frequency estimator (FFTFE) suffers from an undesirable SNR threshold effect, where a noise peak exceeding the true frequency peak causes a large frequency estimation error (known as an outlier) below some critical SNR value [85]. The likelihood of outliers increases with decreasing SNR, having a disabling effect on FFTFE at low SNR.

2.3.2 Differential Frequency Estimator

An NDA phase differential frequency estimator (DiffFE) was proposed in [86] and later applied to optical communications in [87] for MPSK modulations. The sample-autocorrelation based frequency estimator is given by

$$\hat{\Delta f} = \frac{1}{2\pi MT} \arg \left(\sum_{k=0}^{N-1} (r(k)r^*(k-1))^M \right) \quad (2.27)$$

and is illustrated in Fig. 2.5.

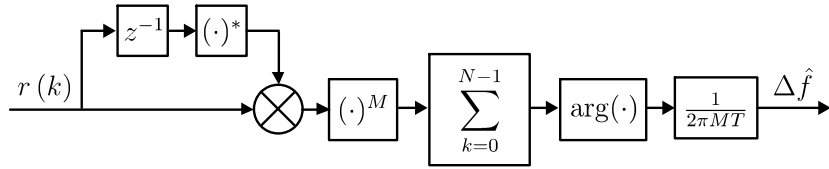


Figure 2.5: Differential frequency estimator.

DiffFE performs complex conjugate multiplication of adjacent received samples. The phase differenced samples are raised to M th power for modulation removal, summed over N samples to smooth out the noise, and the argument of the sum is divided by $2\pi MT$ to obtain the frequency estimate. Accuracy of $\hat{\Delta f}$ is dependent on the N used, but choice of optimum N is rather subjective and no adaptive optimization techniques have been reported.

DiffFE was extended to 16-QAM signals by only phase differencing consecutive Class I symbols in [88]. Class I symbols comprise signal points with modulation phases of $\pi/4 + i\pi/2$ where $i = 0, 1, 2, 3$, i.e., signal points $s_0, s_3, s_4, s_7, s_8, s_{11}, s_{12}$, and s_{15} in Fig. 2.1(d). The use of only a subset of symbols for frequency estimation will cause performance degradation in channels with time-varying frequency offset.

2.3.3 Block M th Power Phase Estimator

A prevalent NDA phase estimator is the block M th power phase estimator (MPE), which was presented for MPSK in [89]. M th power synchronizer was shown to be

an approximate maximum likelihood feedforward phase estimator at low SNR [90, Section 5.7.4]. The phase estimate $\hat{\theta}$ is given by

$$\hat{\theta} = \frac{1}{M} \arg \left(\sum_{l=0}^{L-1} r^M((i-1)L+l) \right), \quad i = 1, 2, \dots \quad (2.28)$$

and is illustrated in Fig. 2.6.

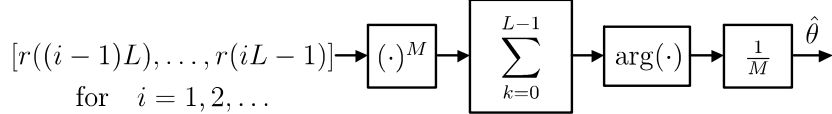


Figure 2.6: Block M th power phase estimator.

Modulation is removed by raising samples to the M th power. Received samples are processed in blocks of length L to yield a single phase estimate $\hat{\theta}$ which is used to phase-correct all L samples in the respective block. The estimate is biased for symbols away from the center of the block [91] because the phase noise θ may not remain constant across the block. MPE was adapted for 16-QAM through a QPSK partitioning technique in [92].

Since the $\arg(\cdot)$ function returns values in the range of $\pm\pi$, $\hat{\theta}$ is restricted within $\pm\pi/q$, where q is the number of rotationally symmetric sectors in the constellation. This leads to q -fold ambiguity in $\hat{\theta}$, which can be resolved by using differential encoding. Due to the modulo- $2\pi/q$ operation in MPE, $\hat{\theta}$ exhibits a jump, compared to that of the previous block, every time the phase noise θ crosses an odd multiple of π/q . Hence, $\hat{\theta}$ needs to be phase unwrapped. Phase unwrapping ensures the difference between consecutive phase estimates is within $\pm\pi/q$ by adding or subtracting some integer multiple of $2\pi/q$, which can be summarized as follows [89]:

$$\hat{\theta}(k) = \begin{cases} \hat{\theta}(k) + \frac{2\pi}{q}, & \text{if } \hat{\theta}(k) - \hat{\theta}(k-1) > \frac{\pi}{q} \\ \hat{\theta}(k) - \frac{2\pi}{q}, & \text{if } \hat{\theta}(k) - \hat{\theta}(k-1) < -\frac{\pi}{q} \\ \hat{\theta}(k), & \text{else} \end{cases} \quad (2.29)$$

2.3.4 Blind Phase Search

An NDA joint estimation of data symbol and phase was introduced as the blind phase search (BPS) method in [51], which was previously developed by [93, 94]. The general idea of BPS, illustrated in Fig. 2.7, is to try multiple test phase angles and to pick the angle which yields the shortest Euclidean distance to the nearest signal point in the constellation.

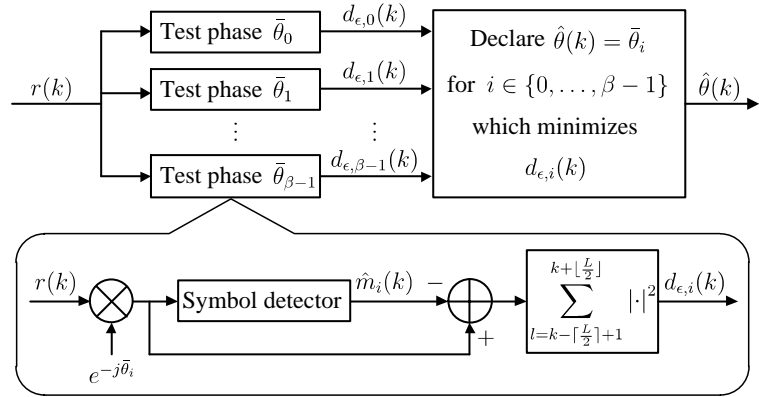


Figure 2.7: Blind phase search estimator.

The received sample $r(k)$ is first individually derotated by β test phase angles $\bar{\theta}_i$,

where

$$\bar{\theta}_i = \frac{i}{\beta} \cdot \frac{2\pi}{q}, \quad i \in \{0, \dots, \beta-1\}. \quad (2.30)$$

For each $\bar{\theta}_i$, the squared magnitude error between the derotated sample and corresponding symbol decision is averaged over L samples for noise smoothing as

$$d_{\epsilon,i}(k) = \sum_{l=k-\lceil \frac{L}{2} \rceil + 1}^{k+\lfloor \frac{L}{2} \rfloor} \left| r(k)e^{-j\bar{\theta}_i} - \hat{m}_i(k) \right|^2. \quad (2.31)$$

Here, $\hat{m}_i(k)$ is the symbol decision on $r(k)e^{-j\bar{\theta}_i}$. The $\bar{\theta}_i$ whose index yields the smallest average squared magnitude error $d_{\epsilon,i}(k)$ is declared as the phase estimate $\hat{\theta}(k)$ at time k following

$$\hat{\theta}(k) = \arg \min_{0 \leq i \leq \beta-1} [d_{\epsilon,i}(k)]. \quad (2.32)$$

Due to a q -fold ambiguity inherent in BPS, phase unwrapping of $\hat{\theta}(k)$ according to Eq. (2.29) is required. The accuracy of $\hat{\theta}(k)$ is inversely proportional to the complexity of BPS and is determined by β , but no automatic optimization for β is available.

2.3.5 Decision-Aided Maximum-Likelihood Phase Estimator

A decision-aided phase estimator of interest is the decision-aided maximum-likelihood (DA-ML) phase estimator derived in [95, 96] and illustrated in Fig. 2.8. The interest in DA-ML lies in its maximum likelihood derivation, and its near optimum maximum-likelihood phase estimation at high and medium SNR [97].

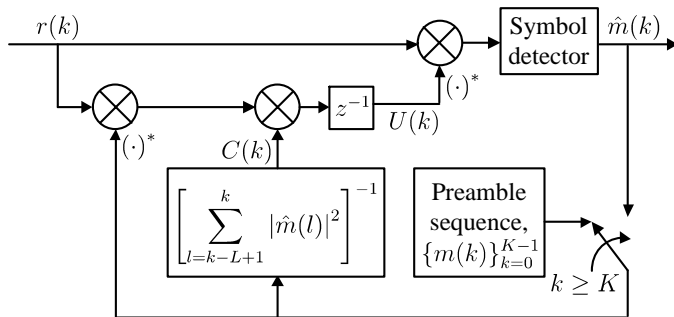


Figure 2.8: DA-ML phase estimator.

The phase noise process $\{\theta(k)\}$ is assumed to vary slower than the symbol rate such that we can approximate $\theta(k)$ to be piecewise constant over intervals longer than LT , where L is an integer representing the filter length. In DA-ML, the maximum likelihood phase estimate $\hat{\theta}(k+1)$ at time $k+1$ is given by the argument of a complex reference phasor $U(k+1)$. The reference phasor is computed using the immediate past L received samples as

$$U(k+1) = C(k) \sum_{l=1}^L r(k-l+1) \hat{m}^*(k-l+1) \quad (2.33)$$

where $\hat{m}(k)$ is the symbol decision on $r(k)$ made by the symbol detector according to

Eq. (2.25) and $C(k)$

$$C(k) = \left(\sum_{l=1}^L |\hat{m}(k-l+1)|^2 \right)^{-1} \quad (2.34)$$

is to normalize the magnitude of $U(k+1)$ in the event of a non-constant modulus signal constellation. Derivation of DA-ML is provided in Appendix A.

An initial preamble of K known symbols is required to startup the receiver, subsequently symbol decisions will be fed back to form the reference phasor. DA-ML avoids additive noise contribution from higher powers (≥ 2) which are present in MPE [95].

Chapter 3

Complex-Weighted Decision-Aided Maximum-Likelihood Phase and Frequency Estimation

Extending upon DA-ML [95, 96], we propose here a novel format-independent CW-DA-ML estimator which jointly estimates the unknown phase noise and frequency offset. The performance of CW-DA-ML is placed in perspective with respect to two fundamental carrier estimators in the literature, namely, (i) FFTFE-MPE (refers to FFTFE [82] followed by MPE [89, 92]) and (ii) DiffFE-MPE (refers to DiffFE [87, 88] followed by MPE [89, 92]). PA CW-DA-ML is introduced and performance gain over its differential encoding counterpart is discussed. The robustness of CW-DA-ML against a time-varying frequency offset is also studied. Finally, the necessary ADC resolution for reliable operation is considered. Merits of QPSK, 8-QAM, 8-PSK, 16-QAM, 16-Star, and 16-PSK constellations are examined, and the most favorable constellations are identified.

3.1 CW-DA-ML Estimator

CW-DA-ML estimator is derived, and its implementation, mean-square error (MSE) learning curve, filter-weight adaptation, and optimum filter lengths are analyzed next.

3.1.1 Principle of Operation

DA-ML, which utilizes the reference phasor $U(k+1)$ for carrier estimation, was shown to have a limited ΔfT tolerance in the range of 10^{-3} [98]. Hence, considering the presence of an unknown angular frequency offset $\Delta\omega$, we propose here a new reference phasor $V(k+1)$ to estimate the carrier at time $k+1$ by filtering the immediate past L received samples as

$$V(k+1) = C(k)\mathbf{w}^T(k)\mathbf{y}(k) \quad (3.1)$$

where $\mathbf{w}(k)$ and $\mathbf{y}(k)$

$$\mathbf{w}(k) = [w_1(k), w_2(k), w_3(k), \dots, w_L(k)]^T \quad (3.2)$$

$$\begin{aligned} \mathbf{y}(k) = & [r(k)\hat{m}^*(k), r(k-1)\hat{m}^*(k-1), r(k-2)\hat{m}^*(k-2), \\ & \dots, r(k-L+1)\hat{m}^*(k-L+1)]^T \end{aligned} \quad (3.3)$$

are the L -by-1 filter-weight vector and the L -by-1 filter-input vector at time k , respectively. In Eq. (3.1), $C(k)$ is as per Eq. (2.34) and functions to normalize the magnitude of the reference phasor $V(k+1)$ to ~ 1 in a non-constant modulus signal constellation. Presence of the normalizing factor $C(k)$ and the removal of modulation using decision feedback in the filter input $\mathbf{y}(k)$, makes CW-DA-ML applicable to any arbitrary modulation format.

Momentarily ignoring the phase noise $\theta(k)$ and AWGN $n(k)$ in the received sample $r(k)$ of Eq. (2.21), and assuming an ideal decision feedback of $\hat{m}(k) = m(k)$, the filter input $\mathbf{y}(k)$ in Eq. (3.3) appears as

$$\begin{aligned} \mathbf{y}(k) = & [|m(k)|^2 e^{j\Delta\omega k}, |m(k-1)|^2 e^{j\Delta\omega(k-1)}, |m(k-2)|^2 e^{j\Delta\omega(k-2)}, \\ & \dots, |m(k-L+1)|^2 e^{j\Delta\omega(k-L+1)}]^T. \end{aligned} \quad (3.4)$$

Here, impaired by only the angular frequency offset, consecutive filter-input terms differ by a phase rotation of $\Delta\omega$. The weight vector $\mathbf{w}(k)$ is designed to rotate each

filter-input term to have the same angular frequency offset of $\Delta\omega(k+1)$. This leads to the reference phasor $V(k+1)$ in Eq. (3.1) being angular-frequency-offset aligned with the next received signal $r(k+1) = m(k+1)e^{j\Delta\omega(k+1)}$, thus enabling coherent demodulation.

From Eq. (3.4), it is intuitively clear that $\arg(\mathbf{w}(k))$ should equal $[\Delta\omega, -2\Delta\omega, 3\Delta\omega, \dots, L\Delta\omega]^T$, but $\Delta\omega$ is unknown in practice. Thus, we propose to choose the weights automatically and adaptively at each time k based on the observations $\{r(l), 0 \leq l \leq k\}$ to minimize the sum-of-error-squares cost function $J(k)$,

$$\begin{aligned} J(k) &= \sum_{l=1}^k |e(l)|^2 \\ &= \sum_{l=1}^k \left| \frac{r(l)}{\hat{m}(l)} - C(l-1)\mathbf{w}^T(k)\mathbf{y}(l-1) \right|^2. \end{aligned} \quad (3.5)$$

The error $e(l)$ is the difference between the desired response $r(l)/\hat{m}(l)$ and the reference phasor output of Eq. (3.1) at time $l-1$ using the latest set of filter coefficients $\mathbf{w}(k)$. Minimization of the cost function $J(k)$ forces the phasor $V(l)$ to track the normalized term $r(l)/\hat{m}(l)$, and thus forces $\arg(w_i(k))$ to track $\Delta\omega_i$. Adaptation of filter weights using a least-squares criterion, as opposed to a MSE criterion $\tilde{J}(k) = \mathbb{E}[|e(k)|^2]$, requires no statistical information about the AWGN, phase noise, or frequency offset.

Minimizing $J(k)$ with respect to $\mathbf{w}(k)$, we obtain the optimum filter-weight vector $\hat{\mathbf{w}}(k)$ as the solution of a least-squares normal equation

$$\hat{\mathbf{w}}(k) = \Phi^{-1}(k)\mathbf{z}(k), \quad k \geq 1 \quad (3.6)$$

$$\Phi(k) = \sum_{l=1}^k C^2(l-1)\mathbf{y}^*(l-1)\mathbf{y}^T(l-1) \quad (3.7)$$

$$\mathbf{z}(k) = \sum_{l=1}^k C(l-1) \frac{r(l)}{\hat{m}(l)} \mathbf{y}^*(l-1) \quad (3.8)$$

where $\Phi(k)$ is the L -by- L time-average autocorrelation matrix and $\mathbf{z}(k)$ is the L -by-1 time-average cross-correlation vector. Detailed derivation of $\hat{\mathbf{w}}$ is given in Appendix B. The optimum $\hat{\mathbf{w}}(k)$ can adapt to follow time-varying channels, as it depends on the observations $\{r(l)\}_{l=0}^k$.

An initial preamble of K known symbols is used to aid $\hat{\mathbf{w}}(k)$ to settle to a steady state and for $V(k)$ to acquire tracking of the phasor $e^{j(\theta(k)+\Delta\omega k)}$. Subsequently, the filter operates in decision-directed mode. The structure of CW-DA-ML is shown in Fig. 3.1. Note that the factor $C(k)$ is not necessary in MPSK format and that CW-DA-ML reduces to the classic DA-ML when $\mathbf{w}(k) = [1, 1, \dots, 1]^T$ in Eq. (3.1).

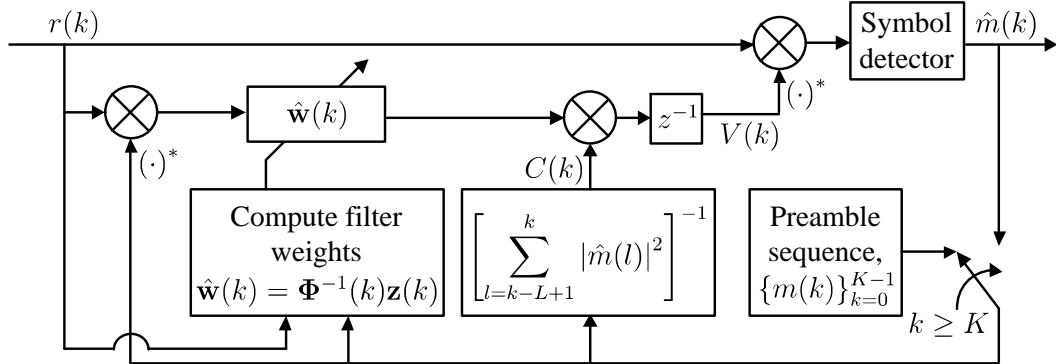


Figure 3.1: CW-DA-ML estimator.

3.1.2 Implementation

The symbol-by-symbol receiver algorithm employing CW-DA-ML is outlined in Table 3.1. In operating the filter of Eq. (3.1), we initialize $V(0) = 1$ and $\hat{\mathbf{w}}(0) = [1, 0, \dots, 0]^T$ to give a maximum gain of one on the first filter input term $r(0)\hat{m}^*(0)$. To guarantee the existence of the inverse of $\Phi(k)$, we ensure that $\Phi(k)$ is nonsingular by initializing $\Phi(0) = \delta\mathbf{I}_L$. Here, \mathbf{I}_L is an L -by- L identity matrix and δ is a small positive constant, e.g., $\delta = 0.01$. Initialization of $\Phi(0)$ with $\delta\mathbf{I}_L$ has no discernible effect on the steady-state performance and convergence behavior of our CW-DA-ML.

Table 3.1: Symbol-by-symbol receiver employing CW-DA-ML

Initialize recursive algorithm at time $k = 0$	
i.	$V(0) = 1$
ii.	$\hat{\mathbf{w}}(0) = [1, 0, 0, \dots, 0]^T$
iii.	$\Phi^{-1}(0) = \delta^{-1} \mathbf{I}_L$
For each iteration, $k = 0, 1, 2, \dots$	
1.	Receiver decision
	$\hat{m}(k) = \arg \max_{0 \leq i \leq M-1} \text{Re} \left[r(k) V^*(k) s_i^* - \frac{1}{2} s_i ^2 \right]$
2.	Preamble sequence, for $0 \leq k \leq K-1$
	$\hat{m}(k) = m(k)$
3.	Form filter input vector
	$\mathbf{y}(k) = [r(k) \hat{m}^*(k), \dots, r(k-L+1) \hat{m}^*(k-L+1)]^T$
4.	Compute intermediate vector, $\psi(k)$, for $k \geq 1$
	$\psi(k) = C(k-1) \Phi^{-1}(k-1) \mathbf{y}^*(k-1)$
5.	Compute gain vector, $\mathbf{g}(k)$, for $k \geq 1$
	$\mathbf{g}(k) = \frac{\psi(k)}{1 + C(k-1) \mathbf{y}^T(k-1) \psi(k)}$
6.	Compute <i>a priori</i> estimation error, $\xi(k)$, for $k \geq 1$
	$\xi(k) = \frac{r(k)}{\hat{m}(k)} - V(k)$
7.	Recursively update filter-weight vector, $\hat{\mathbf{w}}(k)$, for $k \geq 1$
	$\hat{\mathbf{w}}(k) = \hat{\mathbf{w}}(k-1) + \mathbf{g}(k) \xi(k)$
8.	Recursively update inverse correlation matrix, $\Phi^{-1}(k)$, for $k \geq 1$
	$\Phi^{-1}(k) = \text{Tri}\{\Phi^{-1}(k-1) - \mathbf{g}(k) \psi^H(k)\}$
9.	Compute next reference phasor
	$V(k+1) = C(k) \hat{\mathbf{w}}^T(k) \mathbf{y}(k)$

Direct inversion of $\Phi(k)$ at each time k to compute $\hat{\mathbf{w}}(k)$ in Eq. (3.6) is compute-expensive with a complexity order of $O(L^3)$. Hence, we invert $\Phi(k)$ and obtain $\hat{\mathbf{w}}(k)$ recursively using the matrix inversion lemma [52], as summarized by steps 4 to 8 in Table 3.1. See Appendix C for details. Inversion of $\Phi(k)$ at each iteration is now reduced to a scalar division and the entire past observed symbols need not be stored. The

3.1 CW-DA-ML Estimator

matrix $\Phi^{-1}(k)$ is Hermitian, thus only the upper triangle of $\Phi^{-1}(k)$ needs to be computed whereas the lower triangle is obtained through diagonal reflection as signified by the Tri operator in Table 3.1. This reduces the required memory size.

The implementation complexity of Table 3.1 scales as $O(L^2)$ but CW-DA-ML can be equally realized in the form of a recursive lattice filter, further reducing the complexity to $O(L)$ real multiplications and additions per symbol [52]. Use of coordinate rotation digital computers to implement the recursive lattice filter is expected to further simplify the computation as it can perform vector rotations in complex plane efficiently [99].

3.1.3 Mean-Square Error Learning Curve

The MSE of CW-DA-ML given by

$$J'(k) = \mathbb{E} \left[\left| \frac{r(k)}{\hat{m}(k)} - V(k) \right|^2 \right] \quad (3.9)$$

is empirically evaluated in Fig. 3.2 to elucidate the ensemble-average learning properties of CW-DA-ML and, most importantly, the sufficient preamble length K . Here,

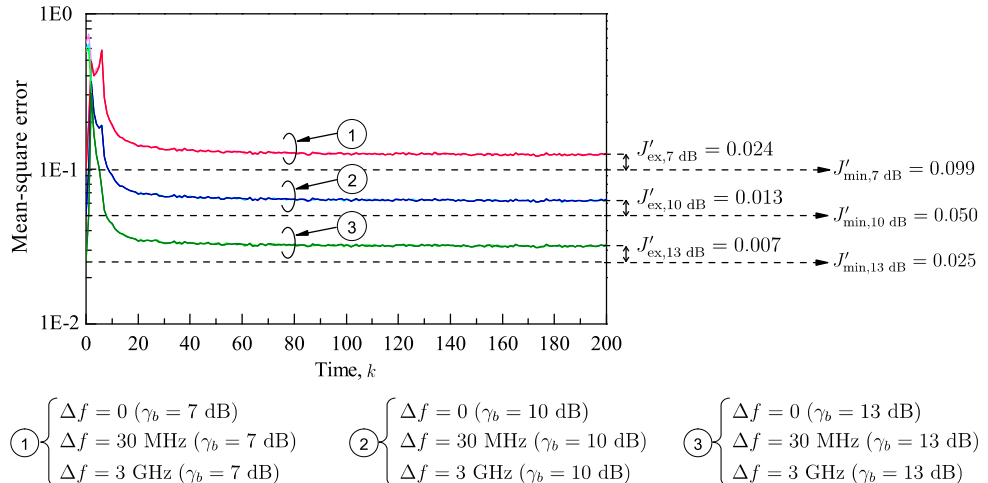


Figure 3.2: Learning curves for CW-DA-ML with different values of Δf and SNR.

QPSK signals are used with $\Delta\nu T_b = 4 \times 10^{-5}$ and $L = 5$. The MSE curves are obtained by averaging $|r(k)/\hat{m}(k) - V(k)|^2$ over 10^4 independent runs at each time point k .

Analytically, the MSE $J'(k)$ can be expanded using Eq.(2.21) into

$$\begin{aligned}
 J'(k) &= \mathbb{E} \left[\left| \frac{m(k)e^{j(\theta(k)+\Delta\omega k)} + n(k)}{\hat{m}(k)} - V(k) \right|^2 \right] \\
 &= \mathbb{E} \left[\left| [e^{j(\theta(k)+\Delta\omega k)} - V(k)] + \frac{n(k)}{m(k)} \right|^2 \right] \\
 &= \mathbb{E} \left[\left| \frac{n(k)}{m(k)} \right|^2 \right] + \mathbb{E} \left[|e^{j(\theta(k)+\Delta\omega k)} - V(k)|^2 \right] \\
 &\quad + \mathbb{E} \left[[e^{j(\theta(k)+\Delta\omega k)} - V(k)] \left[\frac{n(k)}{m(k)} \right]^* \right] + \mathbb{E} \left[[e^{j(\theta(k)+\Delta\omega k)} - V(k)]^* \left[\frac{n(k)}{m(k)} \right] \right]
 \end{aligned} \tag{3.10}$$

where we have assumed ideal decision feedback, i.e., $\hat{m}(k) = m(k)$, in the second step above. The reference phasor $V(k)$ is independent of $n(k)$ and $m(k)$, as $V(k)$ depends only on $\{n(l), m(l)\}_{l=0}^{k-1}$. Additionally, Δf , $\theta(k)$, $n(k)$, and $m(k)$ are assumed to be mutually independent. Hence, the third and fourth terms on the right hand side of Eq. (3.10) amount to zero as $\mathbb{E} \left[\frac{n(k)}{m(k)} \right] = \mathbb{E}[n(k)]\mathbb{E} \left[\frac{1}{m(k)} \right] = 0$. Equation (3.10) then reduces to $J'(k) = J'_{\min} + J'_{\text{ex}}(k)$, where $J'_{\min} = \mathbb{E} [|n(k)/m(k)|^2]$ is the minimum achievable MSE and $J'_{\text{ex}}(k) = \mathbb{E} [|e^{j(\theta(k)+\Delta\omega k)} - V(k)|^2]$ is the excess MSE due to the tracking error of $V(k)$. The J'_{\min} can be expanded as

$$\begin{aligned}
 J'_{\min} &= \mathbb{E} \left[\frac{1}{|m(k)|^2} \right] \mathbb{E} [|n(k)|^2] \\
 &= \mathbb{E} [|m(k)|^2] \mathbb{E} \left[\frac{1}{|m(k)|^2} \right] \frac{\mathbb{E} [|n(k)|^2]}{\mathbb{E} [|m(k)|^2]} \\
 &= \frac{\eta}{\gamma_b \log_2 M}
 \end{aligned} \tag{3.11}$$

where $\eta = \mathbb{E} [|m(k)|^2] \mathbb{E} [1/|m(k)|^2]$ is a unitless constellation penalty [25], whose

value depends on the signal-point arrangement in the constellation. We have η equal to 1 for MPSK and 1.889 for 16-QAM.

Fig. 3.2 includes the computed values of J'_{\min} and J'_{ex} . The fast convergence of CW-DA-ML's learning curve demonstrates that a short preamble of approximately twice the filter length, i.e., $K \approx 2L$, is sufficient to aid $V(k)$ in acquiring tracking of $e^{j(\theta(k)+\Delta\omega k)}$, thus keeping the training overhead cost low. Notably, the excess MSE J'_{ex} is indifferent to varying Δf , attesting that frequency offset estimation by CW-DA-ML is unbiased to the Δf present. Finally, in assessing the tracking capability, we may use the misadjustment criteria \mathcal{M} defined as $\mathcal{M} = J'_{\text{ex}} / J'_{\min}$. The \mathcal{M} of around 0.26 in Fig. 3.2 is slightly high, but this is due to poor choice of filter length L , the effects and importance of which will be further discussed in Section 3.1.4 and 3.1.5.

3.1.4 Adaptation of Filter Weights

The adaptation of the steady-state filter weights $\{\hat{w}_i\}_{i=1}^L$ to different γ_b , $\Delta\nu T_b$, and $\Delta f T$, in CW-DA-ML is analyzed by Fig. 3.3. Here, 16-QAM signals and a filter length of $L = 12$ are used. Each steady-state value is obtained by averaging over 500 runs the average of its value from $k = 50 \times 10^3$ to $k = 51 \times 10^3$ in each run.

The $\Delta\nu T_b$ and γ_b are varied, while the $\Delta f T$ is fixed at 8×10^{-2} , in Fig. 3.3(a). As $\Delta\nu T_b$ and γ_b increases, recent received samples $\{r(l)\}$ are weighted more by $|\hat{w}_i|$ compared to those further back in time, which amounts to a shortening of the filter's effective averaging length. Phase noise $\theta(k)$ becomes less correlated with $\theta(k-l)$ as l or laser linewidth increases. Hence, samples $\{r(l)\}$ further back in time carry less useful information about the phase noise in sample $r(k+1)$ and are weighted less in forming $V(k+1)$. Additionally, increasing γ_b reduces the interval over which additive noise smoothing needs to be performed. However, regardless of the variation in $\Delta\nu T_b$ and γ_b , the phase of the filter weights remain the same.

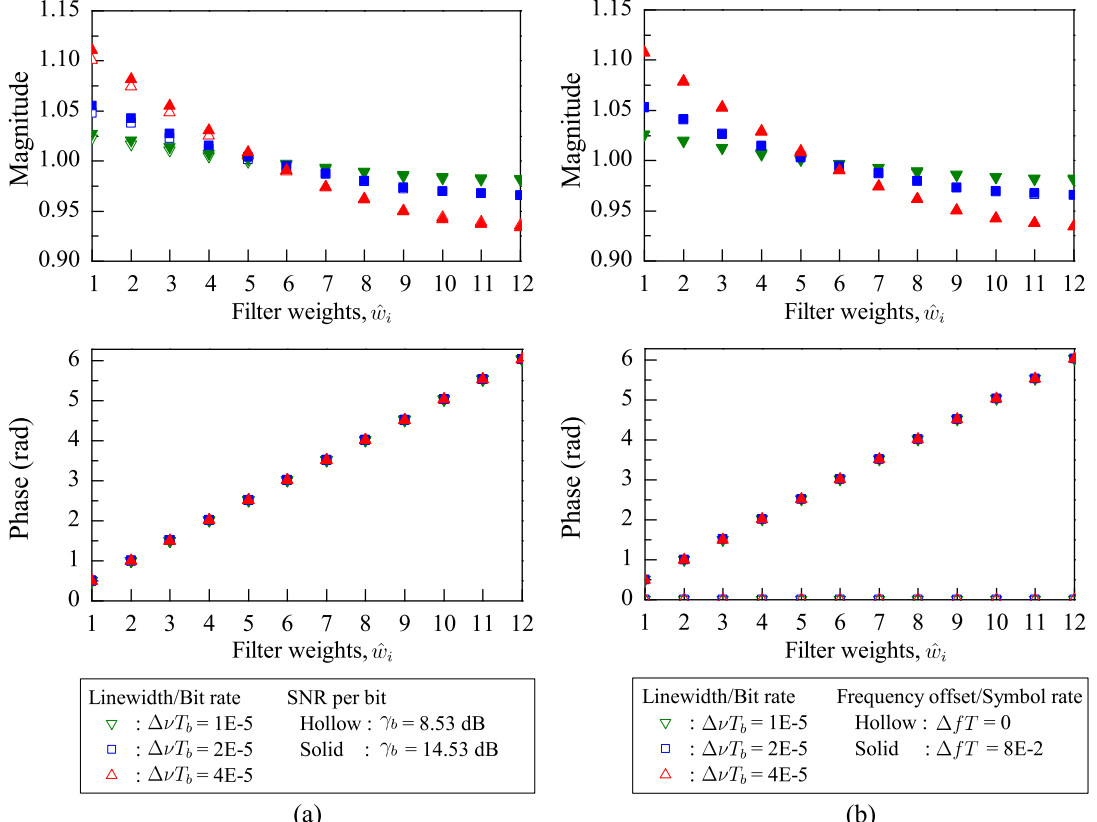


Figure 3.3: Adaptation of steady-state filter weights to different γ_b , $\Delta\nu T_b$, and ΔfT . (a) Different γ_b and $\Delta\nu T_b$, at $\Delta fT = 8 \times 10^{-2}$. (b) Different $\Delta\nu T_b$ and ΔfT , at $\gamma_b = 11.53$ dB.

Next, the $\Delta\nu T_b$ and ΔfT are varied, while the γ_b is kept constant at 11.53 dB, in Fig. 3.3(b). Regardless of the variation in ΔfT , for a given $\Delta\nu T_b$, the magnitude of the filter weights remain the same. However, the phase of the filter weights converges to the pattern of $2\pi[\Delta fT, 2\Delta fT, \dots, L\Delta fT]$ depending on the frequency offset present, as expected. We can conclude from Fig. 3.3 that the magnitude of the weight, $|\hat{w}_i|$, responds to $\Delta\nu T_b$ and γ_b in weighting down less-relevant samples, whereas the phase of the weight, $\arg(\hat{w}_i)$, responds to ΔfT in correcting for the frequency offset. Hence, given convergence of $\arg(\hat{w}_i)$ to $2\pi\Delta fTi$, the optimum filter length is only dependent upon $\Delta\nu T_b$ and γ_b .

3.1.5 Optimum Filter Length

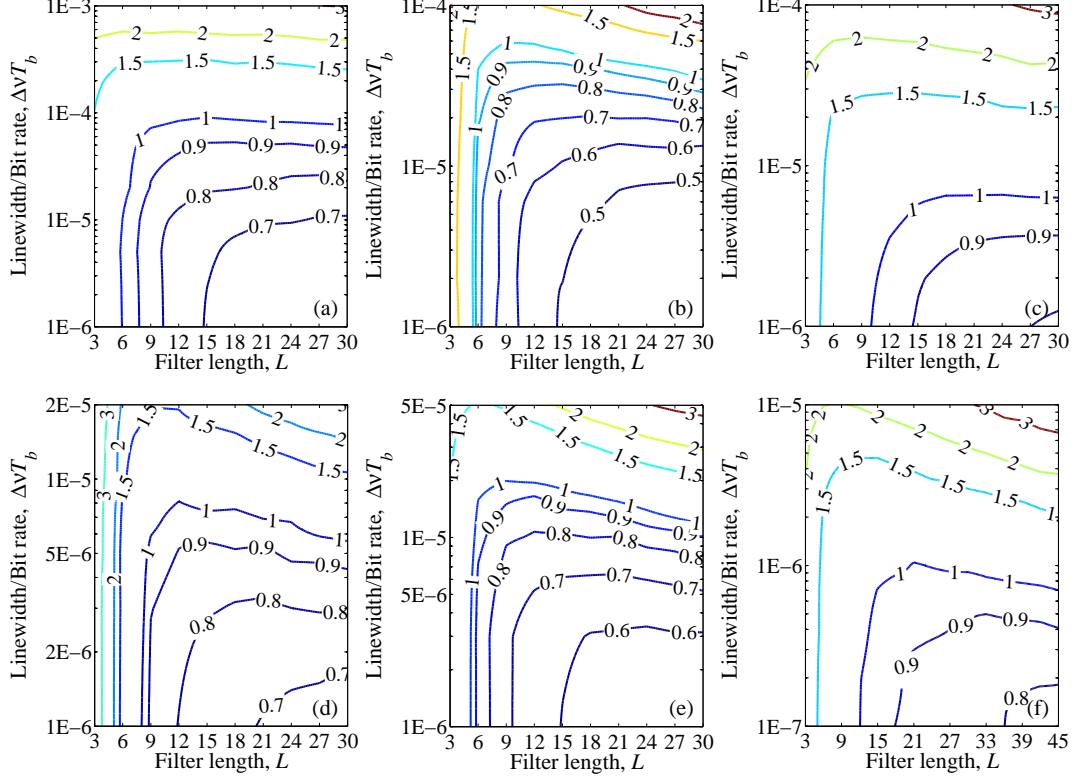


Figure 3.4: SNR per bit penalty of CW-DA-ML at $\text{BER} = 10^{-3}$ versus $\Delta\nu T_b$ and filter length for (a) QPSK, (b) 8-QAM, (c) 8-PSK, (d) 16-QAM, (e) 16-Star, and (f) 16-PSK.

In general, there is a trade-off between the need for long filter lengths to average over AWGN and the need for short filter lengths to average over phase noise. Contour plots of γ_b penalty at $\text{BER} = 10^{-3}$ on a $\Delta\nu T_b$ versus filter length map are drawn in Fig. 3.4 for CW-DA-ML. The contour plots confirm that the optimum filter length decreases with $\Delta\nu T_b$ and there is a minimum filter length even in the absence of phase noise. For comprehensiveness, we provide the contour plots of MPE in Fig. 3.5. Optimum filter lengths at a 1-dB γ_b penalty for CW-DA-ML and MPE are given in Table 3.2. These optimum filter lengths are used for all ensuing analyses in this chapter. For comparison purposes, the optimum filter length of CW-DA-ML will also be used

3.1 CW-DA-ML Estimator

for DA-ML in all subsequent analyses in this chapter.

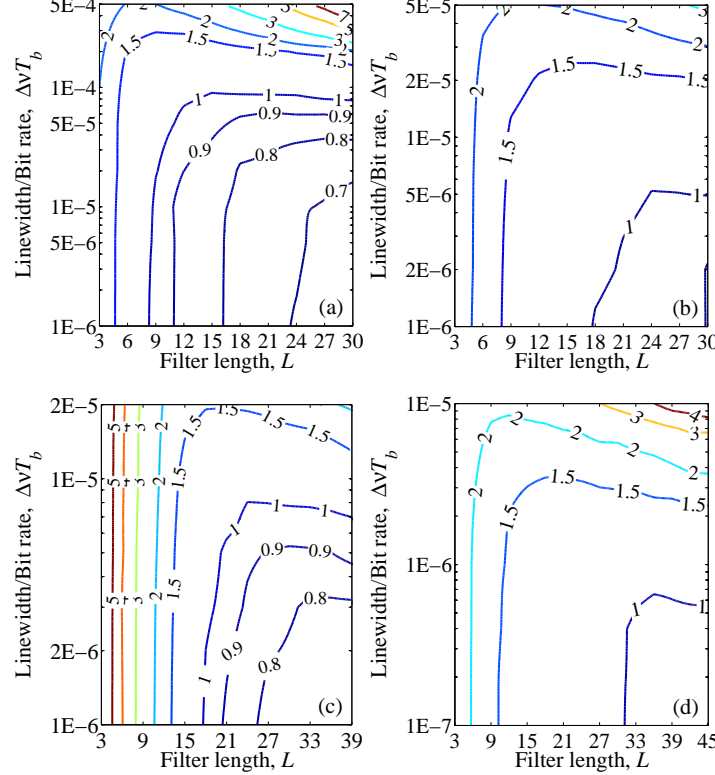


Figure 3.5: SNR per bit penalty of DiffFE-MPE at $\text{BER} = 10^{-3}$ versus $\Delta\nu T_b$ and filter length for (a) QPSK, (b) 8-PSK, (c) 16-QAM, and (d) 16-PSK.

Table 3.2: Optimal filter length for 1-dB γ_b penalty at $\text{BER} = 10^{-3}$

Format	MPE	CW-DA-ML
QPSK	15	15
8-QAM	-	9
8-PSK	24	18
16-QAM	24	12
16-Star	-	9
16-PSK	36	21

3.2 Performance Analysis

The CW-DA-ML is compared with FFTFE-MPE and DiffFE-MPE in terms of: (i) laser linewidth tolerance, (ii) frequency offset estimation range, (iii) acquisition time, accuracy, and SNR threshold, and (iv) cycle slip probability.

3.2.1 Laser Linewidth Tolerance

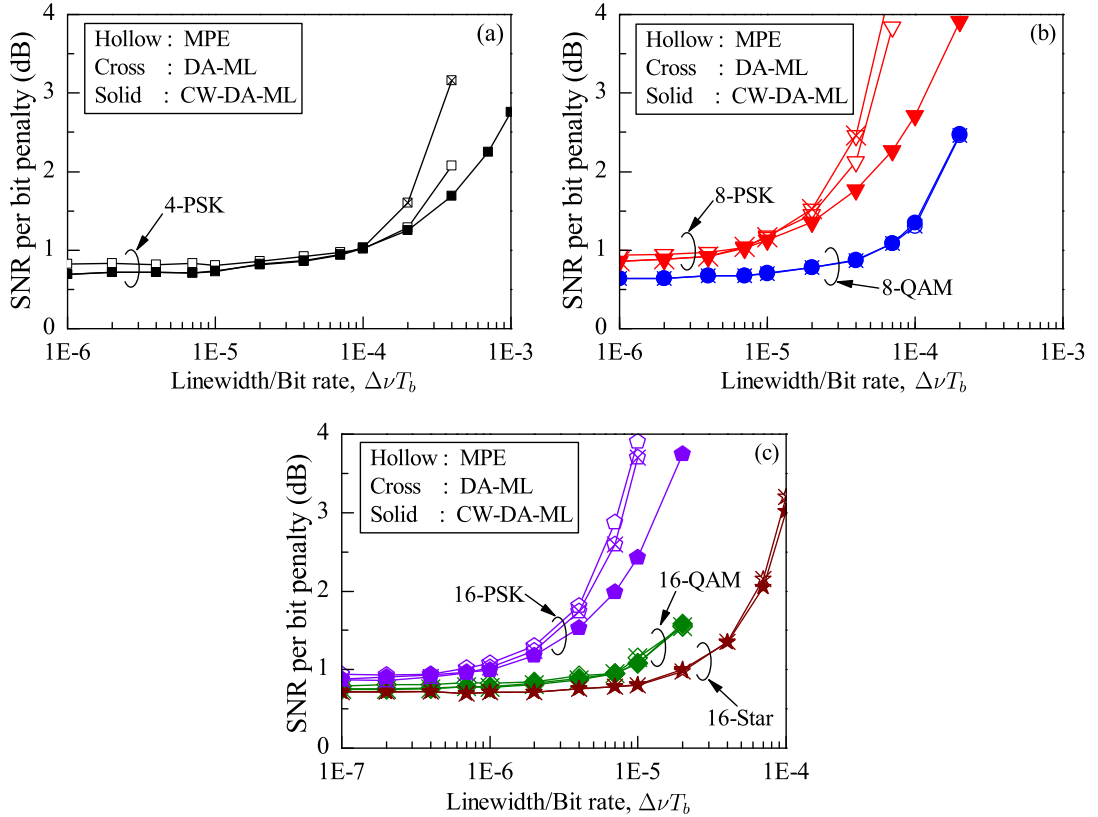


Figure 3.6: Laser linewidth tolerance of carrier estimators for (a) 4-, (b) 8-, and (c) 16-point constellations.

The SNR per bit penalty versus linewidth per bit rate for CW-DA-ML is plotted in Fig. 3.6. Here, without loss of generality, we set $\Delta f = 0$. The tolerable $\Delta\nu T_b$ values for a 1-dB γ_b penalty at BER of 10^{-3} are summarized in Table 3.3. Sorted in order of decreasing $\Delta\nu T_b$ tolerance, we have 4-PSK, 8-QAM, 16-Star, 16-QAM, 8-PSK, and 16-PSK. It is interesting to note that 16-QAM achieves similar $\Delta\nu T_b$ tolerance as

3.2 Performance Analysis

Table 3.3: $\Delta\nu T_b$ tolerance for 1-dB γ_b penalty at $\text{BER} = 10^{-3}$

Format	MPE	DA-ML	CW-DA-ML
QPSK	9.0×10^{-5}	8.8×10^{-5}	9.0×10^{-5}
8-QAM	-	5.8×10^{-5}	5.8×10^{-5}
8-PSK	5.3×10^{-6}	5.8×10^{-6}	6.5×10^{-6}
16-QAM	8.0×10^{-6}	7.7×10^{-6}	8.0×10^{-6}
16-Star	-	2.0×10^{-5}	2.0×10^{-5}
16-PSK	6.5×10^{-7}	9.0×10^{-7}	1.1×10^{-6}

8-PSK and yet occupies $1/12T_b$ less spectral width. As argued extensively in [100], 16-Star ($\phi_{\min} = \pi/4$) has greater $\Delta\nu T_b$ tolerance than 16-QAM ($\phi_{\min} = 0.20\pi$ & $\pi/2$) by virtue of its larger ϕ_{\min} . Since 16-Star ($d_{\min} = 0.534$) has poorer packing density than 16-QAM ($d_{\min} = 0.632$), it generally requires higher γ_b and thus only attractive for $\Delta\nu T_b \geq 2.75 \times 10^{-5}$ as depicted in Fig. 3.7. Similar conclusion holds for other 16-point ring constellations considered in [101] which offer moderate advantage in terms of $\Delta\nu T_b$ tolerance but at the expense of poor packing density, increased transmitter complexity, and differential encoding complexity, compared to 16-QAM.

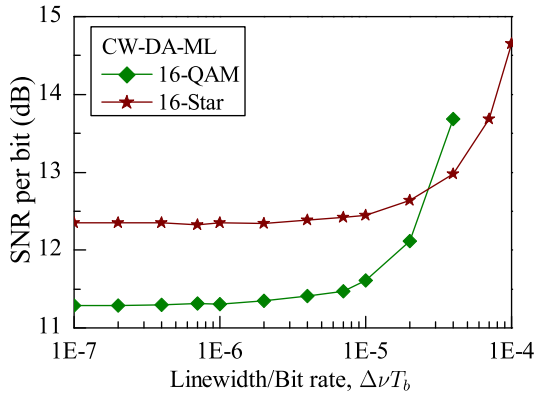


Figure 3.7: Laser linewidth tolerance of 16-QAM and 16-Star, using CW-DA-ML. Here, $\Delta f = 0$.

From Fig. 3.6 and Table 3.3, it is seen that CW-DA-ML equals or outperforms DA-ML in terms of $\Delta\nu T_b$ tolerance, even when $\Delta f = 0$. This is because DA-ML

3.2 Performance Analysis

weighs all filter inputs equally, i.e., $\mathbf{w}(k) = [1, 1, \dots, 1]^T$, but CW-DA-ML weighs the samples in a decaying manner resulting in a better phase estimate. Although MPE has an inherent advantage of using both past and future samples (i.e., noncausal), CW-DA-ML which only uses past samples (i.e., causal) still matches MPE's performance in QPSK and 16-QAM, whereas outperforms MPE in 8- and 16-PSK.

3.2.2 Frequency Offset Tolerance

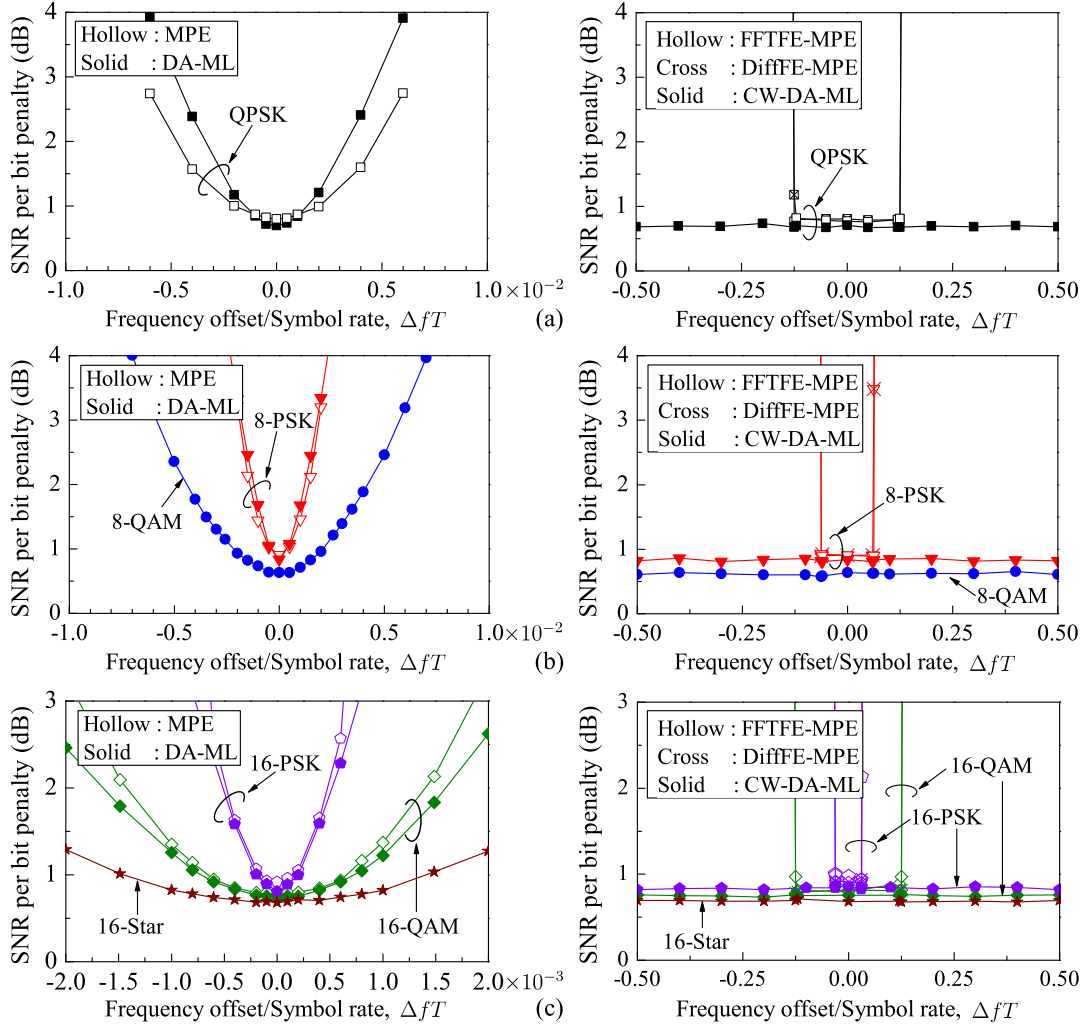


Figure 3.8: Frequency offset tolerance of carrier estimators for (a) 4-, (b) 8-, and (c) 16-point constellations.

Fig. 3.8 shows the frequency-offset-per-symbol-rate estimation range of MPE,

3.2 Performance Analysis

DA-ML, FFTFE-MPE, DiffFE-MPE, and CW-DA-ML, while keeping $\Delta\nu = 0$. The maximum tolerable ΔfT by MPE, with filter length L , is limited by the $\arg(\cdot)/M$ operation to $\pm 1/2LM$ in the absence of phase noise and AWGN. The limited ΔfT tolerance of MPE and DA-ML at 1-dB γ_b penalty, as summarized in Table 3.4, reiterates the need to incorporate a dedicated frequency offset estimation capability into carrier estimators. MPE and DA-ML are only suitable for $\Delta fT \leq \pm 2.1 \times 10^{-3}$. Frequency offset intolerance of MPE and DA-ML originates from the violation of the assumption that all their filter-input terms have identical angular frequency offsets.

Table 3.4: ΔfT tolerance for 1-dB γ_b penalty at $\text{BER} = 10^{-3}$ and $\Delta\nu = 0$

Format	MPE	DA-ML	FFTFE-MPE	DiffFE-MPE	CW-DA-ML
QPSK	$\pm 2.0 \times 10^{-3}$	$\pm 1.5 \times 10^{-3}$	$\pm 1/8$	$\pm 1/8$	$\pm 1/2$
8-QAM	-	$\pm 2.1 \times 10^{-3}$	-	-	$\pm 1/2$
8-PSK	$\pm 0.4 \times 10^{-3}$	$\pm 0.4 \times 10^{-3}$	$\pm 1/16$	$\pm 1/16$	$\pm 1/2$
16-QAM	$\pm 6.5 \times 10^{-4}$	$\pm 0.7 \times 10^{-3}$	$\pm 1/8$	$\pm 1/8$	$\pm 1/2$
16-Star	-	$\pm 1.4 \times 10^{-3}$	-	-	$\pm 1/2$
16-PSK	$\pm 1.5 \times 10^{-4}$	$\pm 0.2 \times 10^{-3}$	$\pm 1/32$	$\pm 1/32$	$\pm 1/2$

FFTFE and DiffFE raises the received samples to their M th power in MPSK format and to the 4th power in 16-QAM format to remove the information-bearing phase. This limits their ΔfT estimation range to a format-dependent $\pm 1/2M$ and $\pm 1/8$ in MPSK and 16-QAM, respectively. On the other hand, CW-DA-ML achieves a complete ΔfT estimation range of $\pm 1/2$, as it uses reference phasor with a complete phase tracking range of $[0, 2\pi]$. FFTFE, DiffFE, and MPE need to be modified separately according to the constellation used, rendering them less attractive in flexible optical systems using multiple modulation formats. Moreover, FFTFE, DiffFE, and MPE are limited to MPSK and 16-QAM formats, in contrast to the format-independent CW-DA-ML.

3.2.3 Acquisition Time, Accuracy, and SNR Threshold

The performance of carrier estimators is determined by the total phase error and not by the error in individual phase and frequency estimates. Fig. 3.9 plots the total-phase-error variance against the received sample size N used to compute the frequency estimate. Here, the true $\Delta fT = 0.1$. For CW-DA-ML, N represents the received samples over which $\hat{\mathbf{w}}$ is updated. The error variance at each sample size N is obtained as $\sigma_\varepsilon^2 = (1/l) \sum_{i=1}^l |\vartheta_i(N) - \hat{\vartheta}_i(N)|^2$ by averaging over $l = 900$ independent realizations. Here, $\vartheta_i(N) = \arg(r_i(N))$ is the total phase of the N th received sample in the i th realization and $\hat{\vartheta}_i(N)$ is the corresponding estimate. To comprehensively study the frequency acquisition time and accuracy of each carrier estimator (FFTFE-MPE, DiffFE-MPE, CW-DA-ML), 3 different scenarios are simulated for each modulation format (QPSK, 8-QAM, 16-QAM) in Fig. 3.9 as follows:

1. Error variance is plotted for a 1-dB penalty at $\text{BER} = 10^{-3}$, using: $\gamma_b = 7.82$ dB and $\Delta\nu T_b = 9.0 \times 10^{-5}$ for QPSK; $\gamma_b = 10.04$ dB and $\Delta\nu T_b = 5.8 \times 10^{-5}$ for 8-QAM; $\gamma_b = 11.53$ dB and $\Delta\nu T_b = 8.0 \times 10^{-6}$ for 16-QAM.
2. Scenario 1 is repeated with γ_b reduced by 3 dB.
3. Scenario 1 is repeated with $\Delta\nu T_b$ reduced by an order of magnitude.

The error variance decreases initially with N due to improving frequency estimate accuracy but reaches an error floor limited by AWGN and laser phase noise. The carrier acquisition time, defined as the N required for σ_ε^2 to reach within 3% of the error floor, is summarized in Table 3.5. CW-DA-ML is 2.5 and 10.5 times faster than DiffFE-MPE in QPSK and 16-QAM, respectively, for a 1-dB γ_b penalty at a BER of 10^{-3} . This can be ascribed to the fast-converging least-squares technique of CW-DA-ML [52]. Additionally, CW-DA-ML uses all N samples for frequency estimation in 16-QAM unlike DiffFE-MPE which only uses $N/2$ samples as the probability of a pair of consecutive Class I symbols is 1/4. Although FFTFE has the shortest frequency-acquisition time, we shall later see that it is undesirable for reasons described in Section 3.2.4. Notably,

3.2 Performance Analysis

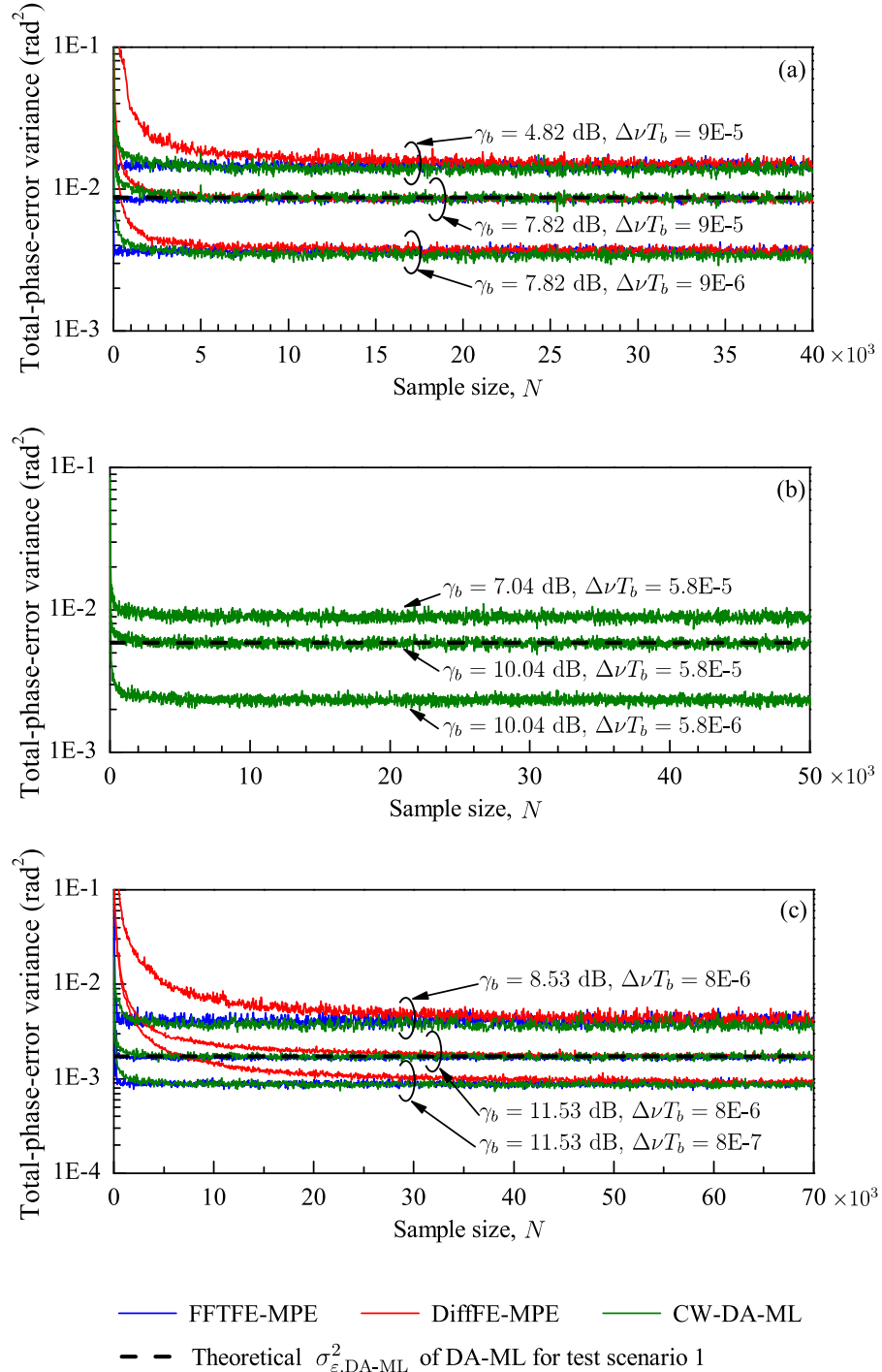


Figure 3.9: Frequency acquisition time and accuracy of FFTFE-MPE, DiffFE-MPE, and CW-DA-ML for (a) QPSK, (b) 8-QAM, and (c) 16-QAM.

3.2 Performance Analysis

Table 3.5: Carrier acquisition time

Format	SNR per bit, γ_b (dB)	Linewidth/ Bit rate, $\Delta\nu T_b$	Sample size, N		
			FFTFE-MPE	DiffFE-MPE	CW-DA-ML
QPSK	4.82	9.0×10^{-5}	165	30×10^3	5×10^3
	7.82	9.0×10^{-5}	45	10×10^3	4×10^3
	7.82	9.0×10^{-6}	45	15×10^3	6×10^3
8-QAM	7.04	5.8×10^{-5}	-	-	4×10^3
	10.04	5.8×10^{-5}	-	-	3×10^3
	10.04	5.8×10^{-6}	-	-	4×10^3
16-QAM	8.53	8.0×10^{-6}	528	58×10^3	5×10^3
	11.53	8.0×10^{-6}	360	42×10^3	4×10^3
	11.53	8.0×10^{-7}	360	54×10^3	5×10^3

the variation in frequency acquisition time with different modulation formats is much smaller in CW-DA-ML than in FFTFE and DiffFE, thanks to CW-DA-ML's format independence.

Lowering the SNR ($\Delta\nu T_b$) increases (decreases) the error floor, as expected. With the decrease in SNR, speed of CW-DA-ML over DiffFE-MPE increased to 6 and 11.6 times in QPSK and 16-QAM, respectively. The convergence time decreases with SNR and $\Delta\nu T_b$, hence a smaller sample size N is sufficient at higher SNR or higher $\Delta\nu T_b$. An exception to this is FFTFE, whose convergence time remains unchanged with variation in $\Delta\nu T_b$. This is because the peak position in the FFT spectrum, and thus its frequency estimate accuracy, remains unaffected as variation in $\Delta\nu T_b$ merely alters the spectral width around the peak.

The dashed line in Fig. 3.9 for each modulation format, depicts the theoretical error variance of DA-ML at $\Delta f = 0$ computed using [102]

$$\sigma_{\varepsilon, \text{DA-ML}}^2 \approx \frac{2L^2 + 3L + 1}{6L} \sigma_p^2 + \frac{1}{2L\gamma_b \log_2 M} \quad (3.12)$$

3.2 Performance Analysis

for test scenario 1. A value of $L = 15, 9$, and 12 was used in Eq. (3.12) for QPSK, 8-QAM, and 16-QAM format, respectively. A similar error floor achieved by CW-DA-ML demonstrates the near-ideal frequency estimation by our estimator. Equation (3.12) can thus be used as a quick approximation of the error floor achievable by CW-DA-ML.

Fig. 3.10 illustrates the error variance versus γ_b of FFTFE-MPE, DiffFE-MPE, and CW-DA-ML in QPSK, 8-QAM, and 16-QAM using different values of N and a ΔfT of 0.1 . CW-DA-ML achieves superior or equal frequency estimation accuracy compared to DiffFE-MPE at any given N and γ_b . This can be attributed to the L -sample lag autocorrelation used in CW-DA-ML [see Eq. (3.7)] which is more resilient to AWGN compared to the 1-sample lag autocorrelation used in DiffFE. CW-DA-ML tends to outperform FFTFE-MPE, and is therefore a better option, at low SNR and/or low N . Low SNR increases the occurrence of outliers and low N reduces the frequency-estimate resolution of FFTFE. Furthermore, CW-DA-ML does not exhibit sharp SNR threshold but rather a gradual deterioration of error variance with decreasing SNR. As the error variance is a decreasing function of N , CW-DA-ML can operate at low SNR by adequately increasing N .

3.2.4 Continuous versus Periodic Tracking

In FFTFE and DiffFE, the frequency estimate becomes available only at the N th time point. Hence, the first N received samples need to be frequency-corrected retrospectively at time point N , resulting in a huge processing bottleneck. Alternatively, the first N samples may be treated as a training sequence at the expense of a large overhead. For example, from Table 3.5, $N = 360$ and 42×10^3 in 16-QAM for FFTFE-MPE and DiffFE-MPE, respectively. In contrast, CW-DA-ML requires merely $2L$ samples as preamble sequence [103] and thus has a smaller overhead, e.g., 24 samples in 16-

3.2 Performance Analysis

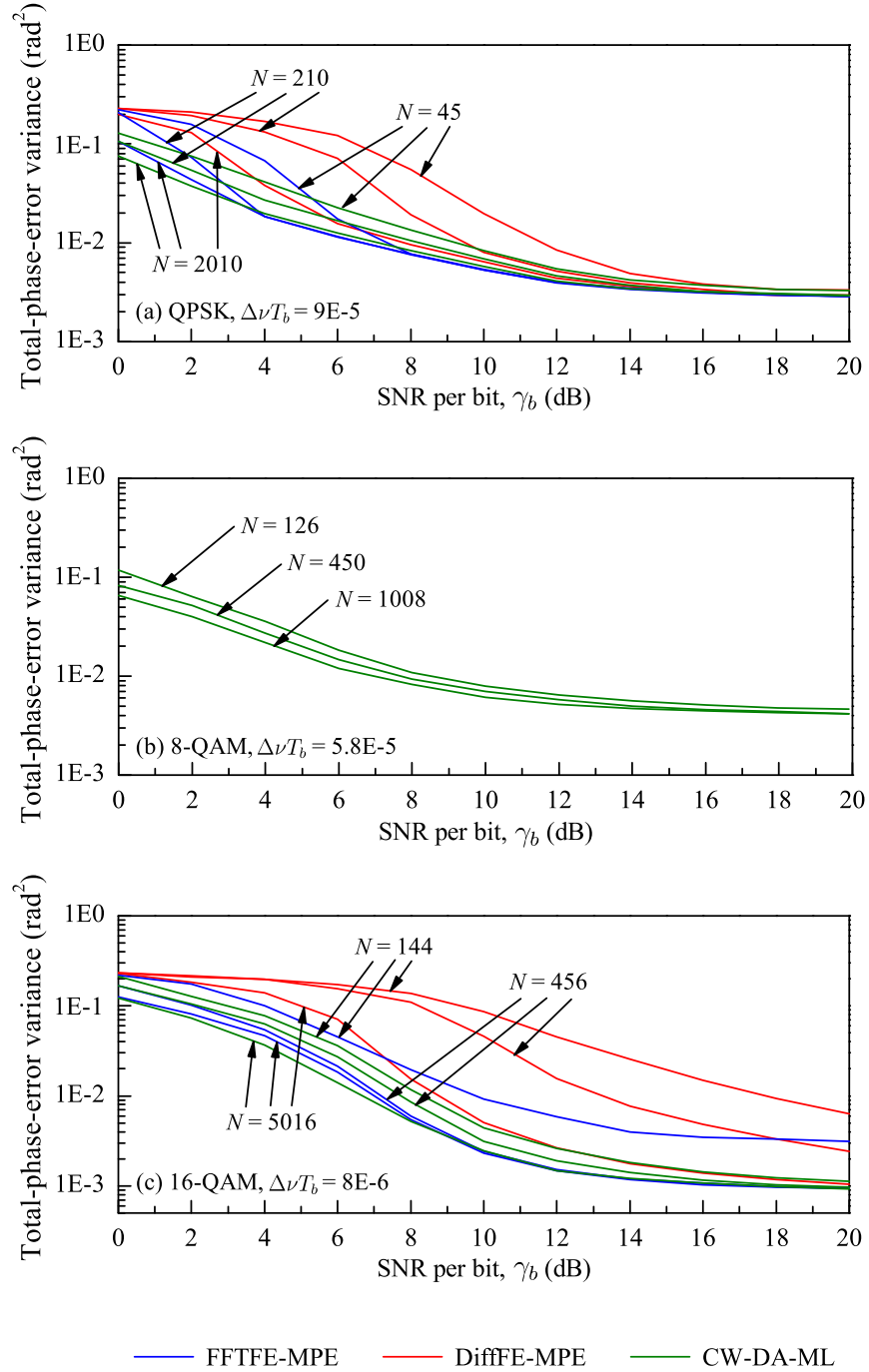


Figure 3.10: Error variance versus γ_b with different sample size N for frequency estimation in (a) QPSK, (b) 8-QAM, and (c) 16-QAM.

QAM with $L = 12$.

In practice, the frequency offset varies with time and needs to be tracked. However, FFTFE-MPE and DiffFE-MPE can only produce periodically-updated static frequency estimates, and is likely to incur some penalty as a result. Moreover, they will incur a large processing bottleneck or a large overhead each time the frequency is re-estimated. It is desirable to track the time-varying frequency offset continuously, such as the symbol-by-symbol CW-DA-ML estimator, to ensure best performance.

3.2.5 Cycle Slip Probability

When AWGN, phase noise, and/or frequency offset pushes the carrier estimate from the true stable operating point into the domain of attraction of a neighboring stable operating point, a cycle slip is said to have occurred. The estimate remains in the vicinity of the new stable operating point, causing a large error burst, until another cycle slip occurs. Angular spacing of the stable operating points φ concur with that of the rotationally symmetric positions of the constellation. We have φ equal to $2\pi/M$ in MPSK, $\pi/4$ in 16-Star, and $\pi/2$ in 8- and 16-QAM constellations.

The highly nonlinear phenomenon of cycle slip, and resulting error burst, can be confined to the slip duration by using differential encoding [104]. However, differential encoding is undesirable for it increases the BER through correlated errors and hinders the use of powerful soft decision (SD) forward error correction (FEC) codes with high coding gain [105]. Alternatively, cycle slip can be mitigated by inserting pilot symbols at a frequency greater than the cycle slip probability. In PA system, a low cycle slip probability is preferred to minimize the required pilot overhead. Detection of cycle slip follows the technique in [106], where 11 or more consecutive symbol errors are assumed to be due to a cycle slip.

A cycle slip of $\pi/2$ and $\pi/8$ by CW-DA-ML in 16-QAM and 16-PSK signals,

3.2 Performance Analysis

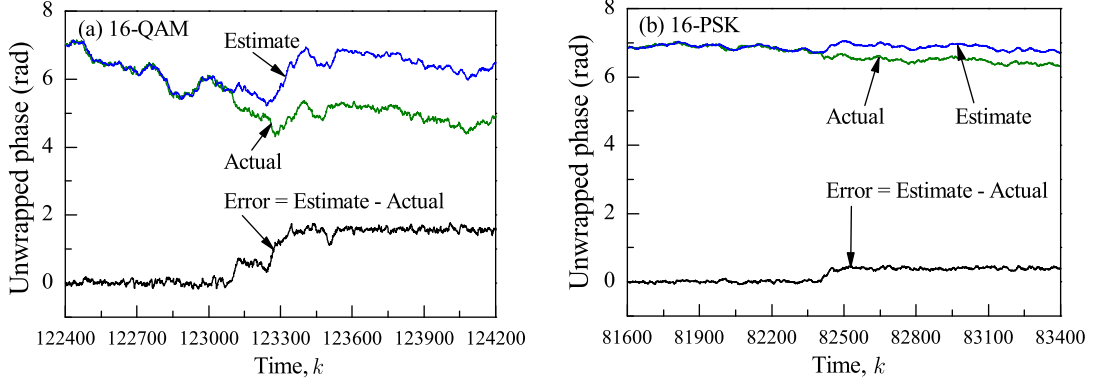


Figure 3.11: Cycle slip in CW-DA-ML for (a) 16-QAM, and (b) 16-PSK signals.

respectively, are shown in Fig. 3.11, where $\Delta f = 0$ for better visualization. It is key to note that the cycle slip in 16-QAM transitioned through an intermediate state of 0.20π rotation before settling at the stable point spaced away by $\pi/2$. An example of this trajectory could be from the domain of point s_9 to s_2 to s_1 of the 16-QAM constellation shown in Fig. 2.1(d).

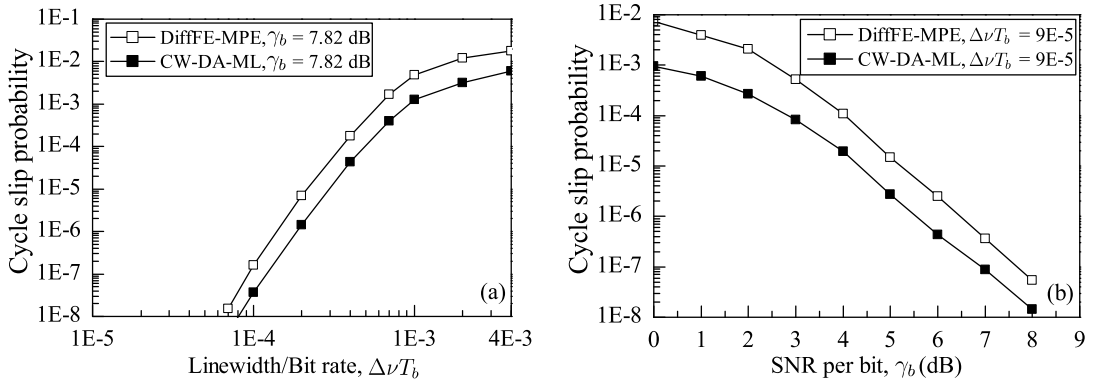


Figure 3.12: Cycle slip probability of CW-DA-ML and DiffFE-MPE for QPSK signal versus (a) $\Delta\nu T_b$, and (b) γ_b .

The cycle slip probability of DiffFE-MPE and CW-DA-ML for QPSK signal is plotted against $\Delta\nu T_b$ in Fig. 3.12(a) and against γ_b in Fig. 3.12(b). The γ_b is fixed at 1 dB above its theoretical value for $\text{BER} = 10^{-3}$ in Fig. 3.12(a), and the $\Delta\nu T_b$ is fixed at 9×10^{-5} in Fig. 3.12(b). The cycle slip probability is an increasing function

3.2 Performance Analysis

of laser phase noise and a decreasing function of SNR. CW-DA-ML has a lower cycle slip probability than DiffFE-MPE. For example, at $\gamma_b = 7.82$ dB and $\Delta\nu T_b = 9 \times 10^{-5}$, CW-DA-ML achieves a lower cycle slip probability of 2×10^{-8} compared to the 8×10^{-8} of DiffFE-MPE. Cycle slip is induced in CW-DA-ML by the use of erroneous symbol decisions when forming the reference phasor in Eq. (3.1). However, cycle slip in DiffFE-MPE is caused by inaccurate phase unwrapping in MPE. Due to MPE's modulo $2\pi/q$ operation, its phase estimate $\hat{\theta}(k)$ needs to be unwrapped to track the true laser phase noise trajectory. The unwrap function selects $\hat{\theta}(k) \pm 2\pi i/q$ where $i \in \{0, 1, 2, \dots\}$, such that $\hat{\theta}(k) - \hat{\theta}(k-1)$ is within $\pm\pi/q$. However, if the true $|\theta(k) - \theta(k-1)|$ was greater than π/q , a cycle slip will occur. Increased $\Delta\nu T_b$ and reduced SNR makes accurate phase unwrapping difficult, and contributes to unwrapping errors as witnessed in Fig. 3.12.

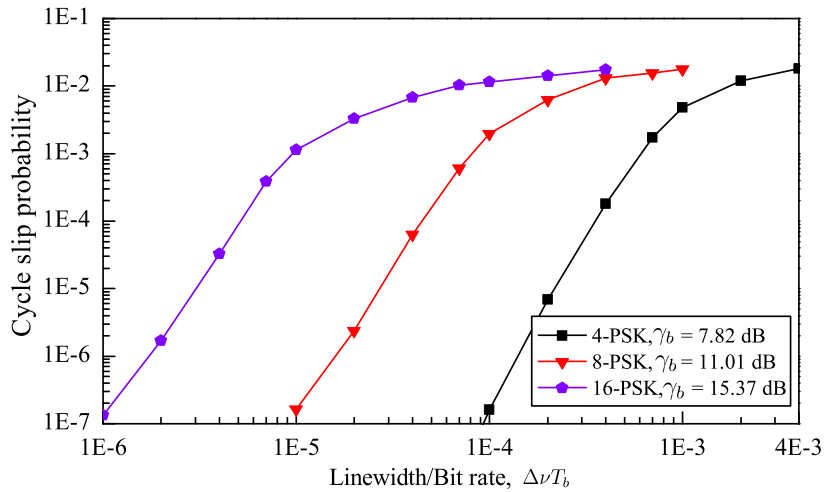


Figure 3.13: Cycle slip probability of DiffFE-MPE versus $\Delta\nu T_b$.

Besides SNR and $\Delta\nu T_b$, the size of the basic unwrapping interval also contributes to the cycle slip probability. In Fig. 3.13, the cycle slip probability of DiffFE-MPE for 4-, 8-, and 16-PSK signals are plotted at 1 dB above their respective theoretical γ_b values for $\text{BER} = 10^{-3}$. As M increases at a given $\Delta\nu T_b$, it is more likely for the true $|\theta(k) - \theta(k-1)|$ to exceed π/q , thus increasing the cycle slip probability. Moreover,

3.2 Performance Analysis

introduction of higher powers of noise with modulation order M by MPE [95] compounds the angular uncertainty of the received sample, making cycle slips more likely. Therefore, MPE based carrier estimators, such as DiffFE-MPE and FFTFE-MPE, are less desirable in practical PA systems than CW-DA-ML due to their higher cycle slip probability.

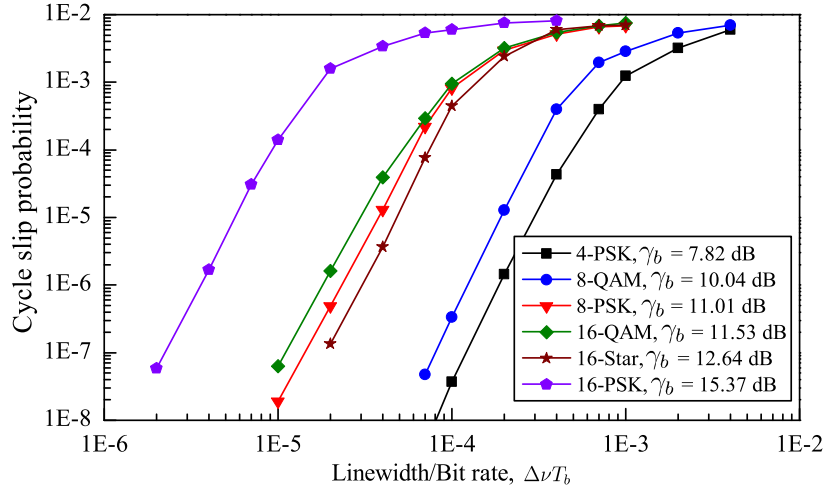


Figure 3.14: Cycle slip probability of different modulation formats versus $\Delta\nu T_b$.

Suitability of various modulation formats in terms of cycle slip probability is investigated in Fig. 3.14 using CW-DA-ML. Each modulation format was simulated at 1 dB above its theoretical γ_b value for $\text{BER} = 10^{-3}$. Sorted in order of increasing cycle slip probability, we have QPSK ($\varphi = \pi/2$), 8-QAM ($\varphi = \pi/2$), 16-Star ($\varphi = \pi/4$), 8-PSK ($\varphi = \pi/4$), 16-QAM ($\varphi = \pi/2$), and 16-PSK ($\varphi = \pi/8$). This order follows the pattern of constellations with larger angular separation of stable operating points φ having a lower cycle slip probability, with the exception of 16-QAM. The irregularity can be explained by recalling that cycle slip in 16-QAM tends to occur through an intermediate state spaced apart by 0.20π which is smaller than $\varphi = \pi/4$ of 8-PSK. Hence, it is more likely for 16-QAM to incur cycle slips compared to 8-PSK. In terms of cycle slip tolerance, best 4-, 8-, and 16-point constellations are 4-PSK, 8-QAM, and 16-Star, respectively. However, we should remember that a higher SNR and a more

complex transmitter is required for 16-Star than 16-QAM.

3.3 Pilot-Assisted Carrier Estimation

Cycle slips can be combated using differential encoding or pilot symbols. PA carrier estimation is preferred in practice for it avoids the differential encoding penalty listed in Table 2.1, enables the use of powerful SD FEC codes with high coding gain, and can be simultaneously used for fiber nonlinearity compensation. In PA carrier estimation, alternating D -symbol-long data and P -symbol-long pilot sequences are transmitted. When data are transmitted in packet frames, headers containing protocols such as the physical addresses of the receiver and FEC information can be used as pilot symbols. The additional energy of pilot symbols is accounted for in our simulation by computing the effective launched energy of each symbol $E_{s,eff}$ as $E_{s,eff} = E_{s,act} \cdot (D + P)/D$. Here, $E_{s,act}$ is the actual energy of each transmitted symbol.

Fig. 3.15 shows the γ_b penalty of PA CW-DA-ML at $BER = 10^{-3}$ with different overhead costs, defined as $P/(D + P)$. As the ratio $(D + P)/D$ decreases toward 1, the $E_{s,act}$ approaches $E_{s,eff}$, hence the receiver sensitivity improves. In Fig. 3.15, the $\Delta\nu T_b$ is set at the tolerance value for a 1-dB γ_b penalty in a differential-encoding system as listed in Table 3.3. Therefore, the PA system with $D = 10^4$ and $P = 20$, achieves a gain of 0.57, 0.30, and 0.13 dB in QPSK, 8-QAM, and 16-QAM, respectively, over its differential-encoding counterpart, while keeping the overhead cost low at 0.2%.

In Fig. 3.15, the improvement in receiver sensitivity levels off for $D \geq 10^4$, indicating negligible error propagation arising from a low cycle slip probability. We can infer that the mean time to lose lock (i.e., cycle slip) is greater than 10^5 symbols. This is proven in Fig. 3.16 by the negligible performance loss with actual, compared to ideal, decision feedback for $BER \leq 10^{-3}$ at $D = 10^5$ and $P = 20$.

3.3 Pilot-Assisted Carrier Estimation

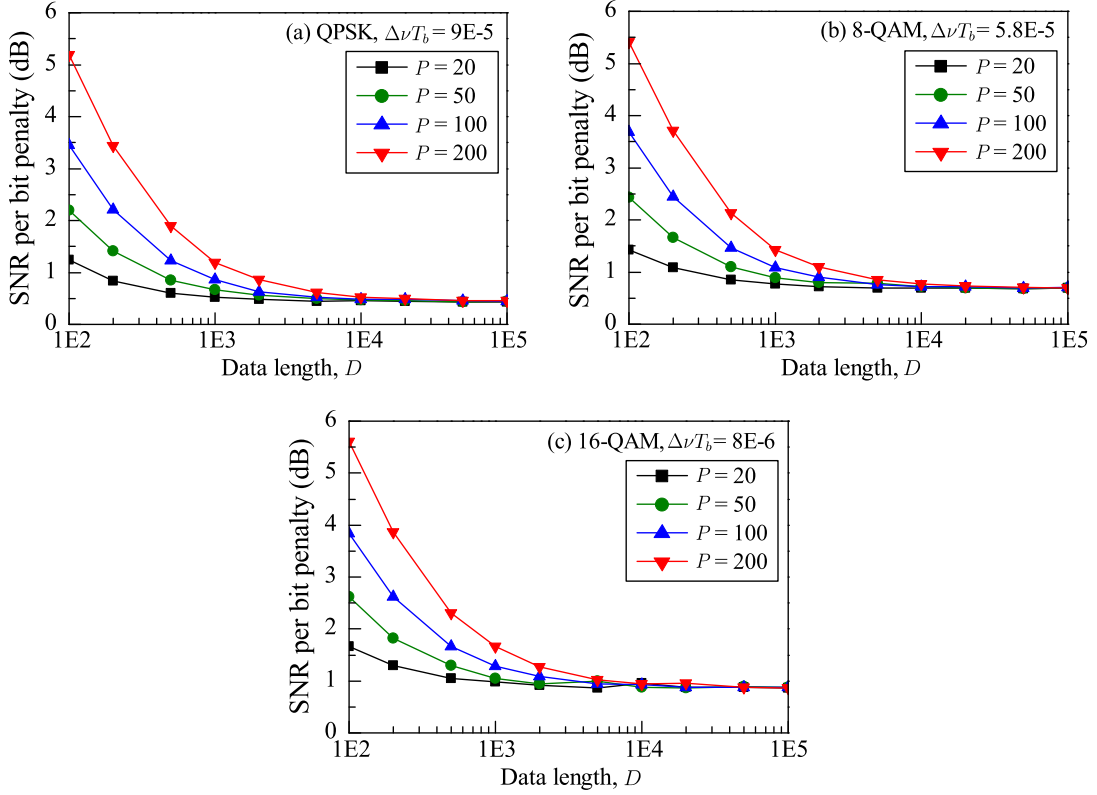


Figure 3.15: SNR per bit penalty versus data length D , at different pilot lengths P , for (a) QPSK, (b) 8-QAM, and (c) 16-QAM. Here, $\Delta f T = 0.1$.

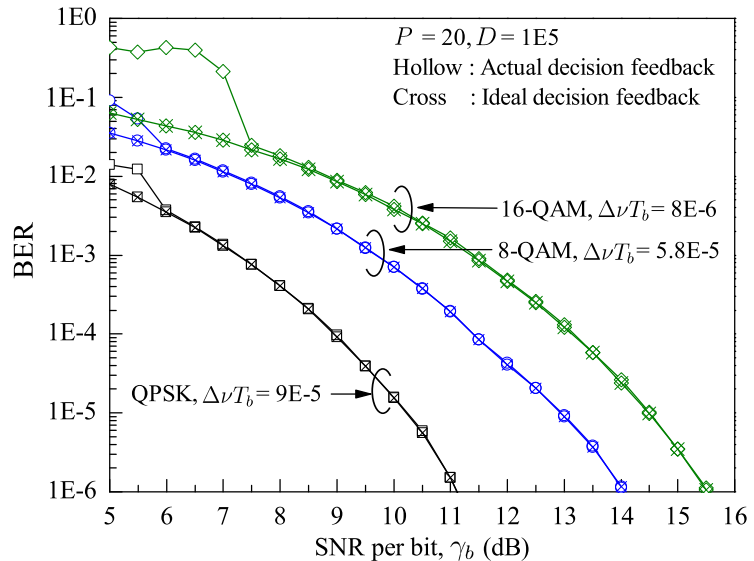


Figure 3.16: BER performance of PA CW-DA-ML with ideal and actual decision feedback. Here, $\Delta f T = 0.1$.

3.4 Time-Varying Frequency Offset

In practice, the frequency of the laser drifts over time in the MHz/s range due to aging or temperature variation and can also experience sudden jumps due to mechanical disturbances or vibrations to the laser cavity [107]. Hence, the frequency offset needs to be continuously tracked for best BER performance in a symbol-by-symbol receiver. Fig. 3.17 evaluates the robustness of PA CW-DA-ML in a time-varying frequency offset environment. A 14-Gbaud 16-QAM signal with $\gamma_b = 12$ dB, $\Delta\nu T_b = 8 \times 10^{-6}$, and training overhead of 0.2% ($D = 10^4$, $P = 20$) was used. The stable BER about 4.7×10^{-4} , measured at 10 ms intervals, demonstrates the reliable tracking of frequency offset experiencing a continuous drift of 10 MHz/s and rapid jumps of 100 kHz every 10 ms. Similarly, we showed in [108] that differentially-encoded CW-DA-ML can track frequency drifts of up to 30 MHz/s and frequency jumps of up to 200 kHz every 10 ms, in a 28-Gbaud 16-QAM signal with $\gamma_b = 13.5$ dB and $\Delta\nu T_b = 4.5 \times 10^{-6}$. CW-DA-ML can continuously track the frequency offset, thanks to its observation dependent filter weight $\hat{\mathbf{w}}(k)$ and negligible error propagation.

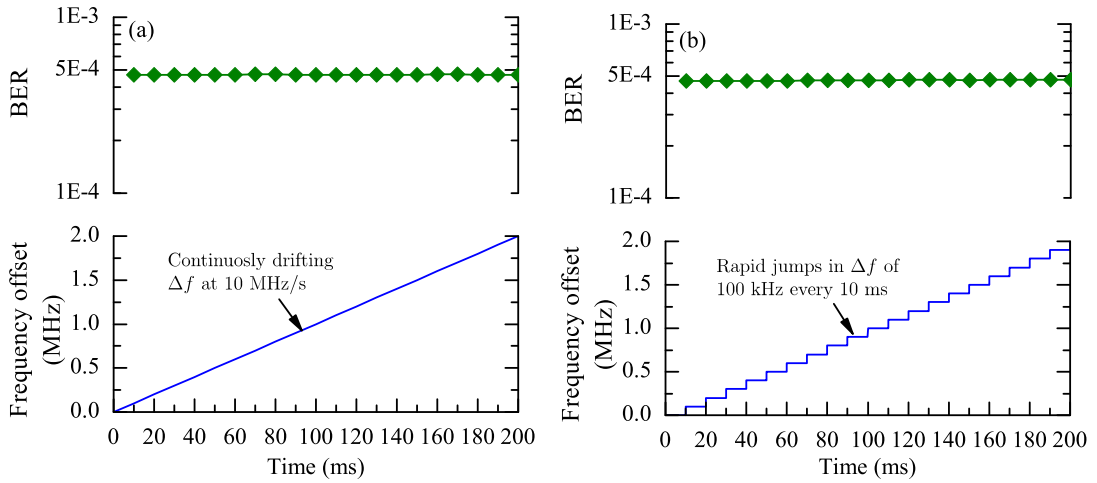


Figure 3.17: BER performance of PA CW-DA-ML in time-varying frequency offset experiencing (a) continuous drift, and (b) rapid jumps.

3.5 ADC Resolution

In coherent receivers, the real and imaginary dimensions of each polarization are sampled and quantized to a discrete set of values by ADCs, whose resolution is determined in number of bits b . In general, ADCs with higher sampling rates are limited to lower resolution [109]. Hence, higher quantization error is introduced in coherent systems requiring higher sampling rates.

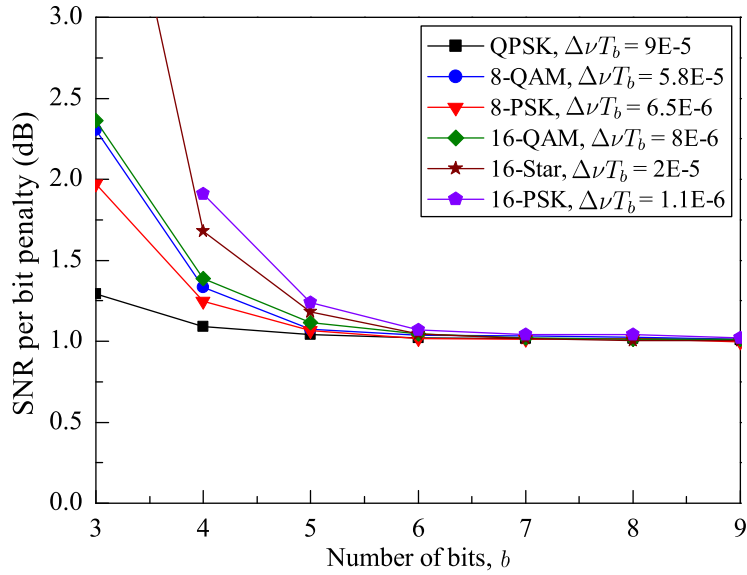


Figure 3.18: ADC resolution in terms of number of bits for differentially-encoded CW-DA-ML. Here, $\Delta fT = 0.1$.

Impact of quantization noise by uniformly quantizing ADC on differentially-encoded CW-DA-ML is investigated in Fig. 3.18, with a time-invariant $\Delta fT = 0.1$. The $\Delta\nu T_b$ is fixed at the tolerance value for a 1-dB γ_b penalty, as listed in Table 3.3. Each signal dimension is divided into 2^b non-overlapping intervals of equal width d_{int} . Midpoint of each interval is designated as the quantization level. Received sample component in each dimension is quantized to the nearest quantization level. The quantization error can be modeled as an additive Gaussian noise with variance $d_{int}^2/12$ per dimension [72].

An ADC resolution greater than 5 bits is seen to be sufficient for all modulation

formats tested. The bits requirement may be reduced by using an ADC with nonuniform quantization intervals, especially for constellations with nonequally spaced signal points such as 8-QAM. Advent of complementary metal-oxide-semiconductor based ADCs with a 6-bit resolution and a sampling rate of 24 Gs/s, commensurate with current line rates, enables the practical implementation of our CW-DA-ML [110].

3.6 Conclusion

Considering the ease of transmitter implementation, differential encoding, tolerance to AWGN, phase noise, frequency offset, and cycle slips, we identify QPSK, 8-QAM, and 16-QAM as the most viable 4-, 8-, and 16-point constellations for coherent optical communications.

Our causal CW-DA-ML achieves a near-ideal frequency offset estimation over a complete ΔfT range of $[-1/2, +1/2]$ and avoids phase unwrapping as it uses a reference phasor with an unambiguous phase tracking range of $[0, 2\pi)$. The initial decay of CW-DA-ML's total-phase-error variance σ_ε^2 follows the Cramer-Rao lower bound (CRLB) [111]¹ closely compared to DiffFE-MPE, reiterating the faster frequency acquisition by CW-DA-ML compared to DiffFE based estimators [108].

Having lower cycle slip probability than MPE based estimators, continuous carrier tracking feature, low training overhead, ability to operate at low SNR region, and being modulation-format independent, makes CW-DA-ML an attractive carrier estimator for flexible multi-modulation coherent receivers with laser frequency instabilities.

¹The CRLB in [111] is derived for joint estimation of a constant phase and frequency offset. Hence, the CRLB of [111] continuously decreases with N .

Chapter 4

Adaptive Complex-Weighted Decision-Aided Phase and Frequency Estimation

Early optical networking systems provided point-to-point WDM transmission. The WDM channels propagated over predetermined optical path between fixed transmitter-receiver pairs, with preset symbol rate and modulation format. These point-to-point systems then evolved into optical mesh topologies using WDM and reconfigurable optical add/drop multiplexers, developed to minimize optical-electrical-optical wavelength regeneration and grooming costs at intermediate nodes [112]. Later, optical packet switching (OPS) offering sub-wavelength switching granularity emerged, driven by the desire for rapidly reconfigurable circuits and effective accommodation of bursty traffic [113]. Unlike early WDM systems, packets can be dynamically routed over different optical paths depending on link status (e.g., link availability and delay), thus experiencing different link impairments. Moreover, with no fixed transmitter-receiver pairs, a given receiver may receive packets from different transmitters. Currently, elastic optical networks [114] and software defined networks [115] have been touted as solutions for enhanced spectral efficiency and optimized network resource utilization. These architectures require transceivers with tunable modulation format and symbol

rate to support trade-offs among optical reach, bit rate, and spectral occupancy [116]. A continuous trade-off between optical reach and spectral efficiency was demonstrated by time-domain interleaving of different MPSK and MQAM signals [117, 118]. Recently, flexible modulation format and bit rate depending on light-path length was shown to reduce queuing delay in OPS networks [119].

Considering the above progress toward a fully reconfigurable optical network, the carrier estimators in intradyne coherent receivers are expected to receive (i) dynamic data with different SNR values and nonlinear phase noise due to variable link impairments, (ii) different laser phase noise and frequency offsets due to variable transmitter-receiver laser pairs, (iii) different modulation formats, and (iv) different symbol rates; and yet be computationally simple for feasible implementation. Popular phase estimators, namely, MPE [89, 92] and BPS [51], utilize fixed-length transversal filters. However, their optimum filter length with respect to BER depends on the parameter set of SNR, linewidth-per-symbol-rate $\Delta\nu T$, nonlinear phase noise, and modulation format [51, 120, 121]. Difficult numerical optimization and manual adjustment of filter length are needed for each set of parameters [51, 120, 121], which is not practical in a reconfigurable optical network. Although the optimum filter length for MPE may be computed using [122]

$$L_{opt,MPE} = \sqrt{3 \frac{\sigma_n^2(1 + 4.5 \times \sigma_n^2)}{\sigma_p^2} - 1}, \quad (4.1)$$

it is only applicable to QPSK format, requires linear laser phase noise and additive noise statistics, does not consider nonlinear phase noise, and still requires manual filter adjustment; all of which are not practical in reconfigurable networks. Besides degrading the BER, a poor choice of filter length directly affects the complexity of the carrier estimator. An unnecessarily long filter length increases the required number of adders and multipliers for filtering. Moreover, given that MPE and DiffFE are not format transparent, several format-adapted MPE modules and format-adapted DiffFE mod-

ules are required to support multiple formats, which increases the receiver hardware.

Previously, a CW-DA-ML estimator with a fixed-length filter was derived in Chapter 3. To avoid the manual filter-length optimization of CW-DA-ML, we develop an adaptive CW-DA estimator with an adaptive filter length in this chapter, following the idea in [123]. Performance of adaptive CW-DA in linear and nonlinear impairments are benchmarked against DiffFE-MPE, DiffFE-BPS, and CW-DA-ML. DiffFE-BPS refers to the operation of DiffFE [87, 88] followed by BPS [51]. In BPS, we set the number of test phases β to 32, following [51]. Finally, a comprehensive complexity analysis of all carrier estimators discussed is presented.

4.1 Principle of Operation

In CW-DA-ML [124], the reference phasor $V(k+1)$ for the carrier at time $k+1$ is computed by Eq. (3.1) using a transversal filter of length L , which can be rewritten as

$$V(k+1) = C(k) \sum_{i=1}^L w_i(k) r(k-i+1) \hat{m}^*(k-i+1) \quad (4.2)$$

where $w_i(k)$ is the i th complex scalar filter weight.

To avoid specifying a filter length L , we propose to replace Eq. (4.2) with a new complex reference phasor $\bar{V}(k+1)$ formed by a first-order recursion as

$$\bar{V}(k+1) = w_1 \bar{V}(k) + w_2 \frac{r(k)}{\hat{m}(k)}, \quad k \geq 0. \quad (4.3)$$

The new phasor $\bar{V}(k+1)$ for demodulating the $(k+1)$ th symbol is a complex-weighted sum of the previous phasor $\bar{V}(k)$ and the current filter input $r(k)/\hat{m}(k)$. No normalization factor is required as the filter input $r(k)/\hat{m}(k)$ is normalized, unlike the need of a normalization factor $C(k)$ in Eq. (3.1) for CW-DA-ML. Our new adaptive CW-DA estimator is applicable to both MPSK and MQAM signals due to the decision-aided approach of Eq. (4.3). Let $x(k) = r(k)/\hat{m}(k)$. If $\hat{m}(k) = m(k)$, then $x(k)$ approximates

4.1 Principle of Operation

the carrier at time k . Using $x(k)$ as the desired response, we define the estimation error as the difference between $x(k)$ and $\bar{V}(k)$. At time $k = 0$, we initialize $\bar{V}(0) = 1$, $w_1 = 0$, and $w_2 = 1$, to give the maximum gain of one to the first received signal $r(0)/\hat{m}(0)$. Subsequently, filter weights in Eq. (4.3) are recomputed automatically at each time $k \geq 1$ based on the observations $\{r(l), 0 \leq l \leq k\}$ so as to minimize the sum-of-error-squares cost function $J(k)$, where

$$J(k) = \sum_{l=1}^k |x(l) - \bar{V}(l)|^2. \quad (4.4)$$

In Eq. (4.4), $\bar{V}(l)$ is expressed in terms of Eq. (4.3). Solving $\partial J(k)/\partial \mathbf{w}^* = 0$, where $\mathbf{w} = [w_1, w_2]^T$, yields the least-squares optimum weight vector $\hat{\mathbf{w}}$ at time k as

$$\hat{\mathbf{w}} = \Phi^{-1} \mathbf{z} \quad (4.5)$$

$$\Phi = \sum_{l=1}^k \begin{bmatrix} |\bar{V}(l-1)|^2 & \bar{V}^*(l-1)x(l-1) \\ x^*(l-1)\bar{V}(l-1) & |x(l-1)|^2 \end{bmatrix} \quad (4.6)$$

$$\mathbf{z} = \sum_{l=1}^k x(l) \begin{bmatrix} \bar{V}^*(l-1) \\ x^*(l-1) \end{bmatrix} \quad (4.7)$$

where Φ is a 2-by-2 matrix and \mathbf{z} is a 2-by-1 vector. The detailed derivation of $\hat{\mathbf{w}}$ is given in Appendix D. The structure of adaptive CW-DA estimator is shown in Fig. 4.1.

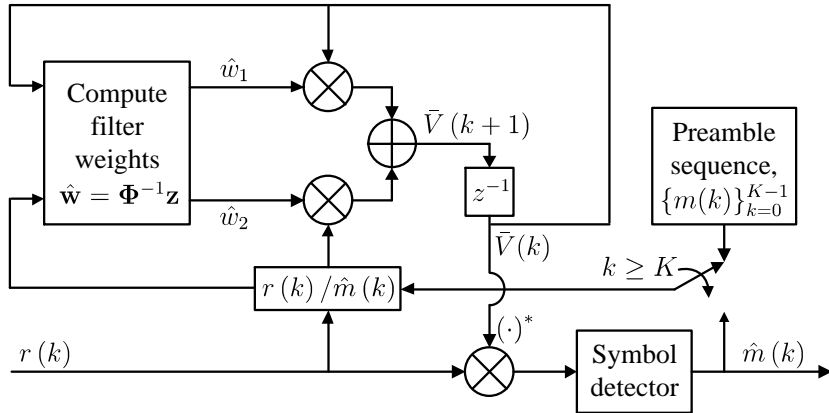


Figure 4.1: Adaptive CW-DA estimator.

4.2 Adaptation of Effective Filter Length

An initial preamble of K known symbols $\{m(k)\}_{k=0}^{K-1}$ is used to aid in acquiring the steady-state filter weights and tracking of the phasor $e^{j(\theta(k)+\Delta\omega k)}$. Thereafter, the adaptive CW-DA estimator switches to using the actual symbol decisions, $\{\hat{m}(k)\}_{k \geq K}$.

4.2 Adaptation of Effective Filter Length

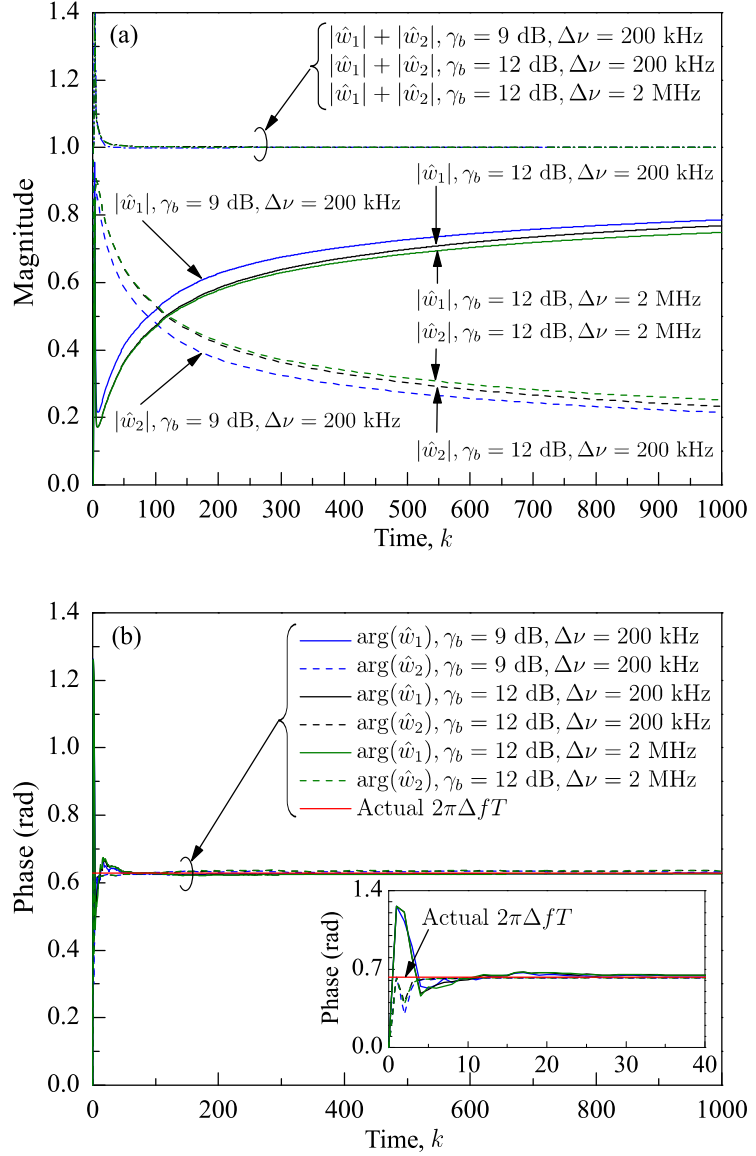


Figure 4.2: Adaptation of the (a) magnitude of weights, $|\hat{w}_i|$, and (b) phase of weights, $\arg(\hat{w}_i)$. Inset shows enlarged time $0 \leq k \leq 40$.

Fig. 4.2 plots the automatic filter weight adaptation of adaptive CW-DA estimator

4.2 Adaptation of Effective Filter Length

at different values of SNR and laser linewidth, averaged over 500 runs, for 28-Gbaud 16-QAM signals. Simulation runs in Fig. 4.2(a) show the gain $|\hat{w}_1|$ on the filter input $\bar{V}(k)$ increasing from 0 while the gain $|\hat{w}_2|$ on $r(k)/\hat{m}(k)$ decreases from 1, to a steady-state value between 0 and 1 as k increases. The large initial gain $|\hat{w}_2|$ helps in carrier acquisition, while the smaller steady-state gain $|\hat{w}_2|$ is suitable for tracking the carrier.

Magnitude of $\bar{V}(l)$ must approximate 1 to minimize the sum of error squares in Eq. (4.4) since the magnitude of $x(l)$ is ~ 1 . For this condition to be satisfied, the magnitude sum of the filter weights must equal 1 by virtue of Eq. (4.3). Indeed, the steady-state $|\hat{w}_1| + |\hat{w}_2|$ always equal to ~ 1 in Fig. 4.2(a). Given the recursive nature of Eq. (4.3) and the sum $|\hat{w}_1| + |\hat{w}_2| \cong 1$, the filter input samples $x(l)$ will be summed in a decaying manner by Eq. (4.3). Thus, $|\hat{w}_1|$ is a measure of the effective filter length of our recursive filter. From Fig. 4.2(a), we see that the effective filter length represented by $|\hat{w}_1|$ decreases with the SNR and laser linewidth. As SNR goes to infinity, the steady-state $|\hat{w}_1|$ goes to zero, and the receiver employing the adaptive CW-DA algorithm approaches a differential detector.

The phasor $\bar{V}(l)$ must have an angular frequency offset approximating $\Delta\omega l$ to minimize Eq. (4.4) since angular frequency offset of $x(l)$ is $\sim \Delta\omega l$. For this condition to be satisfied, the phase of \hat{w}_1 and \hat{w}_2 should be $\sim 2\pi\Delta f T$ by virtue of Eq. (4.3). Indeed, the phase of \hat{w}_1 and \hat{w}_2 always converge to the actual $2\pi\Delta f T$ value of 0.2π rad in Fig. 4.2(b) regardless of SNR and $\Delta\nu T$. Results of Fig. 4.2 show that the magnitude of the filter weights control the effective sample averaging length depending on SNR and $\Delta\nu T$, while the phase of the filter weights help track the angular frequency offset of the carrier.

Fig. 4.3 shows the BER performance of CW-DA-ML for QPSK and 16-QAM signals. The value $(LT)^{-1}$ is a measure of an estimator's bandwidth. The optimum value of L found by an exhaustive search is larger at low SNR and smaller at high SNR. Narrower bandwidth is beneficial at lower SNR to filter the dominant ASE noise and

4.3 Performance in Presence of Linear Phase Noise

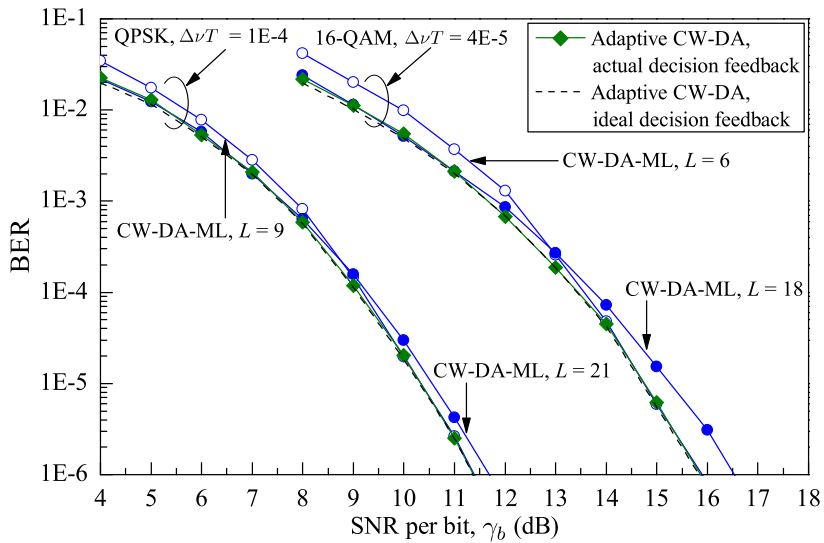


Figure 4.3: BER performance of adaptive CW-DA estimator. Here, $\Delta fT = 0.1$

wider bandwidth is beneficial at higher SNR to track the dominant laser phase noise. On the flip side, adaptive CW-DA estimator always minimizes the BER by automatically adapting its effective filter length according to the SNR, $\Delta\nu T$, and modulation format. Performance loss of actual, compared to ideal, decision feedback is minimal for the tested SNR range.

The adaptive CW-DA estimator not only inherits the merits of CW-DA-ML (e.g., no phase unwrapping, modulation-format independent), but also requires no preset parameters such as filter length L , since the knowledge of phase noise and additive noise is learned adaptively based on the observed signal. These characteristics render the adaptive CW-DA estimator practically useful in a realistic, unknown environment.

4.3 Performance in Presence of Linear Phase Noise

The $\Delta\nu T$ tolerance, ΔfT tolerance, and cycle slip probability in linear phase noise are investigated via simulation. Furthermore, filter-length optimization is shown to be crucial as it affects the cycle slip probability besides the BER performance.

4.3.1 Laser Linewidth and Frequency Offset Tolerance

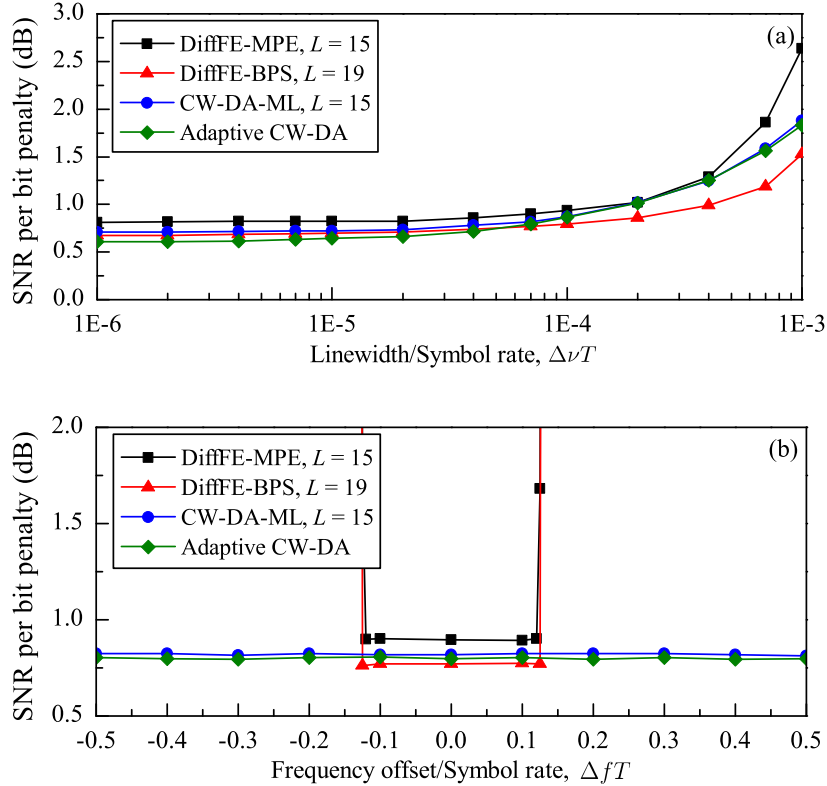


Figure 4.4: (a) Laser linewidth tolerance, with $\Delta f T = 0.1$. (b) Frequency offset tolerance, with $\Delta\nu T = 7 \times 10^{-5}$.

Fig. 4.4 compares the laser linewidth and frequency offset tolerance of carrier estimators at a BER of 10^{-3} for QPSK signals. The γ_b penalty is referenced to that of ideal coherent detection. The filter length L in MPE, BPS, and CW-DA-ML is set to 15, 19, and 15, respectively, which are numerically optimized for a 1-dB γ_b penalty at BER of 10^{-3} [124]. For a 1-dB penalty, adaptive CW-DA estimator accommodates a $\Delta\nu T$ of 1.8×10^{-4} which is comparable to that of MPE and CW-DA-ML, but slightly smaller than the tolerance of BPS. As for the $\Delta f T$ estimation range, DiffFE is limited to $\pm 1/8$ for the reasons established earlier in Section 3.2.2. However, adaptive CW-DA estimator attains a complete $\Delta f T$ estimation range of $\pm 1/2$, as the phasor $\bar{V}(k)$ has an unambiguous phase tracking range of $[0, 2\pi)$.

4.3.2 Cycle Slip Probability

For an error-free optical communication, the optical reach without regeneration is limited by SNR. FEC is now widely adopted as a standard technique for increasing the optical reach or lowering the SNR requirement [125]. In general, FEC codes are not designed for burst errors and correlated errors, which if encountered can tighten the BER threshold of the code [126].

Cycle slips are inherent in MPE, BPS, CW-DA-ML, and adaptive CW-DA estimator. Pilot symbols can be used to mitigate cycle slips, but errors due to cycle slips will persist until the next pilot symbols arrive resulting in burst errors. For successful FEC decoding, pilot symbols need to be inserted at a much higher frequency than the cycle slip probability to minimize the burst error length. Therefore, a low cycle slip probability is preferred to minimize the pilot overhead.

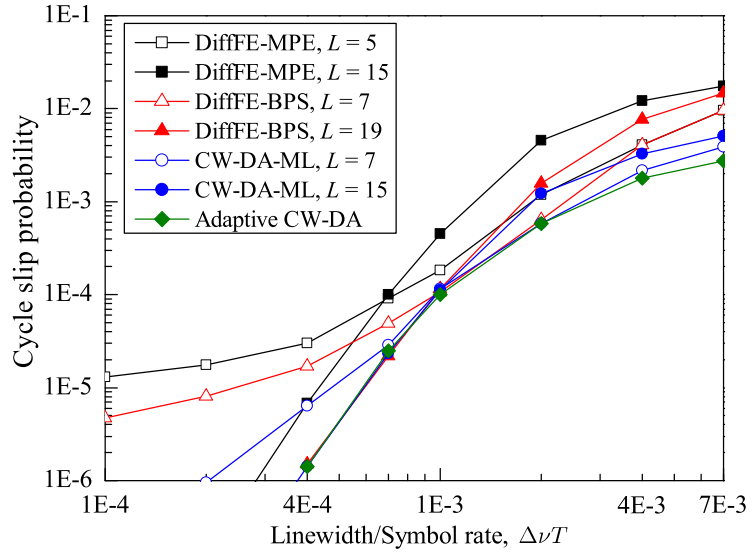


Figure 4.5: Cycle slip probability versus $\Delta\nu T$ for different filter lengths.

The cycle slip probability is plotted in Fig. 4.5 using QPSK signals at $\gamma_b = 7.82$ dB. Cycle slip probability is seen to be filter-length dependent in DiffFE-MPE, DiffFE-BPS, and CW-DA-ML. Effective tracking of laser phase noise using shorter filter lengths at broader laser linewidths and sufficient averaging of ASE noise at narrower

laser linewidths using longer filter lengths, improves the phase estimate. Improved phase estimate reduces the cycle slip probability by reducing phase unwrapping errors in MPE and BPS, and by reducing the symbol decision errors in CW-DA-ML. Inappropriate selection of filter length can be detrimental. For example, insufficient filter length causes a cycle slip probability floor at smaller values of $\Delta\nu T$ in Fig. 4.5. Our adaptive CW-DA estimator tolerates a larger or equal $\Delta\nu T$ compared to DiffFE-MPE, DiffFE-BPS, and CW-DA-ML for a given cycle slip probability.

Next, we demonstrate the criticality of filter-length optimization in a differentially encoded system employing SD FEC. Here, differential encoding is intended to arrest cycle slips. SD FEC provides enhanced net coding gain but its benefits are impaired by the error duplication penalty in differentially encoded systems [127]. The differential encoding penalty was shown to be completely eliminated by turbo differential decoding (TDD), i.e., turbo decoding of an outer SD low density parity check decoder and an inner soft differential decoder [127, 128]. However, TDD is vulnerable to a quickly rising post-FEC error floor in the presence of frequent cycle slips [128].

Fig. 4.6 plots the required SNR for QPSK signals with a target BER of $2.5 \times$

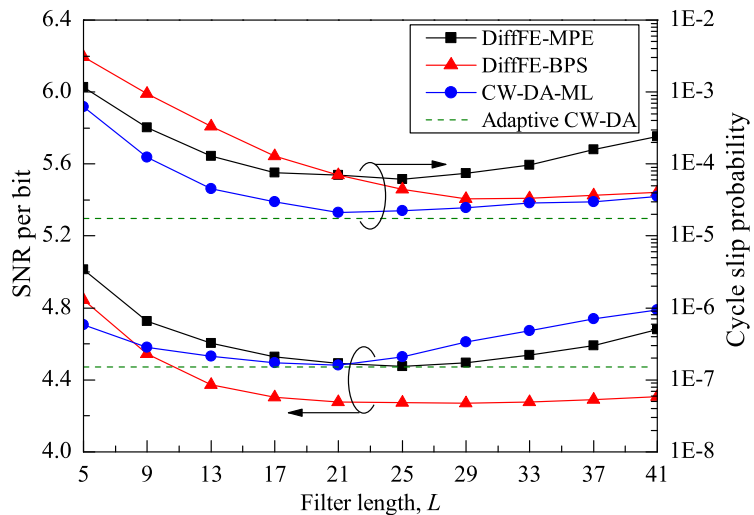


Figure 4.6: Required SNR and corresponding cycle slip probability at $\text{BER} = 2.5 \times 10^{-2}$. Here, $\Delta\nu T = 3 \times 10^{-4}$.

10^{-2} and the corresponding cycle slip probability as a function of the filter length. The cycle slip probability is more sensitive than the required SNR to variations in the filter length. For example, DiffFE-BPS attains a 0.58-dB improvement in the required SNR with filter-length optimization but achieves a 94 times reduction in cycle slip probability. Misadjustment of filter length L in DiffFE-MPE by 4 taps from 17 to 13 causes the cycle slip probability to rise above 10^{-4} , which would cause the TDD post-FEC BER to saturate above 10^{-9} [128]. Such misadjustments can render the carrier estimator unusable as high data integrity with BER lower than 10^{-9} , preferably 10^{-12} , is generally expected in optical transport systems. On the other hand, adaptive CW-DA estimator assures the lowest cycle slip probability at 1.8×10^{-5} and a TDD post-FEC BER of much lower than 10^{-9} . Simultaneously, our new estimator achieves a comparable SNR requirement to that of DiffFE-MPE and CW-DA-ML, and is a mere 0.2 dB inferior to DiffFE-BPS with optimum filter length.

4.4 Performance in Presence of Nonlinear Phase Noise

A key difference between optical fiber and other transmission media is the presence of nonlinear effects. The dominant nonlinear impairment in fiber is the Kerr nonlinearity, where the refractive index of silica fiber vary with the signal power. Interaction of signal and ASE noise with the Kerr effect generates self-phase-modulation (SPM) induced nonlinear phase noise [129].

Assuming the use of zero-dispersion fiber spans, the accumulated nonlinear phase noise experienced by the signal after N_A EDFA is given by [130]

$$\theta_{NL}(k) = \gamma L_{eff} \cdot \sum_{j=1}^{N_A} \left| \sqrt{P_t(k)} e^{j\phi(k)} + \sum_{i=1}^j n_{ASE,i}(k) \right|^2 \quad (4.8)$$

where γ is the nonlinear coupling coefficient and the quantity

$$L_{eff} = \left(\frac{1 - \exp(-\alpha L_f)}{\alpha} \right) \quad (4.9)$$

is the effective interaction length of the fiber [54]. Hence, the input sample to the carrier estimator now becomes

$$\begin{aligned} r(k) &= [m(k)e^{j(\theta_L(k)+\Delta\omega k)} + n(k)]e^{j\theta_{NL}(k)} \\ &= m(k)e^{j(\theta(k)+\Delta\omega k)} + n(k)e^{j\theta_{NL}(k)} \end{aligned} \quad (4.10)$$

where the total phase noise impairment is $\theta(k) = \theta_L(k) + \theta_{NL}(k)$.

Nonlinear phase noise impairs the performance of phase-modulated optical systems [131]. SPM effect is more pronounced in the initial length of L_{eff} , compared to the latter part, in a span due to the higher initial signal power [132]. Attenuation of signal power along the fiber offsets the SPM effect after the initial length of L_{eff} .

We consider the presence of fiber Kerr nonlinearity in the optical transmission system illustrated in Fig. 2.3. A nominal combined laser linewidth of 200 kHz is used and the system parameters in Table 4.1 are assumed.

Table 4.1: System parameter values used in evaluating the nonlinear phase noise and cycle slip tolerance

Parameter	Value	Parameter	Value	Parameter	Value
γ	$1.2 \text{ W}^{-1}\text{km}^{-1}$	α	0.2 dB/km	L_f	100 km
G	20 dB	λ	1550 nm	n_{sp}	1.41
B_o	28 GHz				

4.4.1 BER Performance

Fig. 4.7 analyzes the nonlinear phase noise tolerance of carrier estimators in a 28-Gbaud QPSK signal transmission over $N_A = 41$ spans. The launch power in dBm of Fig. 4.7 is computed as $10 \log_{10}(P_t/1\text{mW})$. The optimum filter length for DiffFE-MPE, DiffFE-BPS, and CW-DA-ML was found to be 21, 27, and 21, respectively,

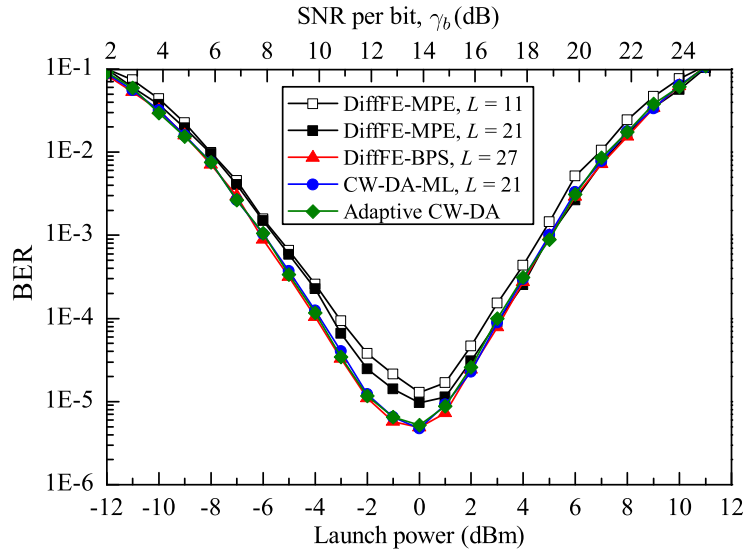


Figure 4.7: BER performance of carrier estimators in nonlinear phase noise. Here, $\Delta f T = 0.1$.

through an exhaustive search. In contrast, our new estimator automatically adapts its effective filter length according to the nonlinear phase noise to achieve the lower BER. The minimum BER occurs at approximately 0 dBm launch power corresponding to a mean nonlinear phase shift $\mathbb{E}[\theta_{NL}]$ of 1.07 rad, which can be computed using [130]

$$\mathbb{E}[\theta_{NL}] = N_A \gamma L_{eff} \left[\left| \sqrt{P_t(k)} e^{j\phi(k)} \right|^2 + (N_A + 1) \frac{\sigma_{ASE}^2}{2} \right]. \quad (4.11)$$

Our result agrees well with the finding of [129] which shows the error rate of a phase-modulated system to be minimized when the mean nonlinear phase shift $\mathbb{E}[\phi_{NL}]$ is in the neighborhood of 1 rad. As the launch power exceeds the optimum power, variance of the total phase noise increases and the BER deteriorates. Adaptive CW-DA estimator approximately halves the minimum achievable BER compared to DiffFE-MPE.

4.4.2 Cycle Slip Probability

In order to understand the effect of nonlinear phase noise on cycle slip probability, we kept the SNR per bit constant at 4.47 dB in Fig. 4.7 and varied the launch power. The

resulting cycle slip probability is plotted in Fig. 4.8. The value of n_{sp} was varied to keep the SNR constant. The nonlinear phase shift increases with the launch power, thereby increasing the cycle slip probability. A cycle slip probability floor appears for DiffFE-MPE and DiffFE-BPS employing fixed-length filters, similar to the linear phase noise case in Fig. 4.5. Points yielding a BER of 2.5×10^{-2} with differential encoding are marked in Fig. 4.8 and tabulated in Table 4.2.

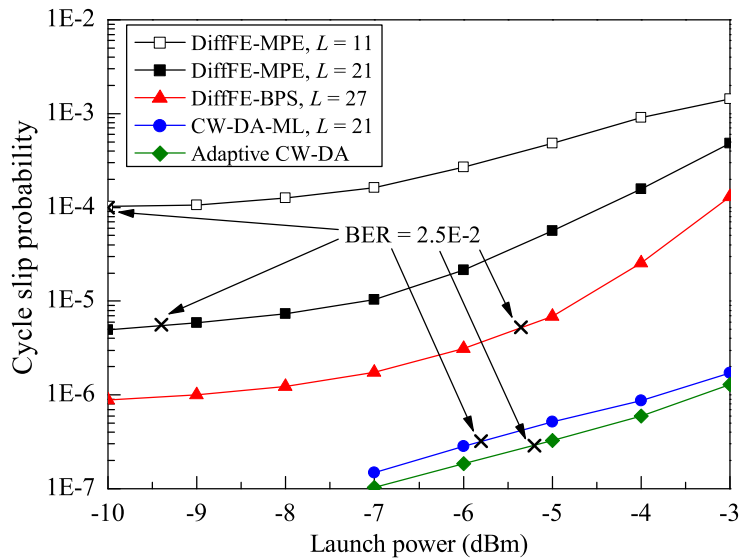


Figure 4.8: Cycle slip probability of carrier estimators in nonlinear phase noise.

Table 4.2: Coordinates of points at $\text{BER} = 2.5 \times 10^{-2}$ in Fig. 4.8

Carrier estimator	Launch power (dBm)	Cycle slip probability
DiffFE-MPE, $L = 11$	-10.0	1.0×10^{-4}
DiffFE-MPE, $L = 21$	-9.4	5.6×10^{-6}
DiffFE-BPS, $L = 27$	-5.4	5.3×10^{-6}
CW-DA-ML, $L = 21$	-5.8	3.2×10^{-7}
Adaptive CW-DA	-5.2	2.9×10^{-7}

The importance of filter-length adjustment is illustrated by DiffFE-MPE using $L = 11$ and $L = 21$. Filter-length adjustment from 11 to 21 yields a minimal 0.6-dB improvement in launch power tolerance at a BER of 2.5×10^{-2} , but successfully avoids

a TDD post-FEC error floor of 10^{-9} by reducing the cycle slip probability from 10^{-4} to 5.6×10^{-6} . From Table 4.2, we observe that the adaptive CW-DA estimator achieves greater nonlinear phase noise tolerance and lower cycle slip probability than the other estimators.

4.5 Complexity Analysis

An important issue that influences the choice of an estimation algorithm is its computational complexity. Carrier estimators should have a low computational complexity in order to be feasible for practical implementation with data rates of 100 Gb/s and beyond. In this section we assess the computational load associated with frequency and phase estimation algorithms described so far.

The computational complexity of CW-DA-ML and adaptive CW-DA estimator to compute the reference phasor $V(k)$ and $\bar{V}(k)$, respectively, is analyzed in Table 4.3. The complexity of FFTFE and DiffFE to estimate $\Delta\omega$ using an observation of N symbols, and the complexity of MPE and BPS to estimate $\theta(k)$ per symbol, are also provided in Table 4.3 for comparison. Assuming an equiprobable symbol distribution, the Class I symbol probability of $1/2$ is used in computing the complexity of DiffFE and MPE, for 16-QAM signals. A complex multiplication corresponds to four real multiplications and two real additions, each modulus extraction requires two real multiplications and one real addition, and searching for the maximum in a set $\{|a(k)|\}_{k=0}^{N-1}$ where $a(k)$ is a complex scalar requires N comparisons. Each $\arg(a(k))$ is expressed as one access to a read-only memory (ROM) to map $a(k)$ into $\arg(a(k))$, and each phase unwrapping operation is expressed as one phase unwrap operation. Each buffer unit is defined to hold one real value.

The radix-2 FFT in FFTFE requires an undesirably large $(N/2) \log_2 N$ complex multiplications and $N \log_2 N$ complex additions, whereas the peak search involves

Table 4.3: Complexity comparison of carrier estimators

Estimator	Complexity to estimate	Format	Real multiplications	Real additions	Intermediate decisions	Comp-arisons	ROM access	Phase unwrap	Buffer units
FFTFE ^a	$\Delta\omega$ over N symbols	MPSK	$2N \log_2 N + 4N \log_2 M + 2N + 2$	$3N \log_2 N + 2N \log_2 M + N$	0	N	0	0	$2N$
		16-QAM	$2N \log_2 N + 10N + 2$	$3N \log_2 N + 5N$	0	N	0	0	$2N$
DiffFE	$\Delta\omega$ over N symbols	MPSK	$(1 + \log_2 M) \times 4(N - 1) + 1$	$(1 + \log_2 M) \times 2(N - 1) + 2N - 2$	0	0	1	0	0
		16-QAM	$7N + 1$	$4N - 2$	0	2	1	0	0
MPE	$\theta(k)$ per symbol	MPSK	$4 \log_2 M + 1/L$	$2 \log_2 M + 2 - 2/L$	0	0	$1/L$	$1/L$	0
		16-QAM	$24 + 5/L$	$17 - 2/L$	0	$(L+4) \times (1/2L)$	$1/L$	$1/L$	0
BPS	$\theta(k)$ per symbol	MPSK / MQAM	6β	$(L+4)\beta$	β	β	0	1	$L\beta$
CW-DA-ML	$V(k)$ per symbol	MPSK / MQAM	$6L^2 + 14L + 10$	$6L^2 + 8L + 6$	0	0	0	0	$L^2 + 6L + 4$
Adaptive CW-DA	$\bar{V}(k)$ per symbol	MPSK / MQAM	43	34	0	0	0	0	12

^a A radix-2 FFT is assumed.

N modulus extractions and N comparisons. The complexity of FFTFE adds to the processing bottleneck described in Section 3.2.4 which is incurred every time the frequency is re-estimated. The complexity of FFTFE, DiffFE, MPE, and BPS are modulation-format dependent, since raising samples to the q th power and the required number of test phase angles β , are modulation-format dependent [51].

In general, compared to the other estimators, CW-DA-ML has increased number of multiplications and additions but avoids any intermediate decisions, comparisons, ROM accesses, and phase unwrapping operations. The increase in number of multiplications and additions is traded-off with its fast, wide, and continuous frequency tracking features. Using some representative parameter values, we see that CW-DA-ML ($L = 12$, buffer units = 220) achieves more than 2.7 times reduction in buffer units compared to FFTFE ($N = 360$, buffer units = 720) and BPS ($L = 19$, $\beta = 32$, buffer units = 608) in 16-QAM.

Besides inheriting the advantages of CW-DA-ML such as no intermediate decisions, comparisons, ROM accesses, and phase unwrapping, adaptive CW-DA estimator achieves dramatic reduction in number of multiplications, additions and buffer units, thanks to its two-tap filter structure. We compute and store only the upper triangle of the matrix Φ in Eq. (4.6) while the lower triangle is obtained by diagonal reflection, as Φ is Hermitian. Summations in Eq. (4.6) and Eq. (4.7) can be computed recursively, since they can be written as

$$\Phi(k) = \Phi(k-1) + \begin{bmatrix} |\bar{V}(k-1)|^2 & \bar{V}^*(k-1)x(k-1) \\ x^*(k-1)\bar{V}(k-1) & |x(k-1)|^2 \end{bmatrix} \quad (4.12)$$

and

$$\mathbf{z}(k) = \mathbf{z}(k-1) + \begin{bmatrix} \bar{V}^*(k-1) \\ x^*(k-1) \end{bmatrix}, \quad (4.13)$$

respectively. Furthermore, the matrix inversion in Eq. (4.5) is trivial as Φ is a 2-by-2

matrix. Adaptive CW-DA estimator has a fixed format-transparent complexity, unlike FFTFE, DiffFE, MPE, BPS, and CW-DA-ML whose complexity varies with M , L , and β . Representative computational-load numbers, obtained using practical parameter values, are given in Table 4.4. Adaptive CW-DA estimator reduces the multiplications, additions, and buffer units by a factor of 36.5, 43.4, and 26.6, respectively, compared to CW-DA-ML for QPSK signals. Although BPS only estimates the phase, it still needs 4.5, 21.6, and 50.7 times more multiplications, additions, and buffer units, respectively, compared to adaptive CW-DA estimator.

Further reduction of adaptive CW-DA estimator's complexity can be achieved in an application specific integrated circuit (ASIC) implementation, for example, by using the coordinate rotation digital computing technique [99]. We remark that the required digital resolution of the ASIC, in terms of number of bits, to minimize the signal quantization penalty will affect the implementation complexity.

4.6 Conclusion

A judicious choice of filter length is crucial in carrier estimators using fixed-length filters such as MPE, BPS, and CW-DA-ML, regardless of their deployment in a PA or a differentially encoded system. Although the degradation in the required SNR or nonlinear phase noise tolerance is minimal when the filter length is not optimized, the resulting degradation in cycle slip probability can cause system failures.

We presented a low-complexity adaptive CW-DA estimator which automatically adapts its effective filter length according to the SNR, $\Delta\nu T$, nonlinear phase noise, and modulation format. It is noteworthy that no preset parameters are required. The adaptive CW-DA estimator has similar $\Delta\nu T$ tolerance as MPE and CW-DA-ML, but slightly less compared to BPS. However, the γ_b penalty compared to BPS is a mere 0.25 dB at $\Delta\nu T = 4.1 \times 10^{-4}$. Our new estimator achieves a lower or equal cycle slip

Table 4.4: Complexity of carrier estimators using representative parameter values

Estimator	Complexity to estimate	Format	Values	Real multiplications	Real additions	Intermediate decisions	Comparisons	ROM access	Phase unwrap	Buffer units
DiffFE	$\Delta\omega$ over N symbols	QPSK	$N = 10^4$	119989	79992	0	0	1	0	0
		16-QAM	$N = 42 \times 10^3$	294001	167998	0	2	1	0	0
MPE	$\theta(k)$ per symbol	QPSK	$L = 15$	8.07	5.87	0	0	0.07	0.07	0
		16-QAM	$L = 24$	24.21	16.92	0	0.58	0.04	0.04	0
BPS	$\theta(k)$ per symbol	MPSK / MQAM	$L = 19$ $\beta = 32$	192	736	32	32	0	1	608
		QPSK	$L = 15$	1570	1476	0	0	0	0	319
CW-DA-ML	$V(k)$ per symbol	16-QAM	$L = 12$	1042	966	0	0	0	0	220
		MPSK / MQAM	-	43	34	0	0	0	0	12
Adaptive CW-DA	$\bar{V}(k)$ per symbol									

4.6 Conclusion

probability compared to DiffFE-MPE, DiffFE-BPS, and CW-DA-ML, in linear and nonlinear phase noise systems. Additionally, a larger nonlinear phase noise tolerance than the other estimators and a complete frequency estimation range is achieved.

Chapter 5

Intensity-Modulated Direct-Detection Radio-over-Fiber System

In this chapter, we consider an IMDD RoF uplink with a loopback architecture employing RSOA-equipped RBSs for broadband wireless access network application. To circumvent the bandwidth limitation of RSOA, RoF systems conventionally utilized frequency downconversion of wireless signals to baseband before being fed to the RSOA [41]. This requires additional signal processing circuitry at RBSs which increases the cost and complexity, and defeats the attractiveness of RoF. Use of optical envelope detection by RSOA was proposed in [42] to avoid the frequency downconversion of RF signals at RBSs. However, [42] is applicable only to wireless signals with amplitude modulation format when the RF carrier frequency is larger than the modulation bandwidth of RSOA. This technique deprives the advantages of advanced modulation formats such as QPSK.

The smooth roll-off characteristics of RSOA's frequency response was exploited in [133] to suggest the use of postdetection electronic equalization at the receiver, to compensate for the limited modulation bandwidth of RSOA. In addition to equalization, FEC codes has been proposed to extend the reach of an RSOA-based system to 20 km [134]. Implementation of equalizers and FEC codes will add to the receiver com-

5.1 Experimental Setup

plexity and overhead, respectively. In these techniques, the data rate will be limited, or parallel processing will be necessitated, by the available electronic computation speed.

Suppressing one of the sidebands in a DSB modulated signal, is known to resolve the signal fading problem in transmission over dispersive fibers [135]. Optical single sideband (SSB) transmitters implemented using dual-electrode MZMs or electroabsorption modulated lasers have been proposed [135, 136]. However, these methods require more complex transmitter designs and laser diode placement at the RBSs which is undesirable.

We propose a novel optical receiver design incorporating a simple DI before photodetection at the CO, for an IMDD RoF system. A 40-km upstream transmission of a 2-Gb/s BPSK signal at 6-GHz RF band over a SSMF using a directly modulated RSOA in a single-fiber loopback network is experimentally demonstrated to assess the effectiveness of our new receiver. The role of DI in equalizing the band-limitation of the RSOA and in increasing the transmission reach by improving tolerance against CD is elucidated. Additionally, we show how DI simultaneously helps generate optical SSB signals in order to be robust against signal fading. Impact of backscattered light on the RF band signal in a single-fiber loopback system and its effects on the achievable transmission distance is analyzed. No frequency downconversion of RF signal at the RBS, postdetection electrical passband equalization at the CO, or use of FEC codes is required in our proposed receiver design.

5.1 Experimental Setup

Experimental setup is depicted in Fig. 5.1. A CW laser operating at 1550.14 nm was first launched into SSMF through an optical circulator and then fed to an RSOA. The RSOA used in the experiment is housed in a transistor-outlook (TO)-can package and is an uncooled device. Its measured frequency response, when a laser light of -5

5.1 Experimental Setup

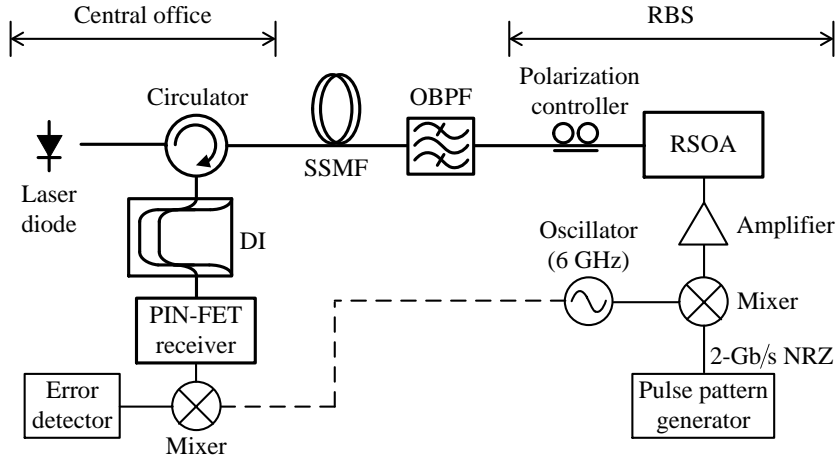


Figure 5.1: Experimental setup for upstream transmission of BPSK radio signals.

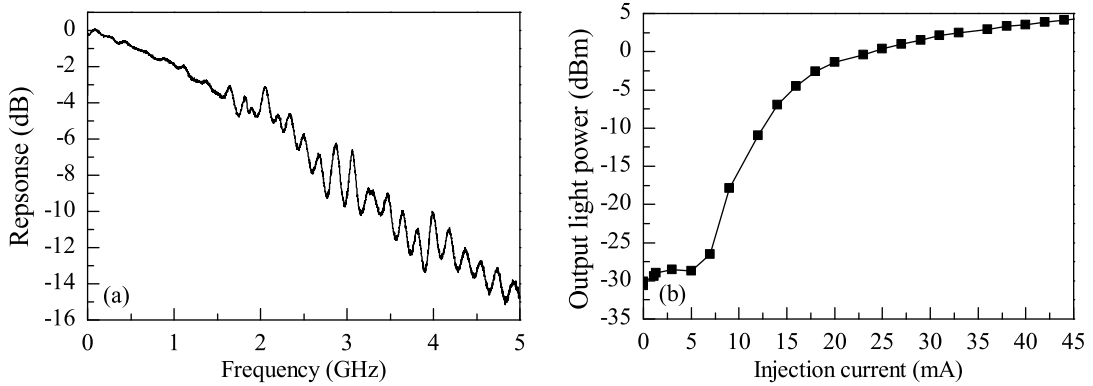


Figure 5.2: RSOA's measured (a) frequency response, and (b) L/I characteristic.

dBm is incident, is shown in Fig. 5.2(a). The device exhibits a 3-dB bandwidth of 1.4 GHz and a roll-off of ~ 3.4 dB/GHz. The polarization-dependent gain of the RSOA was measured to be 2.5 dB and thus a polarization controller was inserted before the RSOA. In real systems, use of polarization-insensitive RSOAs can eliminate the polarization controller. A 2-Gb/s NRZ signal, having a pseudorandom bit pattern of length $2^{31} - 1$, is mixed with a 6 GHz RF carrier producing a BPSK signal which is used to directly modulate the RSOA through a bias-T. The RSOA's nonlinear light-versus-current (L/I) curve is depicted in Fig. 5.2(b) for an injected laser light power of -10 dBm. The dc bias current of the RSOA was set to 41 mA, in the linear region of the L/I transfer function.

The intensity modulated optical signal was transmitted uplink through the SSMF, fed through a DI, and directly detected by a PIN field-effect transistor (FET) receiver at the CO. Free-spectral range (i.e., periodicity) of the DI used is 25 GHz. In the transmission link, we have an optical band-pass filter (OBPF) with a bandwidth of 1.5 nm to emulate a waveguide grating router (WGR) at the remote node of a WDM passive optical network system. The WGR also filters out the out-of-band ASE noise from RSOA, thus improving the optical SNR. The received electrical RF signal is mixed with a 6-GHz oscillator in a coherent homodyne demodulation and fed into an error detector for BER measurement. Due to lack of carrier recovery circuit, a single oscillator was utilized for both BPSK modulation and demodulation.

5.2 BER Performance

We first try to measure the BER for 20-km transmission without DI. However, a complete eye closure was observed and we were unable to measure the BER as the signal clock was not recoverable, confirming the severe bandwidth limitation of the RSOA.

BER measurement was then repeated with the DI being placed before the receiver for 0-, 20-, 30-, and 40-km transmission. Fig. 5.3 shows the measured BER as a function of the root-mean-square optical modulation index (OMI) of the signal measured at the output of the DI. The injection power of the seed light into the RSOA was -6.0 , -6.0 , -8.1 , and -10.6 dBm for 0, 20, 30, and 40 km, respectively. For 0- and 20-km transmission, the RSOA was biased at 41 mA. Since the effects of Rayleigh backscattering increases with fiber length, the RSOA gain was reduced by lowering its bias current as the transmission distance increased. The bias was set to 34 and 30 mA for 30- and 40-km fibers, respectively. The phase of the DI was adjusted to maximize eye opening and to minimize BER. The optical power measured at the receiver was -9.1 dBm for back-to-back transmission.

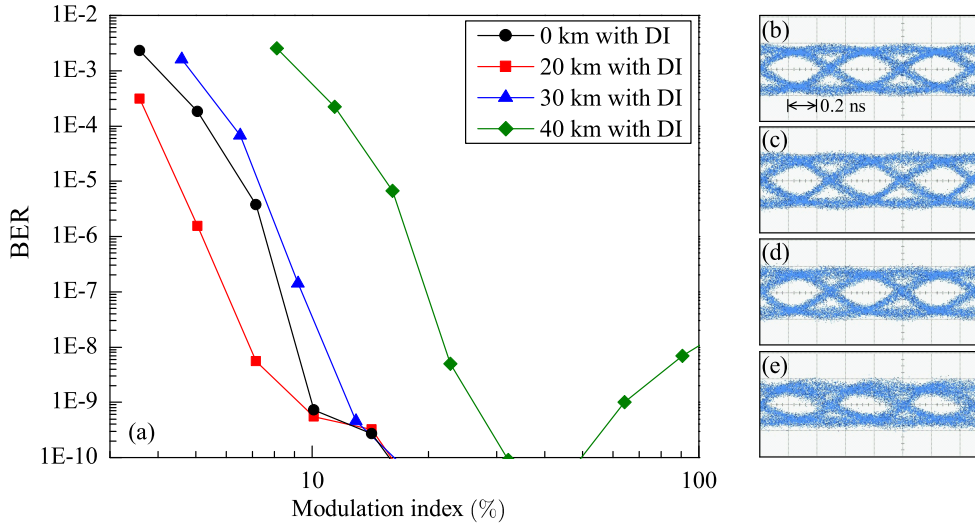


Figure 5.3: (a) Measured BER as a function of OMI for 0-, 20-, 30-, and 40-km transmission over SSMF. Plotted on the right are the electrical eye diagrams measured at the receiver after transmission over (b) 0-km at 40.2% OMI, (c) 20-km at 40.2% OMI, (d) 30-km at 36.6% OMI, and (e) 40-km at 45.5% OMI.

A BER lower than 10^{-9} is achieved when the OMI is $> 20\%$ for 0, 20, and 30 km. At these lengths, no BER degradation was observed even at a large OMI of 100%. Compared to the back-to-back measurement, we have slight improvement of BER performance after 20-km transmission. For 40-km transmission, we have an OMI penalty of 3.5 dB with respect to the back-to-back measurement. Performance degradation caused by clipping effects and nonlinear L/I characteristics of the RSOA is observed for 40-km transmission in excess of 40% OMI. A large swing in the drive current subjects the output light to clipping or nonlinear L/I region in the lower portion and to saturation at the upper portion. Nevertheless, clear eye opening in the measured electrical eye diagrams at the receiver for signals near 40% OMI as shown in Fig. 5.3(b)–(e), confirms the successful transmission up to 40 km.

5.3 Performance Improvement by DI

The successful accommodation of a wideband signal (i.e., 2 Gb/s NRZ signal at 6 GHz RF band) by RSOA and enabling of an extended transmission reach (i.e., 40 km),

made possible by the use of DI, is analyzed next.

5.3.1 Optical Filter

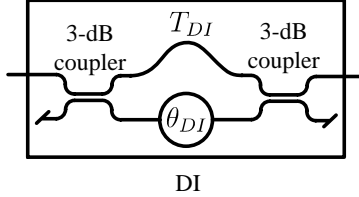


Figure 5.4: Schematic diagram of a DI.

Fig. 5.4 shows the schematic diagram of a DI comprising two 3-dB couplers connected by two arms of different lengths. The input signal is split and acquires different time delays and phase shifts, before interfering at a second coupler. The transfer function of the DI can be expressed as [137]

$$H_{DI}(\omega) = 1 + e^{j(\omega T_{DI} + \theta_{DI})} \quad (5.1)$$

where ω is the angular frequency. Here, T_{DI} is the relative time delay between the two DI arms and θ_{DI} is the adjustable phase of the DI. $H_{DI}(\omega)$ is periodic with a period $1/T_{DI}$ Hz. When θ_{DI} equals π , DI exhibits high-pass-filter characteristics up to $(2T_{DI})^{-1}$ Hz and helps to counteract the low-pass-filter characteristics of RSOA. Introduction of DI recovers the higher frequency components, effectively performing optical equalization.

The optical waveform at the input to the PIN-FET receiver after a 20-km transmission is captured with a high-speed sampling oscilloscope in Fig. 5.5. In Fig. 5.5(a) without DI, the high-frequency components such as the 6-GHz RF carrier is clearly suppressed by the low modulation bandwidth of the RSOA and the optical waveform gives only a coarse envelope of the transmitted BPSK signal. Fluctuations of the waveform is attributed to residual coupling of the input baseband NRZ signal with the output

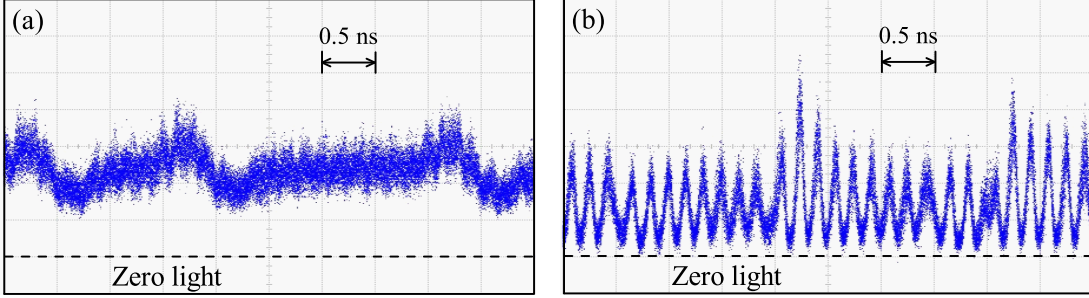


Figure 5.5: Optical waveform of the radio signal captured at the input to the PIN-FET receiver (a) without DI, and (b) with DI.

BPSK signal at the mixer. When DI is inserted, the 6-GHz RF carrier can be clearly observed in the captured optical waveform in Fig. 5.5(b). In essence, optical filtering by DI greatly enhances the bandwidth of the system.

In IMDD systems, where phase information is lost upon square-law photodetection, optical equalization is generally accepted to outperform electrical equalization [138]. Another advantage over electrical equalization is that a single DI can be used for multiple channels in WDM RoF systems thanks to the periodicity of the DI, provided the RSOAs have similar frequency response [138]. For example, a 25-GHz DI can be used in a set-and-forget mode to equalize multiple WDM channels anchored at a 100-GHz spaced frequency grid [139]. Here, the cost of the DI will be shared among the WDM tributaries and becomes insignificant as the number of channels increase.

5.3.2 Positive Chirp

Since the GVD parameter β_2 at 1550 nm for a SSMF is negative, CD broadens the pulse envelope width of an intensity modulated optical pulse on propagation in a fiber and redistributes its frequency components such that higher frequency components are pushed to the leading edge of the pulse, as shown in Fig. 5.6(a). A broadened pulse introduces ISI which limits the transmission distance.

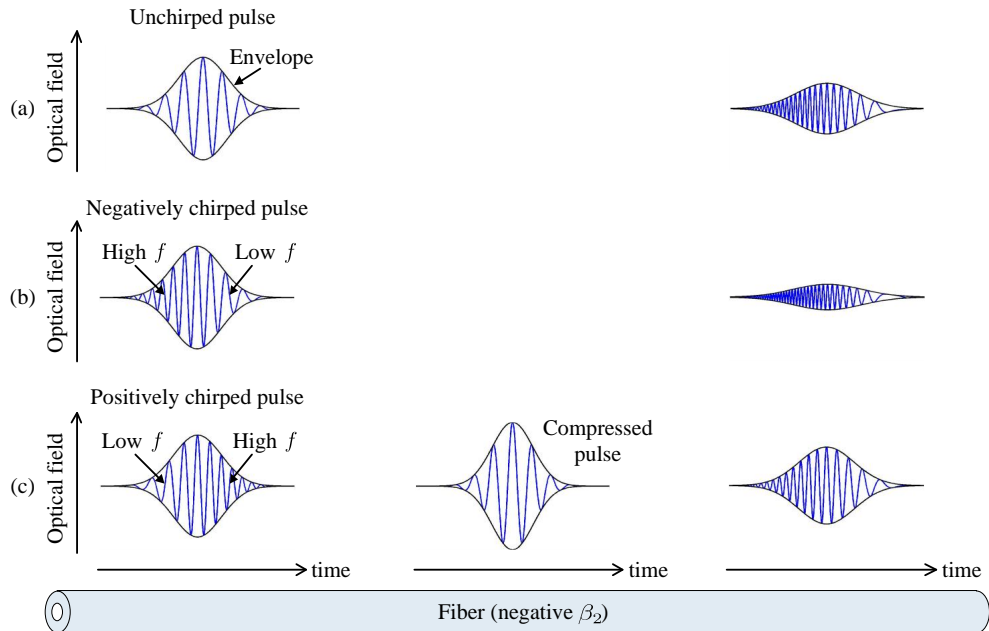


Figure 5.6: Propagation of intensity modulated optical pulses which are (a) unchirped, (b) negatively chirped, and (c) positively chirped.

The injected current, besides modulating the gain, also modulates the refractive index of the RSOA to produce a negatively chirped optical pulse [43, 140]. A pulse is said to be negatively (positively) chirped, with a negative (positive) chirp parameter C_{ch} , if its carrier frequency decreases (increases) with time. Since $\beta_2 C_{ch} > 0$ for a system employing RSOA, a negatively chirped optical pulse monotonically broadens with distance at a rate faster than an unchirped pulse [54]. Hence, negative chirping by RSOA compounds the pulse broadening effect of CD as seen in Fig. 5.6(b), making RSOAs sensitive to CD and thus further limiting the bit rate-distance product.

However, scrutinizing Fig. 5.3, BER improves briefly at 20 km before deteriorating with increase in fiber length. This is ascribed to positive chirping by DI in its SSB filtering action [137]. Fig. 5.6(c) illustrates how a positively chirped pulse with $\beta_2 C_{ch} < 0$ compensates for the GVD-induced chirp leading to an initial pulse compression, before eventual broadening [141]. In our experiment, DI's positive chirp counteracts the GVD- and RSOA-induced negative chirp, aiding a longer transmis-

sion distance of 40 km. DI is shown to be indeed capable of compensating the chirp imposed by a semiconductor optical amplifier in [142].

5.4 Rayleigh Backscattering

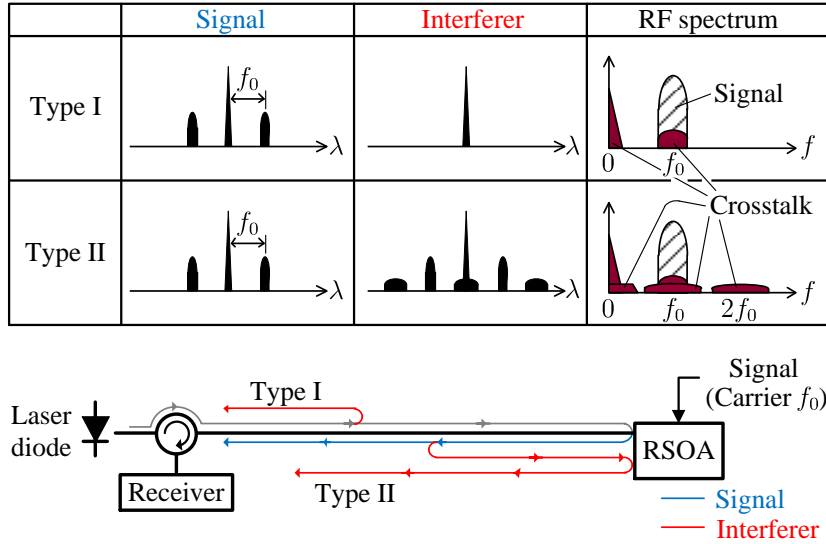


Figure 5.7: Effects of Rayleigh backscattering in RoF systems.

Rayleigh backscattering can be classified into two types, which are illustrated in Fig. 5.7 with the associated signal and resulting interferer spectra. In a single-fiber loopback network, Rayleigh backscattering-induced crosstalk can limit the maximum reach in two ways: (i) Rayleigh backscattered seed light interferes with the upstream data signal (Type I), and (ii) Rayleigh backscattered upstream data signal is modulated again by RSOA and interferes with the upstream data signal (Type II) [143]. Compared to baseband transmission, the deleterious effects of both Type-I and Type-II crosstalk are greatly reduced in an RF band transmission enabled by the DI's bandwidth equalization. As illustrated by the received RF spectra in Fig. 5.7, low-frequency Rayleigh crosstalk of Type I, which extends from zero frequency to several MHz at the receiver and accounts for 50% of the crosstalk, does not affect the high-frequency radio sig-

nal [144]. A large amount of Type-II crosstalk also falls outside the radio signal band at the receiver when the signal is confined within an octave.

5.5 Single Sideband Generation

5.5.1 Chromatic Dispersion Induced RF Power Fading

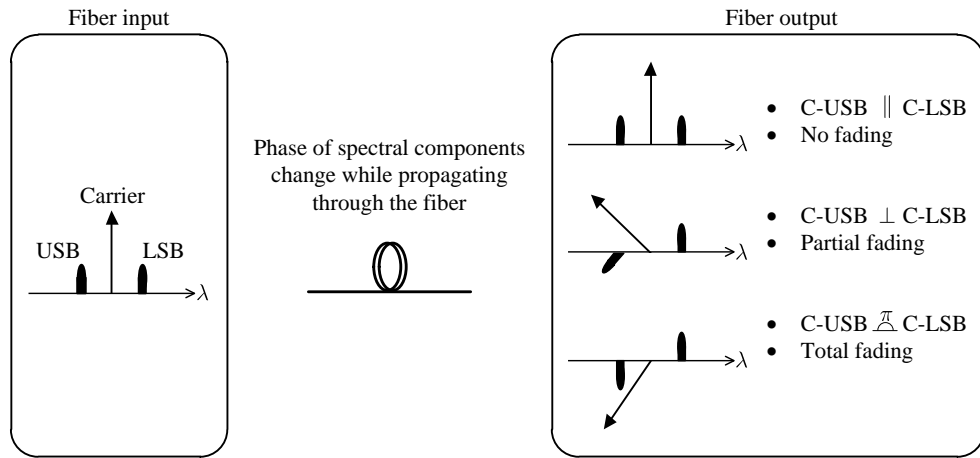


Figure 5.8: CD-induced RF power fading in a DSB signal.

Fig. 5.8 illustrates the RF power fading phenomenon. CD causes each spectral component of a signal propagating in the fiber to acquire a different phase shift depending on its frequency, fiber length, and fiber's GVD parameter, as dictated by Eq. (2.13). At the photodetector, in a DSB modulation, the upper-frequency sideband (USB) and the lower-frequency sideband (LSB) will beat with the optical carrier, thereby generating carrier-USB (C-USB) and carrier-LSB (C-LSB) beat signals which interfere to produce the electrical RF signal [44]. The relative phase shifts, induced by CD, between the carrier and each sideband causes a phase difference in the two resultant beat signals. As the phase difference deviates from zero, the electrical RF signal experiences fading caused by destructive interference between the beat signals [45]. A total fading occurs when the phase difference equals π due to a complete cancellation

between the C-USB and C-LSB beat signals.

The detected RF power of the DSB modulated optical field will vary as [145]

$$P_{RF} \propto \cos^2 \left[\frac{\pi L_f D_{CD}}{c} \lambda^2 f_{RF}^2 \right] \quad (5.2)$$

where L_f is the fiber length of dispersion D_{CD} , λ is the optical carrier wavelength, and f_{RF} is the RF frequency. Power nulls occur at fiber lengths of

$$L_f = \frac{ic}{2D_{CD}\lambda^2 f_{RF}^2}, \quad i = 1, 3, 5, \dots \quad (5.3)$$

and at RF frequencies of

$$f_{RF} = \sqrt{\frac{ic}{2D_{CD}\lambda^2 L_f}}, \quad i = 1, 3, 5, \dots \quad (5.4)$$

The RF power degradation due to CD, with $D_{CD} = 17 \text{ ps}/(\text{nm}\cdot\text{km})$, as a function of fiber length and as a function of RF frequency is shown in Fig. 5.9. Accurate adaptation of the fiber length according to the RF frequencies is needed to minimize the power penalty caused by CD-induced RF power fading [44]. As the RF frequency increases, the fading becomes more pronounced as it occurs at shorter frequency and fiber-length intervals, thus severely limiting the transmission distance and the RF frequencies that can be supported.

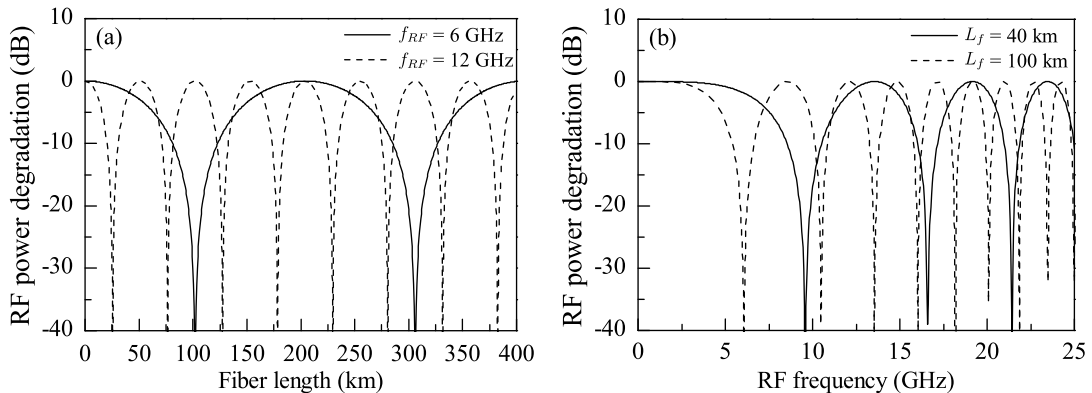


Figure 5.9: RF power degradation at the receiver for optical DSB modulation as a function of (a) fiber length and (b) RF frequency.

5.5.2 Sideband Suppression by DI

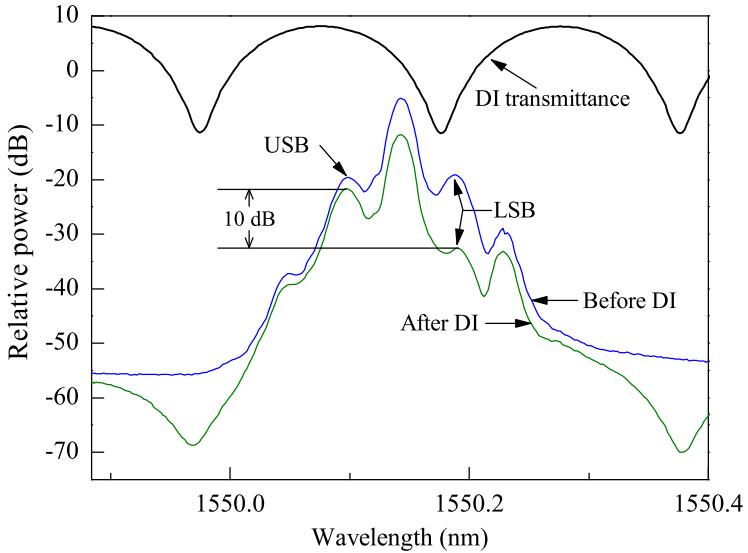


Figure 5.10: Optical spectra of the signal before and after DI. Also depicted is the transmittance of the DI.

Fig. 5.10 shows the optical spectra of the signal measured before and after the DI, after a 20 km transmission. Also depicted in the figure is the transmittance of the DI. Direct modulation of RSOA by the 6-GHz radio signal produces two small sidebands around the optical carrier. The null frequency of the DI is located 4.2 GHz off the laser diode frequency. Thus, it filters out the LSB of the RSOA output, leaving the USB and thus creating an SSB signal. The LSB of the signal at the output of the DI is suppressed by ~ 10 dB compared to the USB.

To demonstrate that our proposed scheme successfully generates optical SSB signals and averts CD-induced RF fading, we perform an RF tone fading measurement using the modified setup in Fig. 5.11 which isolates the CD effect from others. The injection power of the seed light into the RSOA is kept at -6 dBm throughout this measurement. The RSOA is directly modulated with a 6-GHz sinusoidal wave and sent to SSMF for transmission. An EDFA is employed after transmission to compensate for the fiber loss. An OBPF (i.e., OBPF 2 in Fig. 5.11) is used to reject the out-of-band

ASE noise and thus minimize the contribution of noise to the received signal power.

The optical power into the DI is kept at -7 dBm.

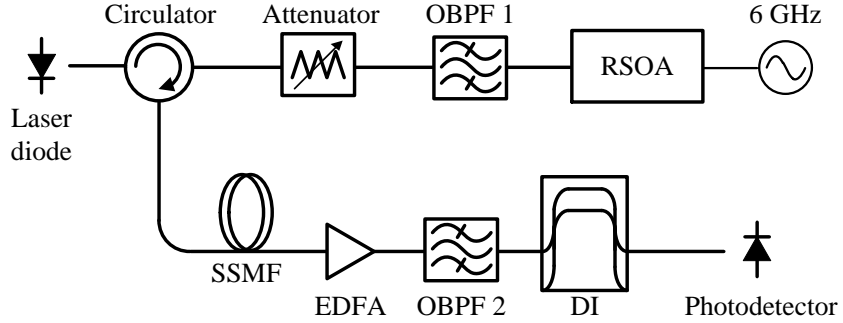


Figure 5.11: RF tone fading measurement setup.

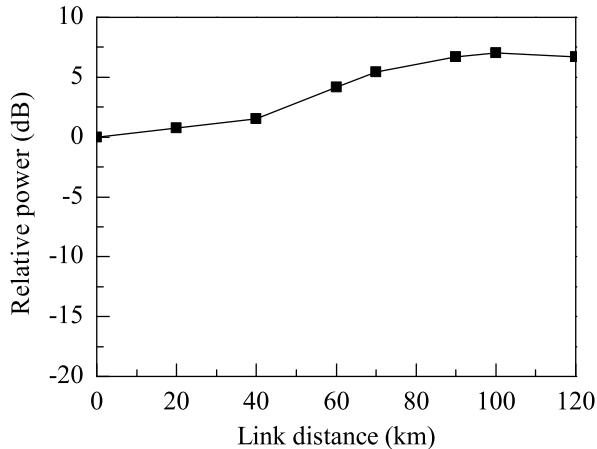


Figure 5.12: Relative RF power of a 6-GHz sinusoidal wave as a function of transmission distance over SSMF.

Fig. 5.12 plots the 6-GHz RF tone power relative to the power at 0 km as a function of link distance. The signal power at the detector is fairly constant with a small variation of 7.0 dB over 120 km. The power variation is attributed to an incomplete LSB suppression by the DI. A finite sideband suppression ratio (SSR) of 10 dB witnessed in Fig. 5.10 leads to a 5.7-dB fluctuation of the received RF power in the presence of CD as calculated using [146],

$$P_{SSR} = 20 \log_{10} \left(\frac{10^{\frac{SSR}{20}} + 1}{10^{\frac{SSR}{20}} - 1} \right) \quad (5.5)$$

which agrees with our measurement. Also seen in the Fig. 5.12 is that maximum RF power, indicative of constructive interference between the C-USB and C-LSB beat signals, is achieved at 100 km instead of at 0 km. This is because the optical signal is prechirped as the spectral components have a relative phase shift at 0 km.

5.6 Tolerable RF Carrier Frequencies and Frequency Offsets

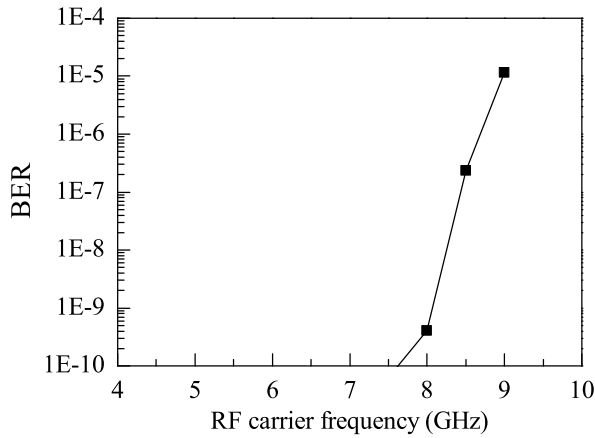


Figure 5.13: RF carrier frequency tolerance.

Fig. 5.13 shows the measured BER versus RF carrier frequency after 20-km transmission using the setup in Fig. 5.1. The received optical power is -9.1 dBm. The OMNI of the signal is set to 40.2% at 6 GHz and kept unchanged throughout this measurement. We have a $\text{BER} < 10^{-10}$ for RF carrier frequencies from 4.0 to 7.5 GHz. Due to the limited bandwidth of the system, especially that of the RSOA, the BER deteriorates rapidly when the RF carrier frequency exceeds 8 GHz.

Fig. 5.14 analyzes the tolerance of frequency offset between the laser diode and DI in the setup of Fig. 5.1. Here, zero frequency offset refers to the case when the null frequency of the DI is located 4.2 GHz off the laser diode frequency. The RF carrier frequency is 6 GHz and the received optical power is -9.1 dBm. It is found

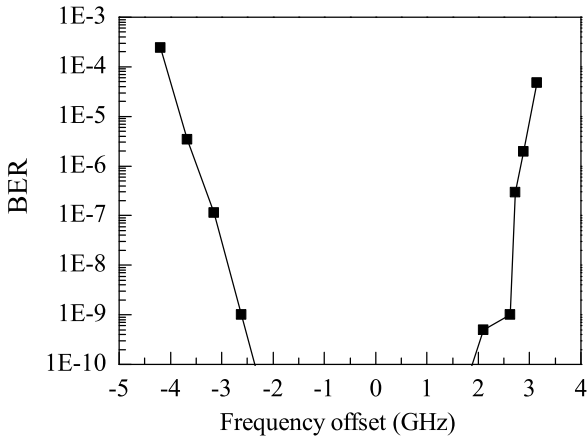


Figure 5.14: Tolerance of frequency offset between the DI and laser diode when the RF carrier frequency is 6 GHz.

that the frequency offset should be kept within ± 2 GHz to have a BER less than 10^{-9} . Since both the seed light and the DI are located in the same place (i.e., CO), frequency alignment could be easily achieved by locking the seed light wavelength to the DI [137].

5.7 Conclusion

We have proposed a novel direct detection receiver incorporating a DI for an RSOA-based IMDD RoF system. Effectiveness of our new receiver was assessed through an upstream transmission of a 2-Gb/s, 6-GHz radio signal in loopback-configured network using a directly modulated uncooled-RSOA packaged in a TO-can.

Use of DI greatly alleviates the modulation bandwidth restriction of the RSOA, enabling a 2 Gb/s uplink BPSK radio signal at an RF carrier frequency of up to 7.5 GHz. A large frequency mismatch of up to ± 2 GHz between the DI and laser diode frequency was shown to be tolerable. By virtue of DI's positive chirping action and the high-frequency octave-confined radio signal transmission which reduces the in-band intensity noise from Rayleigh backscattering, an extended link distance of up to 40 km

5.7 Conclusion

was achieved. To the best of our knowledge, this is the longest transmission distance and also highest RF carrier frequency carried over a directly modulated RSOA in a directly-detected loopback-configured network.

Moreover, signal fading problem in DSB signals were overcome by DI which suppresses a sideband to generate optical SSB signals just prior to photodetection. Our new optical receiver design is easily implementable as only an additional DI placement is required at the CO, with no changes at the RBSs.

Chapter 6

Conclusion

6.1 Summary of Main Contributions

First, we addressed the coherent optical receiver design problem with respect to carrier phase and frequency estimation, for nonbinary modulations which are essential in improving the spectral efficiency. Nonbinary modulation, compared to binary modulation, is also more robust against transmission impairments, including CD and PMD [9]. A new joint phase noise and frequency offset estimator, named CW-DA-ML, was derived in Chapter 3. The modulation-agnostic CW-DA-ML achieves better $\Delta\nu T$ and ΔfT tolerance than FFTFE-MPE, DiffFE-MPE, and DA-ML. CW-DA-ML is superior in carrier estimation accuracy at low SNR and/or sample size N , compared to FFTFE-MPE and DiffFE-MPE. This is crucial, given the development of advanced FEC codes with low BER thresholds which lowers the target operating SNR of modern systems. Moreover, it is desirable to operate at lower signal power to reduce fiber nonlinearity. Aided by the absence of phase unwrapping and higher order noises, CW-DA-ML achieves lower cycle slip probability than MPE. Bolstered by the low cycle slip probability, a PA CW-DA-ML with low pilot overhead of 0.2% is demonstrated. Symbol-by-symbol tracking feature and fast convergence behavior helps CW-DA-ML to reliably track time-varying frequency offset. Additionally, the phase noise tolerance

6.1 Summary of Main Contributions

and cycle slip probability of several 4-, 8-, and 16-point constellations were analyzed.

Next, we established the need for receivers having carrier estimators with adaptive filter length to optimize the BER in future reconfigurable optical networks. Hence, adaptive CW-DA estimator with an effective filter length that automatically adapts according to the SNR, $\Delta\nu T$, nonlinear phase noise, and modulation format was presented in Chapter 4. It can operate in a set-and-forget mode as it requires no *a priori* system statistics and no preset parameters. The filter length of a carrier estimator is shown to affect the cycle slip probability besides the BER. Considering that FEC codes are not robust to burst errors and cycle slips, we demonstrate that filter-length optimization is necessary to avoid spectral-efficiency reduction in PA systems and potential system failures in differential encoding systems. Our estimator achieves a lower cycle slip probability and a greater nonlinear phase noise tolerance than DiffFE-MPE, DiffFE-BPS, and CW-DA-ML. Reduced complexity, due to the two-tap structure, makes adaptive CW-DA estimator favorable for practical implementation.

Finally, in Chapter 5, we considered the direct-detection receiver design for an RoF system employing RSOA at the RBSs. We proposed to incorporate an optical DI before the photodetector at the receiver and demonstrated the receiver with an upstream transmission of a 2-Gb/s 6-GHz BPSK radio signal using RSOA in a single-fiber loopback network. The DI, acting as an optical equalizer, compensates for the limited RSOA modulation bandwidth. SSB filtering by DI relieves the CD-induced RF fading effect and helps to overcome the maximum link-length cap. Furthermore, extended transmission distance of up to 40 km is shown to be made possible by the (i) positive chirp of DI which offsets the negative chirp of GVD and RSOA, and (ii) reduced Rayleigh backscattering induced in-band crosstalk. Gradual shifting of wireless services to higher RF bands with increasing data rates places the proposed system as a strong contender, due to its direct modulated RSOA capability up to 7.5 GHz band encoded by 2 Gb/s signal and simple RBSs requiring no additional signal processing.

6.2 Suggestions for Future Research

The contributions in the previous chapters lead naturally to various avenues for further research. We mention some possible extensions in the following subsections.

6.2.1 Carrier Estimators for Space-Division Multiplexed Systems

Currently, space-division multiplexing (SDM) of parallel data streams in the cores of multicore fibers or in the modes of multimode fibers is of immense research interest to increase capacity per fiber as the capacity limit of SSMFs are approached [147, 148]. Coherent detection and multiple-input multiple-output DSP is used in the receiver to recover the spatial data streams, which might be significantly mixed [149]. Key DSP steps include carrier phase and frequency estimation.

It is desirable to further develop CW-DA-ML [124] and adaptive CW-DA [150] estimators for carrier estimation application in SDM systems. Spatial coupling causes phase and frequency fluctuations between modes (or cores) to be correlated, resulting in common-mode impairments which can be exploited by joint carrier estimation of multiple received channels [151]. A performance comparison, with the master-slave phase estimator for multicore fibers proposed by [151] and the single digital PLL-based joint carrier estimation of multiple channels in few-mode fibers proposed by [152], will be in order. For simulation of carrier estimators in SDM systems, understanding of mode coupling is necessary and [153] gives a preliminary insight into emulating a linear propagation in few-mode fibers.

6.2.2 Equalizers with Adaptive Filter Length

Preset constant filter length has been an inherent feature of equalizers described for dispersion compensation in the literature, for example see [154]. Following the mo-

tivation in the introduction of Chapter 4, equalizers with fully adaptive filter length are desirable to compensate for time-varying dispersion due to utilization of different transmission paths in reconfigurable optical networks. However, equalizers with adaptive filter length has received little attention in optical communications. Given that the equalization performance and complexity are nondecreasing function of the filter length, the challenge is to intelligently decide on a sufficient filter length which best balances equalization performance with complexity.

Several efforts in seeking the best filter length include use of gradually increasing filter length [155], segmented filter structure [156], two competing filters of different lengths [157], and least-mean square styled variable filter length [158]. However, these methods (i) allow only filter-length increment, (ii) require filter-length change in fixed step sizes, (iii) sensitive to design parameter choice which are subjective and needs to be manually tuned, or (iv) assume *a priori* knowledge of the desired signal making it not suitable for blind signal processing. The above methods are also untested for dispersion compensation in optical communications.

Another possible route to pursue in realizing equalizers with adaptive filter length is the implementation of equalizers in the form of order-recursive lattice filters [159]. A lattice filter of order (or length) L_{latt} consists of a cascade of L_{latt} elementary stages, where each stage is statistically decoupled from the others. Hence, the modular structure of the lattice filter lends itself to the implementation of a variable filter order as the filter order can be changed by simply adding or removing stages without affecting earlier computations.

6.2.3 Phase-Modulated Coherent Detection RoF System

RoF, or the use of optical fiber for delivery of radio services, is a promising technology for the burgeoning next-generation wireless networks, as it provides a large bandwidth

6.2 Suggestions for Future Research

and a graceful evolution strategy due to its transparent optical transport of wireless signals [32]. Phase-modulated RoF links with coherent detection offers numerous advantages over IMDD links. Electrical-to-optical encoding by optical phase modulators is linear and provides higher modulation depths, in contrast to IMDD's inherently non-linear modulation transfer characteristic which limits the dynamic range [160, 161]. Compared to intensity modulation, constant-intensity phase modulation is less vulnerable to fiber nonlinearities and requires no dc bias at the RBS which eliminates performance degradation due to potential drifting of A_{dc} bias in Eq. (1.4) [162]. Coherent detection can also offer increased receiver sensitivity and spurious-free dynamic range compared to direct-detection links [163]. Additionally, coherent detection allows better frequency selectivity and closer channel spacing in WDM systems [164].

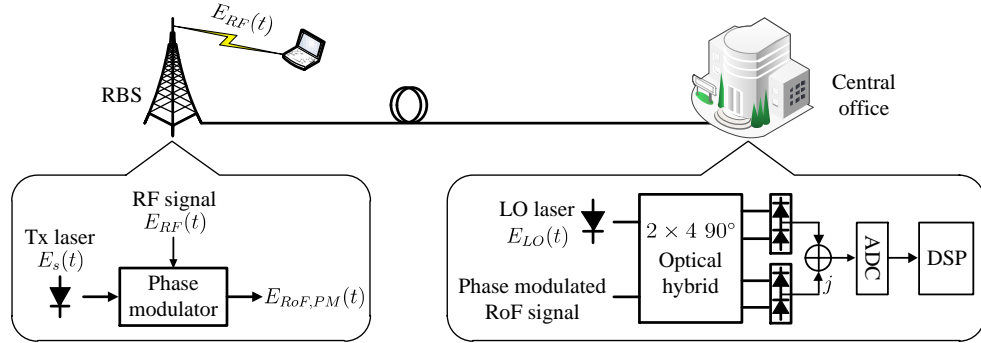


Figure 6.1: Phase-modulated RoF link with coherent detection.

The phase-modulated RoF uplink is illustrated in Fig. 6.1. Optical field of the transmitter laser is modeled as $E_s(t) = \exp(j(\theta_s(t) + \omega_s t))$, where $\theta_s(t)$ and ω_s are the phase noise and angular frequency of the transmitter laser, respectively. The received RF signal $E_{RF}(t)$, given by Eq. (1.3), at the RBS is used to drive a LiNbO₃ optical phase modulator which linearly encodes $E_{RF}(t)$ onto the phase of the transmitter laser. The resultant optical field launched into the fiber is

$$E_{RoF,PM}(t) = \exp\left[j\left(\theta_s(t) + \omega_s t + \frac{\pi}{V_\pi} A(t) \cos(\phi(t) + 2\pi f_0 t)\right)\right], \quad (6.1)$$

where π/V_π is the modulation depth factor, with V_π being the half-wave voltage of the phase modulator [165].

At the CO, the phase modulated RoF signal is mixed with a LO laser $E_{LO}(t)$, given by Eq. (2.9), in a 2×4 90° optical hybrid and detected by balanced photodetectors. Following the coherent signal reception described in Section 2.2.3 and assuming no ISI or nonlinear distortion, the sampled photodetector output is

$$\begin{aligned} r_{RoF,PM}(l\bar{T}) = & R\sqrt{P_{LO}} \\ & \times \exp\left[j\left(\theta(l\bar{T}) + \Delta\omega(l\bar{T}) + \frac{\pi}{V_\pi} A(l\bar{T}) \cos(\phi(l\bar{T}) + 2\pi f_0 l\bar{T})\right)\right] \end{aligned} \quad (6.2)$$

where $l = 0, 1, 2 \dots$ is an integer, $\bar{T} = T/T_0$ is the sampling interval, and other variables are as defined in Section 2.2.

Key to obtaining the benefits of phase modulated RoF is carrier estimation of θ , $\Delta\omega$, and f_0 in Eq. (6.2) for linear demodulation of the data signal [161]. A carrier estimator comprising a digital PLL to estimate θ and $\Delta\omega$, followed by a linear phase extractor, and an RF carrier recovery to estimate f_0 was proposed in [166]. However, a complete study of the admissible symbol rates, modulation formats, $\Delta\nu$, Δf , and f_0 , of the carrier estimator remains unexplored. The carrier estimator of [166] is not format transparent, and requires complicated manual loop parameter optimization between the competing demands of good BER and acquisition time or estimation range.

Format-transparent, adaptive, carrier estimators for phase modulated RoF signals with good $\Delta\nu$ tolerance, Δf tolerance, f_0 estimation range, and without any preset parameters remain to be developed.

Appendix A

Derivation of DA-ML Phase Estimator

The likelihood function $\Lambda(\theta, k + 1)$ is given by the joint PDF $p(r(k), \dots, r(k - L + 1)|\theta)$. Given the assumption of no ISI, $r(k)$ and $r(l)$ are independent since $n(k)$ and $n(l)$ are independent for $k \neq l$. Hence, the likelihood function can be written as

$$\Lambda(\theta, k + 1) = \prod_{l=k-L+1}^k p(r(l)|\theta) \quad (\text{A.1})$$

In carrier-suppressed modulation formats, it is possible to arrange the signal points in the constellation as $s_i = -s_{i+M/2}$. Substituting the PDF

$$p(r(l)|\theta) = \sum_{i=0}^{M-1} p(r(l)|\theta, m(l) = s_i) p(m(l) = s_i) \quad (\text{A.2})$$

and

$$p(r(l)|\theta, m(l) = s_i) = \frac{1}{\pi\sigma_n^2} \exp\left[-\frac{|r(l) - s_i e^{j\theta}|^2}{\sigma_n^2}\right], \quad (\text{A.3})$$

where $p(m(l) = s_i) = 1/M$, into Eq. (A.1) gives

$$\begin{aligned} \Lambda(\theta, k + 1) &= \prod_{l=k-L+1}^k \sum_{i=0}^{M-1} \frac{1}{M\pi\sigma_n^2} \exp\left[-\frac{|r(l) - s_i e^{j\theta}|^2}{\sigma_n^2}\right] \\ &= \prod_{l=k-L+1}^k \frac{1}{M\pi\sigma_n^2} \exp\left[-\frac{|r(l)|^2}{\sigma_n^2}\right] \\ &\times \sum_{i=0}^{M-1} \exp\left[-\frac{|s_i|^2}{\sigma_n^2}\right] \exp\left[\frac{2\mathbf{Re}[r(l)s_i^* e^{-j\theta}]}{\sigma_n^2}\right]. \end{aligned} \quad (\text{A.4})$$

The terms s_i and $s_{i+M/2}$ in Eq. (A.4) can be combined using the identity $\cosh(a) = (e^a + e^{-a})/2$ since $s_i = -s_{i+M/2}$ for $i = 0, \dots, (M/2) - 1$. Hence we have,

$$\begin{aligned} \Lambda(\theta, k+1) &= \prod_{l=k-L+1}^k \frac{1}{M\pi\sigma_n^2} \exp\left[-\frac{|r(l)|^2}{\sigma_n^2}\right] \\ &\quad \times \sum_{i=0}^{\frac{M}{2}-1} \exp\left[-\frac{|s_i|^2}{\sigma_n^2}\right] \cosh\left[\frac{2\mathbf{Re}[r(l)s_i^*e^{-j\theta}]}{\sigma_n^2}\right]. \end{aligned} \quad (\text{A.5})$$

The log-likelihood function $\ln \Lambda(\theta, k+1)$ can now be written as

$$\begin{aligned} \ln \Lambda(\theta, k+1) &= \sum_{l=k-L+1}^k \ln \left[\sum_{i=0}^{\frac{M}{2}-1} \exp\left[-\frac{|s_i|^2}{\sigma_n^2}\right] \cosh\left[\frac{2\mathbf{Re}[r(l)s_i^*e^{-j\theta}]}{\sigma_n^2}\right] \right] \\ &\quad + \sum_{l=k-L+1}^k \ln \left[\frac{1}{M\pi\sigma_n^2} \exp\left[-\frac{|r(l)|^2}{\sigma_n^2}\right] \right] \end{aligned} \quad (\text{A.6})$$

Solving $\partial \ln \Lambda(\theta, k+1)/\partial \theta = 0$ at $\theta = \hat{\theta}(k+1)$ gives the maximum likelihood phase estimate $\hat{\theta}(k+1)$ as

$$\begin{aligned} \cos \hat{\theta}(k+1) &= \sum_{l=k-L+1}^k \frac{\sum_{i=0}^{\frac{M}{2}-1} \exp(-\bar{s}_i) \sinh[\Gamma_i(l, \hat{\theta}(k+1))] \mathbf{Im}[r(l)s_i^*]}{\sum_{i=0}^{\frac{M}{2}-1} \exp(-\bar{s}_i) \cosh[\Gamma_i(l, \hat{\theta}(k+1))]} \\ &= \sin \hat{\theta}(k+1) \sum_{l=k-L+1}^k \frac{\sum_{i=0}^{\frac{M}{2}-1} \exp(-\bar{s}_i) \sinh[\Gamma_i(l, \hat{\theta}(k+1))] \mathbf{Re}[r(l)s_i^*]}{\sum_{i=0}^{\frac{M}{2}-1} \exp(-\bar{s}_i) \cosh[\Gamma_i(l, \hat{\theta}(k+1))]} \end{aligned} \quad (\text{A.7})$$

where for simplicity we have let $\bar{s}_i = |s_i|^2/\sigma_n^2$ and $\Gamma_i(l, \hat{\theta}(k+1)) = (2/\sigma_n^2)\mathbf{Re}[r(l)s_i^*e^{-j\hat{\theta}(k+1)}]$.

It is difficult to explicitly solve the highly nonlinear Eq. (A.7) for $\hat{\theta}(k+1)$, hence a decision feedback approach is adopted to derive an implementable structure. Assuming $\hat{\theta}(l)$ has been obtained, the symbol detector uses it to produce a symbol decision $\hat{m}(l)$ for sample $r(l)$ according to Eq. (2.25). For BPSK at high SNR, since $M = 2$ and $\tanh(a) \approx \text{sgn}(a)$ at large a , Eq. (A.7) reduces to

$$\hat{\theta}(k+1) = \arctan \left[\frac{\sum_{l=k-L+1}^k \mathbf{Im}[r(l)\hat{m}^*(l)]}{\sum_{l=k-L+1}^k \mathbf{Re}[r(l)\hat{m}^*(l)]} \right] \quad (\text{A.8})$$

where the trial signal point s_i has been replaced with the symbol decision $\hat{m}(l)$. In the case of signal constellations with $M > 2$, for a fixed l in Eq. (A.7), each of the summations over i is dominated in magnitude by the s_i which matches the symbol decision $\hat{m}(l)$. Thus, Eq. (A.7) again reduces to Eq. (A.8) when s_i is replaced with $\hat{m}(l)$. This decision-feedback approximation is more accurate for $M = 2$ than for $M > 2$.

Equation (A.8) can be written in an equivalent form using a complex phasor $U(k+1)$

$$U(k+1) = \sum_{l=k-L+1}^k r(l)\hat{m}^*(l) \quad (\text{A.9})$$

whose argument gives the maximum likelihood phase estimate, i.e., $\arg(U(k+1)) = \hat{\theta}(k+1)$.

Appendix B

Derivation of $\hat{\mathbf{w}}$ in CW-DA-ML

The cost function $J(k)$ of Eq. (3.5) can be rewritten as follows:

$$\begin{aligned} J(k) &= \sum_{l=1}^k e^*(l)e(l) \\ &= \sum_{l=1}^k \left[\frac{r^*(l)}{\hat{m}^*(l)} - C(l-1)\mathbf{w}^H(k)\mathbf{y}^*(l-1) \right] \left[\frac{r(l)}{\hat{m}(l)} - C(l-1)\mathbf{w}^T(k)\mathbf{y}(l-1) \right] \end{aligned} \quad (\text{B.1})$$

By treating \mathbf{w} and \mathbf{w}^* as independent variables, we may solve for the stationary points of the real-valued function $J(k, \mathbf{w}, \mathbf{w}^*)$ using the following theorem [167].

Theorem B.1. *If $f(\mathbf{b}, \mathbf{b}^*)$ is a real-valued function of the complex vectors \mathbf{b} and \mathbf{b}^* , then the vector pointing in the direction of the maximum rate of change of $f(\mathbf{b}, \mathbf{b}^*)$ is $\partial f(\mathbf{b}, \mathbf{b}^*)/\partial \mathbf{b}^*$, which is the partial derivative of $f(\mathbf{b}, \mathbf{b}^*)$ with respect to \mathbf{b}^* .*

Hence, taking partial derivative of Eq. (B.1) with respect to $\mathbf{w}^*(k)$, we have

$$\begin{aligned} \frac{\partial J(k)}{\partial \mathbf{w}^*(k)} &= \sum_{l=1}^k \frac{\partial \left[\frac{r^*(l)}{\hat{m}^*(l)} - C(l-1)\mathbf{w}^H(k)\mathbf{y}^*(l-1) \right]}{\partial \mathbf{w}^*(k)} e(l) \\ &= \sum_{l=1}^k [-C(l-1)\mathbf{y}^*(l-1)]e(l). \end{aligned} \quad (\text{B.2})$$

In the above step, we have used the vector differentiation identity:

$$\frac{\partial(a - \mathbf{w}^H \mathbf{b})}{\partial \mathbf{w}^*} = -\mathbf{b}, \quad (\text{B.3})$$

where a is a scalar and \mathbf{b} is a vector. Next, we rearrange the term $\mathbf{w}^T(k)\mathbf{y}(l-1)$ to $\mathbf{y}^T(l-1)\mathbf{w}(k)$ in $e(l)$. Finally, solving $\partial J(k)/\partial \mathbf{w}^*(k) = 0$ yields the least-squares optimum weight vector $\hat{\mathbf{w}}(k)$ as

$$\begin{aligned} 0 &= \sum_{l=1}^k [-C(l-1)\mathbf{y}^*(l-1)]e(l) \\ \sum_{l=1}^k C(l-1)\frac{r(l)}{\hat{m}(l)}\mathbf{y}^*(l-1) &= \sum_{l=1}^k C^2(l-1)\mathbf{y}^*(l-1)\mathbf{y}^T(l-1)\hat{\mathbf{w}}(k) \\ \hat{\mathbf{w}} &= \left[\sum_{l=1}^k C^2(l-1)\mathbf{y}^*(l-1)\mathbf{y}^T(l-1) \right]^{-1} \sum_{l=1}^k C(l-1)\frac{r(l)}{\hat{m}(l)}\mathbf{y}^*(l-1) \end{aligned} \quad (\text{B.4})$$

Appendix C

Recursive Update of $\hat{\mathbf{w}}$ in CW-DA-ML

It is straightforward to see that Eq. (3.7) and Eq. (3.8) can be updated recursively as

$$\Phi(k) = \Phi(k-1) + C^2(k-1)\mathbf{y}^*(k-1)\mathbf{y}^T(k-1), \quad (\text{C.1})$$

$$\mathbf{z}(k) = \mathbf{z}(k-1) + C(k-1)\frac{r(k)}{\hat{m}(k)}\mathbf{y}^*(k-1). \quad (\text{C.2})$$

A special form of the matrix inversion lemma is [168]

$$(\mathbf{A} + a\mathbf{b}\mathbf{b}^H)^{-1} = \mathbf{A}^{-1} - \frac{a\mathbf{A}^{-1}\mathbf{b}\mathbf{b}^H\mathbf{A}^{-1}}{1 + a\mathbf{b}^H\mathbf{A}^{-1}\mathbf{b}} \quad (\text{C.3})$$

for an arbitrary nonsingular L -by- L matrix \mathbf{A} , an L -by-1 vector \mathbf{b} , and a scalar a .

Making the following identifications

$$\mathbf{A} = \Phi(k-1) \quad (\text{C.4})$$

$$\mathbf{b} = \mathbf{y}^*(k-1) \quad (\text{C.5})$$

$$a = C^2(k-1) \quad (\text{C.6})$$

and substituting them into Eq. (C.3), we obtain the recursive equation for updating the inverse of $\Phi(k)$:

$$\Phi^{-1}(k) = \Phi^{-1}(k-1) - \frac{C^2(k-1)\Phi^{-1}(k-1)\mathbf{y}^*(k-1)\mathbf{y}^T(k-1)\Phi^{-1}(k-1)}{1 + C^2(k-1)\mathbf{y}^T(k-1)\Phi^{-1}(k-1)\mathbf{y}^*(k-1)}. \quad (\text{C.7})$$

For convenience we define a gain vector $\mathbf{g}(k)$, as follows

$$\mathbf{g}(k) = \frac{C(k-1)\Phi^{-1}(k-1)\mathbf{y}^*(k-1)}{1 + C^2(k-1)\mathbf{y}^T(k-1)\Phi^{-1}(k-1)\mathbf{y}^*(k-1)}. \quad (\text{C.8})$$

Incorporating the above definition into Eq. (C.7), we obtain

$$\Phi^{-1}(k) = \Phi^{-1}(k-1) - \mathbf{g}(k)C(k-1)\mathbf{y}^T(k-1)\Phi^{-1}(k-1). \quad (\text{C.9})$$

By rearranging the gain vector in Eq. (C.8), we have

$$\mathbf{g}(k) = [\Phi^{-1}(k-1) - \mathbf{g}(k)C(k-1)\mathbf{y}^T(k-1)\Phi^{-1}(k-1)]C(k-1)\mathbf{y}^*(k-1). \quad (\text{C.10})$$

Using Eq. (C.9), we recognize the term multiplying $C(k-1)\mathbf{y}^*(k-1)$ in Eq. (C.10) is $\Phi^{-1}(k)$. Hence, we can express the gain vector as

$$\mathbf{g}(k) = \Phi^{-1}(k)C(k-1)\mathbf{y}^*(k-1). \quad (\text{C.11})$$

Next, to derive the recursive time-update equation for the optimum filter-weight vector $\hat{\mathbf{w}}(k)$, we express Eq. (3.6) using Eq. (C.2) and Eq. (C.11) as

$$\begin{aligned} \hat{\mathbf{w}}(k) &= \Phi^{-1}(k)\mathbf{z}(k-1) + \Phi^{-1}(k)C(k-1)\frac{r(k)}{\hat{m}(k)}\mathbf{y}^*(k-1) \\ &= \Phi^{-1}(k)\mathbf{z}(k-1) + \mathbf{g}(k)\frac{r(k)}{\hat{m}(k)}. \end{aligned} \quad (\text{C.12})$$

Substituting $\Phi^{-1}(k)$ in the above equation with Eq. (C.9), we get

$$\begin{aligned} \hat{\mathbf{w}}(k) &= \Phi^{-1}(k-1)\mathbf{z}(k-1) - \mathbf{g}(k)C(k-1)\mathbf{y}^T(k-1)\Phi^{-1}(k-1)\mathbf{z}(k-1) \\ &\quad + \mathbf{g}(k)\frac{r(k)}{\hat{m}(k)} \\ &= \hat{\mathbf{w}}(k-1) - \mathbf{g}(k)C(k-1)\mathbf{y}^T(k-1)\hat{\mathbf{w}}(k-1) + \mathbf{g}(k)\frac{r(k)}{\hat{m}(k)} \\ &= \hat{\mathbf{w}}(k-1) + \mathbf{g}(k)\left[\frac{r(k)}{\hat{m}(k)} - C(k-1)\hat{\mathbf{w}}^T(k-1)\mathbf{y}(k-1)\right] \\ &= \hat{\mathbf{w}}(k-1) + \mathbf{g}(k)\xi(k) \end{aligned} \quad (\text{C.13})$$

where

$$\begin{aligned}\xi(k) &= \frac{r(k)}{\hat{m}(k)} - C(k-1)\hat{\mathbf{w}}^T(k-1)\mathbf{y}(k-1) \\ &= \frac{r(k)}{\hat{m}(k)} - V(k)\end{aligned}\tag{C.14}$$

is the *a priori* estimation error.

Finally, $\mathbf{g}(k)$ of Eq. (C.8), $\xi(k)$ Eq. (C.14), $\hat{\mathbf{w}}(k)$ of Eq. (C.13), and $\Phi^{-1}(k)$ of Eq. (C.9), in this order, describe one iteration of the weight-vector update. We may add an additional step of computing an intermediate vector

$$\psi(k) = C(k-1)\Phi^{-1}(k-1)\mathbf{y}^*(k-1)\tag{C.15}$$

at the beginning of the weight-vector update, to simplify the duplicate computation of $\psi(k)$ in the gain vector $\mathbf{g}(k)$ and $\psi^H(k)$ in the inverse autocorrelation matrix $\Phi^{-1}(k)$, as illustrated in Table 3.1.

Appendix D

Derivation of $\hat{\mathbf{w}}$ in Adaptive CW-DA Estimator

First, let's represent Eq. (4.3) in a concise vector form as

$$\begin{aligned}\bar{V}(k+1) &= w_1 \bar{V}(k) + w_2 x(k) \\ &= \begin{bmatrix} w_1 & w_2 \end{bmatrix} \begin{bmatrix} \bar{V}(k) \\ x(k) \end{bmatrix} \\ &= \mathbf{w}^T \mathbf{y}(k)\end{aligned}\tag{D.1}$$

where $\mathbf{y}(k)$ is the filter-input vector $[\bar{V}(k), x(k)]^T$. By substituting $\bar{V}(l)$ in Eq. (4.4) with Eq. (D.1), the cost function can be rewritten as

$$\begin{aligned}J(k) &= \sum_{l=1}^k |x(l) - \mathbf{w}^T \mathbf{y}(l-1)|^2 \\ &= \sum_{l=1}^k [x^*(l) - \mathbf{w}^H \mathbf{y}^*(l-1)] [x(l) - \mathbf{w}^T \mathbf{y}(l-1)].\end{aligned}\tag{D.2}$$

Since $J(k)$ is a real valued function of \mathbf{w} and \mathbf{w}^* , we proceed as per Theorem B.1:

$$\begin{aligned}\frac{\partial J(k)}{\partial \mathbf{w}^*} &= \sum_{l=1}^k \frac{\partial [x^*(l) - \mathbf{w}^H \mathbf{y}^*(l-1)]}{\partial \mathbf{w}^*} [x(l) - \mathbf{w}^T \mathbf{y}(l-1)] \\ &= \sum_{l=1}^k [-\mathbf{y}^*(l-1)] [x(l) - \mathbf{y}^T(l-1) \mathbf{w}]\end{aligned}\tag{D.3}$$

where we had used the identity in Eq. (B.3) and had rearranged the term $\mathbf{w}^T \mathbf{y}(l-1)$ to $\mathbf{y}^T(l-1)\mathbf{w}$. Finally, we equate Eq. (D.3) to zero to obtain the $\hat{\mathbf{w}}$ which minimizes $J(k)$ as

$$\begin{aligned}
 0 &= \sum_{l=1}^k [-\mathbf{y}^*(l-1)] [x(l) - \mathbf{y}^T(l-1)\hat{\mathbf{w}}] \\
 \sum_{l=1}^k x(l)\mathbf{y}^*(l-1) &= \sum_{l=1}^k \mathbf{y}^*(l-1)\mathbf{y}^T(l-1)\hat{\mathbf{w}} \\
 \hat{\mathbf{w}} &= \left[\sum_{l=1}^k \mathbf{y}^*(l-1)\mathbf{y}^T(l-1) \right]^{-1} \cdot \sum_{l=1}^k x(l)\mathbf{y}^*(l-1) \\
 \begin{bmatrix} \hat{w}_1 \\ \hat{w}_2 \end{bmatrix} &= \left[\sum_{l=1}^k \begin{bmatrix} |\bar{V}(l-1)|^2 & \bar{V}^*(l-1)x(l-1) \\ x^*(l-1)\bar{V}(l-1) & |x(l-1)|^2 \end{bmatrix} \right]^{-1} \cdot \sum_{l=1}^k x(l) \begin{bmatrix} V^*(l-1) \\ x^*(l-1) \end{bmatrix}
 \end{aligned} \tag{D.4}$$

Bibliography

- [1] T. H. Maiman, “Stimulated optical radiation in ruby,” *Nature*, vol. 187, no. 4736, pp. 493–494, Aug. 1960.
- [2] K. C. Kao and G. A. Hockham, “Dielectric-fibre surface waveguides for optical frequencies,” *Proc. IEE*, vol. 113, no. 7, pp. 1151–1158, Jul. 1966.
- [3] P. J. Winzer, “Beyond 100G ethernet,” *IEEE Commun. Mag.*, vol. 48, no. 7, pp. 26–30, Jul. 2010.
- [4] A. H. Gnauck, P. J. Winzer, S. Chandrasekhar, X. Liu, B. Zhu, and D. W. Peckham, “Spectrally efficient long-haul WDM transmission using 224-Gb/s polarization-multiplexed 16-QAM,” *J. Lightw. Technol.*, vol. 29, no. 4, pp. 373–377, Feb. 2011.
- [5] K.-P. Ho, “Exact evaluation of the capacity for intensity-modulated direct-detection channels with optical amplifier noises,” *IEEE Photon. Technol. Lett.*, vol. 17, no. 4, pp. 858–860, Apr. 2005.
- [6] C. E. Shannon, “A mathematical theory of communication,” *Bell Syst. Tech. J.*, vol. 27, no. 3, pp. 379–423, Jul. 1948.
- [7] R. J. Essiambre, G. Kramer, P. J. Winzer, G. J. Foschini, and B. Goebel, “Capacity limits of optical fiber networks,” *J. Lightw. Technol.*, vol. 28, no. 4, pp. 662–701, Feb. 2010.
- [8] E. Ip, A. P. T. Lau, D. J. F. Barros, and J. M. Kahn, “Coherent detection in optical fiber systems,” *Opt. Exp.*, vol. 16, no. 2, pp. 753–791, Jan. 2008.
- [9] J. M. Kahn and K.-P. Ho, “Spectral efficiency limits and modulation/detection techniques for DWDM systems,” *IEEE J. Sel. Topics Quantum Electron.*, vol. 10, no. 2, pp. 259–272, Mar./Apr. 2004.
- [10] E. Desurvire, “Fundamental information-density limits in optically amplified transmission: an entropy analysis,” *Opt. Lett.*, vol. 25, no. 10, pp. 701–703, May 2000.
- [11] A. Mecozzi and M. Shtaif, “On the capacity of intensity modulated systems using optical amplifiers,” *IEEE Photon. Technol. Lett.*, vol. 13, no. 9, pp. 1029–1031, Sep. 2001.

Bibliography

- [12] J. M. Geist, “Capacity and cutoff rate for dense M-ary PSK constellations,” in *Proc. IEEE Mil. Commun. Conf. Record*, Monterey, CA, 1990, pp. 768–770.
- [13] J. P. Aldis and A. G. Burr, “The channel capacity of discrete time phase modulation in AWGN,” *IEEE Trans. Inf. Theory*, vol. 39, no. 1, pp. 184–185, Jan. 1993.
- [14] K.-P. Ho and J. M. Kahn, “Channel capacity of WDM systems using constant-intensity modulation formats,” in *Proc. OFC/NFOEC*, Anaheim, CA, 2002, paper ThGG85.
- [15] L. G. Kazovsky, G. Kalogerakis, and W.-T. Shaw, “Homodyne phase-shift-keying systems: past challenges and future opportunities,” *J. Lightw. Technol.*, vol. 24, no. 12, pp. 4876–4884, Dec. 2006.
- [16] C. Berrou, A. Glavieux, and P. Thitimajshima, “Near Shannon limit error-correcting coding and decoding: turbo-codes,” in *Proc. ICC*, Geneva, Switzerland, 1993, pp. 1064–1070.
- [17] S.-Y. Chung, G. D. Forney, Jr., T. J. Richardson, and R. Urbanke, “On the design of low-density parity-check codes within 0.0045 db of the Shannon limit,” *IEEE Commun. Lett.*, vol. 5, no. 2, pp. 58–60, Feb. 2001.
- [18] C. Berrou, “The ten-year-old turbo codes are entering into service,” *IEEE Commun. Mag.*, vol. 41, no. 8, pp. 110–116, Aug. 2003.
- [19] E. Ip, J. M. Kahn, D. Anthon, and J. Hutchins, “Linewidth measurements of MEMS-based tunable lasers for phase-locking applications,” *IEEE Photon. Technol. Lett.*, vol. 17, no. 10, pp. 2029–2031, Oct. 2005.
- [20] Y. Han and G. Li, “Coherent optical communication using polarization multiple-input-multiple-output,” *Opt. Exp.*, vol. 13, no. 19, pp. 7527–7534, Sep. 2005.
- [21] M. A. Grant, W. C. Michie, and M. J. Fletcher, “The performance of optical phase-locked loops in the presence of nonnegligible loop propagation delay,” *J. Lightw. Technol.*, vol. 5, no. 4, pp. 592–597, Apr. 1987.
- [22] *Integrable Tunable Laser Assembly Multi Source Agreement*, Optical Internetworking Forum Std. OIF-ITLA-MSA-01.2, 2008.
- [23] F. M. Gardner, *Phaselock Techniques*, 3rd ed. New Jersey: John Wiley & Sons, 2005.
- [24] J. R. Barry and J. M. Kahn, “Carrier synchronization for homodyne and heterodyne detection of optical quadriphase-shift keying,” *J. Lightw. Technol.*, vol. 10, no. 12, pp. 1939–1951, Dec. 1992.

- [25] E. Ip and J. M. Kahn, “Carrier synchronization for 3- and 4-bit-per-symbol optical transmission,” *J. Lightw. Technol.*, vol. 23, no. 12, pp. 4110–4124, Dec. 2005.
- [26] S. Norimatsu and K. Iwashita, “Linewidth requirements for optical synchronous detection systems with nonnegligible loop delay time,” *J. Lightw. Technol.*, vol. 10, no. 3, pp. 341–349, Mar. 1992.
- [27] K.-Y. Kim and H.-J. Choi, “Design of carrier recovery algorithm for high-order QAM with large frequency acquisition range,” in *Proc. ICC*, Helsinki, Finland, 2001, pp. 1016–1020.
- [28] P. J. Winzer, A. H. Gnauck, C. R. Doerr, M. Magarini, and L. L. Buhl, “Spectrally efficient long-haul optical networking using 112-Gb/s polarization-multiplexed 16-QAM,” *J. Lightw. Technol.*, vol. 28, no. 4, pp. 547–556, Feb. 2010.
- [29] T. Kobayashi, A. Sano, H. Masuda, K. Ishihara, E. Yoshida, Y. Miyamoto, H. Yamazaki, and T. Yamada, “160-Gb/s polarization-multiplexed 16-QAM long-haul transmission over 3,123 km using digital coherent receiver with digital PLL based frequency offset compensator,” in *Proc. OFC/NFOEC*, San Diego, CA, 2010, paper OTuD1.
- [30] I. Fatadin, D. Ives, and S. J. Savory, “Compensation of frequency offset for differentially encoded 16- and 64-QAM in the presence of laser phase noise,” *IEEE Photon. Technol. Lett.*, vol. 22, no. 3, pp. 176–178, Feb. 2010.
- [31] F. Derr, “Coherent optical QPSK intradyne system: concept and digital receiver realization,” *J. Lightw. Technol.*, vol. 10, no. 9, pp. 1290–1296, Sep. 1992.
- [32] L. Kazovsky, S.-W. Wong, T. Ayhan, K. M. Albeyoglu, M. R. N. Ribeiro, and A. Shastri, “Hybrid optical-wireless access networks,” *Proc. IEEE*, vol. 100, no. 5, pp. 1197–1225, May 2012.
- [33] J. Capmany and D. Novak, “Microwave photonics combines two worlds,” *Nature Photon.*, vol. 1, pp. 319–330, Jun. 2007.
- [34] C. Lim, A. Nirmalathas, M. Bakaui, P. Gamage, K.-L. Lee, Y. Yang, D. Novak, and R. Waterhouse, “Fiber-wireless networks and subsystem technologies,” *J. Lightw. Technol.*, vol. 28, no. 4, pp. 390–405, Feb. 2010.
- [35] E. I. Ackerman and C. H. Cox, “RF fiber-optic link performance,” *IEEE Microw. Mag.*, vol. 2, no. 4, pp. 50–58, Dec. 2001.
- [36] M. D. Feuer, J. M. Wiesenfeld, J. S. Perino, C. A. Burrus, G. Raybon, S. C. Shunk, and N. K. Dutta, “Single-port laser-amplifier modulators for local access,” *IEEE Photon. Technol. Lett.*, vol. 8, no. 9, pp. 1175–1177, Sep. 1996.

Bibliography

- [37] Y. Takushima, K. Cho, and Y. Chung, “Design issues in RSOA-based WDM PON,” in *IEEE IPGC*, Singapore, Dec. 2008, pp. 1–4.
- [38] P. Chanclou, F. Payoux, T. Soret, N. Genay, R. Brenot, F. Blache, M. Goix, J. Landreau, O. Legouezigou, and F. Mallécot, “Demonstration of RSOA-based remote modulation at 2.5 and 5 Gbit/s for WDM PON,” in *Proc. OFC/NFOEC*, Anaheim, CA, 2007, paper OWD1.
- [39] G. de Valicourt, M. A. Violas, D. Wake, F. van Dijk, C. Ware, A. Enard, D. Make, Z. Liu, M. Lamponi, G.-H. Duan, and R. Brenot, “Radio-over-fiber access network architecture based on new optimized RSOA devices with large modulation bandwidth and high linearity,” *IEEE Trans. Microw. Theory Tech.*, vol. 58, no. 11, pp. 3248–3258, Nov. 2010.
- [40] Z. Liu, M. Sadeghi, G. de Valicourt, R. Brenot, and M. Violas, “Experimental validation of a reflective semiconductor optical amplifier model used as a modulator in radio over fiber systems,” *IEEE Photon. Technol. Lett.*, vol. 23, no. 9, pp. 576–578, May 2011.
- [41] Y.-Y. Won, H.-C. Kwon, and S.-K. Han, “1.25-Gb/s wavelength-division multiplexed single-wavelength colorless radio-on-fiber systems using reflective semiconductor optical amplifier,” *J. Lightw. Technol.*, vol. 25, no. 11, pp. 3472–3478, Nov. 2007.
- [42] X. Yu, T. B. Gibbon, and I. T. Monroy, “Bidirectional radio-over-fiber system with phase-modulation downlink and RF oscillator-free uplink using a reflective SOA,” *IEEE Photon. Technol. Lett.*, vol. 20, no. 24, pp. 2180–2182, Dec. 2008.
- [43] K. Y. Cho, A. Agata, Y. Takushima, and Y. C. Chung, “Chromatic dispersion tolerance of 10-Gb/s WDM PON implemented by using bandwidth-limited RSOAs,” in *Proc. OECC*, Hong Kong, China, 2009, paper TuH2.
- [44] H. Schmuck, “Comparison of optical millimetre-wave system concepts with regard to chromatic dispersion,” *Electron. Lett.*, vol. 31, no. 21, pp. 1848–1849, Oct. 1995.
- [45] U. Gliese, S. Nørskov, and T. N. Nielsen, “Chromatic dispersion in fiber-optic microwave and millimeter-wave links,” *IEEE Trans. Microw. Theory Tech.*, vol. 44, no. 10, pp. 1716–1724, Oct. 1996.
- [46] C. Arellano, K.-D. Langer, and J. Prat, “Reflections and multiple Rayleigh backscattering in WDM single-fiber loopback access networks,” *J. Lightw. Technol.*, vol. 27, no. 1, pp. 12–18, Jan. 2009.
- [47] G. J. Foschini, R. D. Gitlin, and S. B. Weinstein, “Optimization of two-dimensional signal constellations in the presence of Gaussian noise,” *IEEE Trans. Commun.*, vol. 22, no. 1, pp. 28–38, Jan. 1974.

- [48] W. Webb and L. Hanzo, *Modern Quadrature Amplitude Modulation: Principles and Applications for Fixed and Wireless Communications*. London, UK: Pentech Press, 1994.
- [49] H. Zhang, P.-Y. Kam, and C. Yu, “Optimal ring ratio of 16-star quadrature amplitude modulation in coherent optical communication systems,” in *Proc. OECC*, Kaohsiung, Taiwan, 2011, pp. 577–578.
- [50] C. R. Doerr, L. Zhang, P. J. Winzer, and A. H. Gnauck, “28-Gbaud InP square or hexagonal 16-QAM modulator,” in *Proc. OFC/NFOEC*, Los Angeles, CA, 2011, paper OMU2.
- [51] T. Pfau, S. Hoffmann, and R. Noe, “Hardware-efficient coherent digital receiver concept with feedforward carrier recovery for M -QAM constellations,” *J. Lightw. Technol.*, vol. 27, no. 8, pp. 989–999, Apr. 2009.
- [52] J. G. Proakis, *Digital Communications*, 5th ed. New York: McGraw-Hill, 2008.
- [53] W. J. Weber, “Differential encoding for multiple amplitude and phase shift keying systems,” *IEEE Trans. Commun.*, vol. 26, no. 3, pp. 385–391, Mar. 1978.
- [54] G. P. Agrawal, *Fiber-Optic Communication Systems*, 3rd ed. New York: John Wiley & Sons, 2002.
- [55] T. Miya, Y. Terunuma, T. Hosaka, and T. Miyashita, “Ultimate low-loss single-mode fibre at $1.55\text{ }\mu\text{m}$,” *Electron. Lett.*, vol. 15, no. 4, pp. 106–108, Feb. 1979.
- [56] M. Seimetz and C.-M. Weinert, “Options, feasibility, and availability of 2×4 90° hybrids for coherent optical systems,” *J. Lightw. Technol.*, vol. 24, no. 3, pp. 1317–1322, Mar. 2006.
- [57] A. Yariv, “Signal-to-noise considerations in fiber links with periodic or distributed optical amplification,” *Opt. Lett.*, vol. 15, no. 19, pp. 1064–1066, Oct. 1990.
- [58] O. Kharraz and D. Forsyth, “Performance comparisons between PIN and APD photodetectors for use in optical communication systems,” *Optik*, vol. 124, no. 13, pp. 1493–1498, Jul. 2013.
- [59] S. J. Savory, “Digital coherent optical receivers: algorithms and subsystems,” *IEEE J. Sel. Topics Quantum Electron.*, vol. 16, no. 5, pp. 1164–1179, Sep. 2010.
- [60] M. Taylor, “Coherent detection method using DSP for demodulation of signal and subsequent equalization of propagation impairments,” *IEEE Photon. Technol. Lett.*, vol. 16, no. 2, pp. 674–676, Feb. 2004.

Bibliography

- [61] F. M. Gardner, “A BPSK/QPSK timing-error detector for sampled receivers,” *IEEE Trans. Commun.*, vol. COM-34, no. 5, pp. 423–429, May 1986.
- [62] S. H. Chang, H. S. Chung, and K. Kim, “Digital non-data-aided symbol synchronization in optical coherent intradyne reception,” *Opt. Exp.*, vol. 16, no. 19, pp. 15 097–15 103, Sep. 2008.
- [63] M. Oerder and H. Meyr, “Digital filter and square timing recovery,” *IEEE Trans. Commun.*, vol. 36, no. 5, pp. 605–612, May 1988.
- [64] G. P. Agrawal, *Nonlinear Fiber Optics*, 3rd ed. San Diego, CA: Academic Press, 2001.
- [65] C. Yu, “Polarization mode dispersion monitoring,” in *Optical Performance Monitoring Techniques for Next Generation Photonic Networks*, 1st ed. Burlington, MA: Academic Press, 2010, ch. 4, pp. 101–126.
- [66] I. Fatadin, D. Ives, and S. Savory, “Blind equalization and carrier phase recovery in a 16-QAM optical coherent system,” *J. Lightw. Technol.*, vol. 27, no. 15, pp. 3042–3049, Aug. 2009.
- [67] H. Bülow, W. Baumert, H. Schmuck, F. Mohr, T. Schulz, F. Küppers, and W. Weiershausen, “Measurement of the maximum speed of PMD fluctuation in installed field fiber,” in *Proc. OFC/IOOC*, San Diego, CA, 1999, pp. 83 – 85 vol.2.
- [68] H. Bülow, “System outage probability due to first- and second-order PMD,” *IEEE Photon. Technol. Lett.*, vol. 10, no. 5, pp. 696–698, May 1998.
- [69] Z. Wang, C. Xie, and X. Ren, “PMD and PDL impairments in polarization division multiplexing signals with direct detection,” *Opt. Exp.*, vol. 17, no. 10, pp. 7993–8004, May 2009.
- [70] M. Kuschnerov, F. N. Hauske, K. Piyawanno, B. Spinnler, M. S. Alfiad, A. Napoli, and B. Lankl, “DSP for coherent single-carrier receivers,” *J. Lightw. Technol.*, vol. 27, no. 16, pp. 3614–3622, Aug. 2009.
- [71] S. J. Savory, “Digital filters for coherent optical receivers,” *Opt. Exp.*, vol. 16, no. 2, pp. 804–817, Jan. 2008.
- [72] E. Ip and J. M. Kahn, “Digital equalization of chromatic dispersion and polarization mode dispersion,” *J. Lightw. Technol.*, vol. 25, no. 8, pp. 2033–2043, Aug. 2007.
- [73] D. N. Godard, “Self-recovering equalization and carrier tracking in two-dimensional data communication systems,” *IEEE Trans. Commun.*, vol. 28, no. 11, pp. 1867–1875, Nov. 1980.

Bibliography

- [74] G. Goldfarb and G. Li, "Chromatic dispersion compensation using digital IIR filtering with coherent detection," *IEEE Photon. Technol. Lett.*, vol. 19, no. 13, pp. 969–971, Jul. 2007.
- [75] S. Tsukamoto, K. Katoh, and K. Kikuchi, "Unrepeated transmission of 20-Gb/s optical quadrature phase-shift-keying signal over 200-km standard single-mode fiber based on digital processing of homodyne-detected signal for group-velocity dispersion compensation," *IEEE Photon. Technol. Lett.*, vol. 18, no. 9, pp. 1016–1018, May 2006.
- [76] R. D. Gitlin and S. B. Weinstein, "Fractionally-spaced equalization: an improved digital transversal equalizer," *Bell Syst. Tech. J.*, vol. 60, no. 2, pp. 275–296, Feb. 1981.
- [77] S. U. H. Qureshi, "Adaptive equalization," *Proc. IEEE*, vol. 73, no. 9, pp. 1349–1387, Sep. 1985.
- [78] G. Ungerboeck, "Fractional tap-spacing equalizer and consequences for clock recovery in data modems," *IEEE Trans. Commun.*, vol. COM-24, no. 8, pp. 856–864, Aug. 1976.
- [79] Y. Atzmon and M. Nazarathy, "Laser phase noise in coherent and differential optical transmission revisited in the polar domain," *J. Lightw. Technol.*, vol. 27, no. 1, pp. 19–29, Jan. 2009.
- [80] P.-Y. Kam, S. S. Ng, and T. S. Ng, "Optimum symbol-by-symbol detection of uncoded digital data over the Gaussian channel with unknown carrier phase," *IEEE Trans. Commun.*, vol. 42, no. 8, pp. 2543–2552, Aug. 1994.
- [81] Y. Wang, E. Serpedin, and P. Ciblat, "Non-data aided feedforward estimation of PSK-modulated carrier frequency offset," in *Proc. ICC*, New York, NY, 2002, pp. 192–196.
- [82] Y. Wang, E. Serpedin, P. Ciblat, and P. Loubaton, "Non-data aided feedforward cyclostationary statistics based carrier frequency offset estimators for linear modulations," in *Proc. GLOBECOM'01*, Paris, France, 2001, pp. 1386–1390.
- [83] M. Selmi, Y. Jaouen, and P. Ciblat, "Accurate digital frequency offset estimator for coherent PolMux QAM transmission systems," in *Proc. ECOC*, Vienna, Austria, 2009, paper P3.08.
- [84] D. C. Rife and R. R. Boorstyn, "Single-tone parameter estimation from discrete-time observations," *IEEE Trans. Inf. Theory*, vol. IT-20, no. 5, pp. 591–598, Sep. 1974.
- [85] M. Morelli and U. Mengali, "Feedforward frequency estimation for PSK: a tutorial review," *Eur. Trans. Telecomm.*, vol. 9, no. 2, pp. 103–116, Mar./Apr. 1998.

- [86] J. C. I. Chuang and N. R. Sollenberger, “Burst coherent demodulation with combined symbol timing, frequency offset estimation, and diversity selection,” *IEEE Trans. Commun.*, vol. 39, no. 7, pp. 1157–1164, Jul. 1991.
- [87] A. Leven, N. Kaneda, U.-V. Koc, and Y.-K. Chen, “Frequency estimation in intradyne reception,” *IEEE Photon. Technol. Lett.*, vol. 19, no. 6, pp. 366–368, Mar. 2007.
- [88] I. Fatadin and S. J. Savory, “Compensation of frequency offset for 16-QAM optical coherent systems using QPSK partitioning,” *IEEE Photon. Technol. Lett.*, vol. 23, no. 17, pp. 1246–1248, Sep. 2011.
- [89] D. S. Ly-Gagnon, S. Tsukamoto, K. Katoh, and K. Kikuchi, “Coherent detection of optical quadrature phase-shift keying signals with carrier phase estimation,” *J. Lightw. Technol.*, vol. 24, no. 1, pp. 12–21, Jan. 2006.
- [90] U. Mengali and A. N. D’Andrea, *Synchronization Techniques for Digital Receivers*. New York: Plenum Press, 1997.
- [91] A. J. Viterbi and A. M. Viterbi, “Nonlinear estimation of PSK-modulated carrier phase with application to burst digital transmission,” *IEEE Trans. Inf. Theory*, vol. IT-29, no. 4, pp. 543–551, Jul. 1983.
- [92] I. Fatadin, D. Ives, and S. J. Savory, “Laser linewidth tolerance for 16-QAM coherent optical systems using QPSK partitioning,” *IEEE Photon. Technol. Lett.*, vol. 22, no. 9, pp. 631–633, May 2010.
- [93] S. K. Oh and S. P. Stapleton, “Blind phase recovery using finite alphabet properties in digital communications,” *Electron. Lett.*, vol. 33, no. 3, pp. 175–176, Jan. 1997.
- [94] F. Rice, B. Cowley, B. Moran, and M. Rice, “Cramér-Rao lower bounds for QAM phase and frequency estimation,” *IEEE Trans. Commun.*, vol. 49, no. 9, pp. 1582–1591, Sep. 2001.
- [95] P.-Y. Kam, “Maximum likelihood carrier phase recovery for linear suppressed-carrier digital data modulations,” *IEEE Trans. Commun.*, vol. COM-34, no. 6, pp. 522–527, Jun. 1986.
- [96] S. Zhang, P.-Y. Kam, C. Yu, and J. Chen, “Decision-aided carrier phase estimation for coherent optical communications,” *J. Lightw. Technol.*, vol. 28, no. 11, pp. 1597–1607, Jun. 2010.
- [97] R. D. Gaudenzi, T. Garde, and V. Vanghi, “Performance analysis of decision-directed maximum-likelihood phase estimators for M-PSK modulated signals,” *IEEE Trans. Commun.*, vol. 43, no. 12, pp. 3090–3100, Dec. 1995.

- [98] A. Meiyappan, P.-Y. Kam, and H. Kim, “Performance of decision-aided maximum-likelihood carrier phase estimation with frequency offset,” in *Proc. OFC/NFOEC*, Los Angeles, CA, 2012, paper OTu2G.6.
- [99] J. E. Volder, “The cordic trigonometric computing technique,” *IRE Trans. Electron. Comp.*, vol. EC-8, no. 3, pp. 330–334, Sep. 1959.
- [100] H. Zhang, S. Zhang, P.-Y. Kam, C. Yu, and J. Chen, “Optimized phase error tolerance of 16-star quadrature amplitude modulation in coherent optical communication systems,” in *Proc. OECC*, Sapporo, Japan, 2010, pp. 592–593.
- [101] G. J. Foschini, R. D. Gitlin, and S. B. Weinstein, “On the selection of a two-dimensional signal constellation in the presence of phase jitter and Gaussian noise,” *Bell Syst. Tech. J.*, vol. 52, no. 6, pp. 927–965, Feb. 1973.
- [102] S. Zhang, P.-Y. Kam, J. Chen, and C. Yu, “Bit-error rate performance of coherent optical M -ary PSK/QAM using decision-aided maximum likelihood phase estimation,” *Opt. Exp.*, vol. 18, no. 12, pp. 12 088–12 103, Jun. 2010.
- [103] A. Meiyappan, P.-Y. Kam, and H. Kim, “A complex-weighted, decision-aided, maximum-likelihood carrier phase and frequency-offset estimation algorithm for coherent optical detection,” *Opt. Exp.*, vol. 20, no. 18, pp. 20 102–20 114, Aug. 2012.
- [104] H. Meyr, M. Moeneclaey, and S. Fechtel, *Digital Communication Receivers: Synchronization, Channel Estimation and Signal Processing*. New York: John Wiley & Sons, 1997.
- [105] E. Ip and J. M. Kahn, “Addendum to ‘Feedforward carrier recovery for coherent optical communications’,” *J. Lightw. Technol.*, vol. 27, no. 13, pp. 2552–2553, Jul. 2009.
- [106] M. G. Taylor, “Phase estimation methods for optical coherent detection using digital signal processing,” *J. Lightw. Technol.*, vol. 27, no. 7, pp. 901–914, Apr. 2009.
- [107] M. Kuschnerov, K. Piyawanno, M. S. Alfiad, B. Spinnler, A. Napoli, and B. Lankl, “Impact of mechanical vibrations on laser stability and carrier phase estimation in coherent receivers,” *IEEE Photon. Technol. Lett.*, vol. 22, no. 15, pp. 1114–1116, Aug. 2010.
- [108] A. Meiyappan, P.-Y. Kam, and H. Kim, “Full-range and rapid-tracking carrier phase and frequency estimator for 16-QAM coherent systems,” in *Proc. OFC/NFOEC*, Anaheim, CA, 2013, paper OTu3I.4.
- [109] R. H. Walden, “Analog-to-digital converter survey and analysis,” *IEEE J. Sel. Areas Commun.*, vol. 17, no. 4, pp. 539–550, Apr. 1999.

Bibliography

- [110] P. Schvan, J. Bach, C. Falt, P. Flemke, R. Gibbins, Y. Greshishchev, N. Ben-Hamida, D. Pollex, J. Sitch, S.-C. Wang, and J. Wolczanski, “A 24GS/s 6b ADC in 90nm CMOS,” in *Proc. ISSCC Dig.Tech. Papers*, San Francisco, CA, 2008, pp. 544–634.
- [111] M. P. Fitz, “Planar filtered techniques for burst mode carrier synchronization,” in *Proc. GLOBECOM’91*, Phoenix, AZ, 1991, pp. 365–369.
- [112] E. B. Basch, R. Egorov, S. Gringeri, and S. Elby, “Architectural tradeoffs for reconfigurable dense wavelength-division multiplexing systems,” *IEEE J. Sel. Topics Quantum Electron.*, vol. 12, no. 4, pp. 615–626, Jul./Aug. 2006.
- [113] S. J. B. Yoo, “Optical packet and burst switching technologies for the future photonic internet,” *J. Lightw. Technol.*, vol. 24, no. 12, pp. 4468–4492, Dec. 2006.
- [114] O. Gerstel, M. Jinno, A. Lord, and S. J. B. Yoo, “Elastic optical networking: a new dawn for the optical layer?” *IEEE Commun. Mag.*, vol. 50, no. 2, pp. s12–s20, Feb. 2012.
- [115] S. Gringeri, N. Bitar, and T. J. Xia, “Extending software defined network principles to include optical transport,” *IEEE Commun. Mag.*, vol. 51, no. 3, pp. 32–40, Mar. 2013.
- [116] K. Roberts and C. Laperle, “Flexible transceivers,” in *Proc. ECOC*, Amsterdam, The Netherlands, 2012, paper We.3.A.3.
- [117] W.-R. Peng, I. Morita, and H. Tanaka, “Hybrid QAM transmission techniques for single-carrier ultra-dense WDM systems,” pp. 824–825, Jul. 2011.
- [118] Q. Zhuge, X. Xu, M. Morsy-Osman, M. Chagnon, M. Qiu, and D. V. Plant, “Time domain hybrid QAM based rate-adaptive optical transmissions using high speed DACs,” in *Proc. OFC/NFOEC*, Anaheim, CA, 2013, paper OTh4E.6.
- [119] F. Vacondio, O. Rival, Y. Pointurier, C. Simonneau, L. Lorcy, J.-C. Antona, and S. Bigo, “Coherent receiver enabling data rate adaptive optical packet networks,” in *Proc. ECOC*, Geneva, Switzerland, 2011, paper Mo.2.A.4.
- [120] D. van den Borne, C. R. S. Fludger, T. Duthel, T. Wuth, E. D. Schmidt, C. Schulien, E. Gottwald, G. D. Khoe, and H. de Waardt, “Carrier phase estimation for coherent equalization of 43-Gb/s POLMUX-NRZ-DQPSK transmission with 10.7-Gb/s NRZ neighbours,” in *Proc. ECOC*, Berlin, Germany, 2007, paper 7.2.3.
- [121] M. Seimetz, “Laser linewidth limitations for optical systems with high-order modulation employing feed forward digital carrier phase estimation,” in *Proc. OFC/NFOEC*, San Diego, CA, 2008, paper OTuM2.

Bibliography

- [122] G. Goldfarb and G. Li, “BER estimation of QPSK homodyne detection with carrier phase estimation using digital signal processing,” *Opt. Exp.*, vol. 14, no. 18, pp. 8043–8053, Jul. 2006.
- [123] P.-Y. Kam, K. H. Chua, and X. Yu, “Adaptive symbol-by-symbol reception of MPSK on the Gaussian channel with unknown carrier phase characteristics,” *IEEE Trans. Commun.*, vol. 46, no. 10, pp. 1275–1279, Oct. 1998.
- [124] A. Meiyappan, P.-Y. Kam, and H. Kim, “On decision aided carrier phase and frequency offset estimation in coherent optical receivers,” *J. Lightw. Technol.*, vol. 31, no. 13, pp. 2055–2069, Jul. 2013.
- [125] *Forward Error Correction for High Bit-Rate DWDM Submarine Systems*, International Telecommunication Union Std. ITU-T Recommendation G.975.1, 2004.
- [126] T. Mizuochi, “Recent progress in forward error correction and its interplay with transmission impairments,” *IEEE J. Sel. Topics Quantum Electron.*, vol. 12, no. 4, pp. 544–554, Jul./Aug. 2006.
- [127] F. Yu, N. Stojanovic, F. N. Hauske, D. Chang, Z. Xiao, G. Bauch, D. Pflueger, C. Xie, Y. Zhao, L. Jin, Y. Li, L. Li, X. Xu, and Q. Xiong, “Soft-decision LDPC turbo decoding for DQPSK modulation in coherent optical receivers,” in *Proc. ECOC*, Geneva, Switzerland, 2011, paper We.10.P1.70.
- [128] A. Bisplinghoff, S. Langenbach, T. Kupfer, and B. Schmauss, “Turbo differential decoding failure for a coherent phase slip channel,” in *Proc. ECOC*, Amsterdam, The Netherlands, 2012, paper Mo.1.A.5.
- [129] J. P. Gordon and L. F. Mollenauer, “Phase noise in photonic communications systems using linear amplifiers,” *Opt. Lett.*, vol. 15, no. 23, pp. 1351–3, Dec. 1990.
- [130] K.-P. Ho and J. M. Kahn, “Electronic compensation technique to mitigate nonlinear phase noise,” *J. Lightw. Technol.*, vol. 22, no. 3, pp. 779–783, Mar. 2004.
- [131] H. Kim and A. H. Gnauck, “Experimental investigation of the performance limitation of DPSK systems due to nonlinear phase noise,” *IEEE Photon. Technol. Lett.*, vol. 15, no. 2, pp. 320–322, Feb. 2003.
- [132] E. Ip and J. M. Kahn, “Compensation of dispersion and nonlinear impairments using digital backpropagation,” *J. Lightw. Technol.*, vol. 26, no. 20, pp. 3416–3425, Oct. 2008.
- [133] K. Y. Cho, Y. Takushima, and Y. C. Chung, “10-Gb/s operation of RSOA for WDM PON,” *IEEE Photon. Technol. Lett.*, vol. 20, no. 18, pp. 1533–1535, Sep. 2008.

Bibliography

- [134] K. Y. Cho, A. Agata, Y. Takushima, and Y. C. Chung, “FEC optimization for 10-Gb/s WDM PON implemented by using bandwidth-limited RSOA,” in *Proc. OFC/NFOEC*, San Diego, CA, 2009, paper OMN5.
- [135] G. H. Smith, D. Novak, and Z. Ahmed, “Overcoming chromatic-dispersion effects in fiber-wireless systems incorporating external modulators,” *IEEE Trans. Microw. Theory Tech.*, vol. 45, no. 8, pp. 1410–1415, Aug. 1997.
- [136] H. Kim, “EML-based optical single sideband transmitter,” *IEEE Photon. Technol. Lett.*, vol. 20, no. 4, pp. 243–245, Feb. 2008.
- [137] H. Kim, “10-Gb/s operation of RSOA using a delay interferometer,” *IEEE Photon. Technol. Lett.*, vol. 22, no. 18, pp. 1379–1381, Sep. 2010.
- [138] C. R. Doerr, S. Chandrasekhar, P. J. Winzer, A. R. Chraplyvy, A. H. Gnauck, L. W. Stulz, R. Pafchek, and E. Burrows, “Simple multichannel optical equalizer mitigating intersymbol interference for 40-Gb/s nonreturn-to-zero signals,” *J. Lightw. Technol.*, vol. 22, no. 1, pp. 249–256, Jan. 2004.
- [139] H. Kim, “Transmission of 10-Gb/s directly modulated RSOA signals in single-fiber loopback WDM PONs,” *IEEE Photon. Technol. Lett.*, vol. 23, no. 14, pp. 965–967, Jul. 2011.
- [140] I. Papagiannakis, M. Omella, D. Klonidis, A. N. Birbas, J. Kikidis, I. Tomkos, and J. Prat, “Investigation of 10-Gb/s RSOA-based upstream transmission in WDM-PONs utilizing optical filtering and electronic equalization,” *IEEE Photon. Technol. Lett.*, vol. 20, no. 24, pp. 2168–2170, Dec. 2008.
- [141] N. Henmi, T. Saito, and T. Ishida, “Prechirp technique as a linear dispersion compensation for ultrahigh-speed long-span intensity modulation directed detection optical communication systems,” *J. Lightw. Technol.*, vol. 12, no. 10, pp. 1706–1719, Oct. 1994.
- [142] Z. Rizou, K. Zoiros, and M. Connelly, “Modelling of semiconductor optical amplifier chirp compensation using optical delay interferometer,” in *Proc. NUSOD*, Rome, Italy, 2011, pp. 89–90.
- [143] M. Fujiwara, J.-I. Kani, H. Suzuki, and K. Iwatsuki, “Impact of backreflection on upstream transmission in WDM single-fiber loopback access networks,” *J. Lightw. Technol.*, vol. 24, no. 2, pp. 740–746, Feb. 2006.
- [144] A. Chiuchiarelli, M. Presi, R. Proietti, G. Contestabile, P. Choudhury, L. Giorgi, and E. Ciaramella, “Enhancing resilience to Rayleigh crosstalk by means of line coding and electrical filtering,” *IEEE Photon. Technol. Lett.*, vol. 22, no. 2, pp. 85–87, Jan. 2010.

Bibliography

- [145] F. Devaux, Y. Sorel, and J. F. Kerdiles, “Simple measurement of fiber dispersion and of chirp parameter of intensity modulated light emitter,” *J. Lightw. Technol.*, vol. 11, no. 12, pp. 1937–1940, Dec. 1993.
- [146] T. Fujiwara and K. Kikushima, “Power penalty dependency on sideband suppression ratio in optical SSB signal transmission,” in *Proc. OECC*, Yokohama, Japan, 2007, paper 11A2-2.
- [147] H. Takara, A. Sano, T. Kobayashi, H. Kubota, H. Kawakami, A. Matsuura, Y. Miyamoto, Y. Abe, H. Ono, K. Shikama, Y. Goto, K. Tsujikawa, Y. Sasaki, I. Ishida, K. Takenaga, S. Matsuo, K. Saitoh, M. Koshiba, and T. Morioka, “1.01-Pb/s (12 SDM/222 WDM/456 Gb/s) crosstalk-managed transmission with 91.4-b/s/Hz aggregate spectral efficiency,” in *Proc. ECOC*, Amsterdam, The Netherlands, 2012, paper Th.3.C.1.
- [148] R.-J. Essiambre, R. Ryf, N. K. Fontaine, and S. Randel, “Breakthroughs in photonics 2012: space-division multiplexing in multimode and multicore fibers for high-capacity optical communication,” *IEEE Photon. J.*, vol. 5, no. 2, p. 0701307, Apr. 2013.
- [149] S. Randel, R. Ryf, A. Sierra, P. J. Winzer, A. H. Gnauck, C. A. Bolle, R.-J. Essiambre, D. W. Peckham, A. McCurdy, and R. Lingle, Jr., “ 6×56 -Gb/s mode-division multiplexed transmission over 33-km few-mode fiber enabled by 6×6 MIMO equalization,” *Opt. Exp.*, vol. 19, no. 17, pp. 16 697–16 707, Aug. 2011.
- [150] A. Meiyappan, H. Kim, and P.-Y. Kam, “A low-complexity, low-cycle-slip-probability, format-independent carrier estimator with adaptive filter length,” *J. Lightw. Technol.*, vol. 31, no. 23, pp. 3806–3812, Dec. 2013.
- [151] M. D. Feuer, L. E. Nelson, X. Zhou, S. L. Woodward, R. Isaac, B. Zhu, T. F. Taunay, M. Fishteyn, J. M. Fini, and M. F. Yan, “Joint digital signal processing receivers for spatial superchannels,” *IEEE Photon. Technol. Lett.*, vol. 24, no. 21, pp. 1957–1960, Nov. 2012.
- [152] R. G. H. van Uden, C. M. Okonkwo, V. A. J. M. Sleiffer, M. Kuschnerov, H. de Waardt, and A. M. J. Koonen, “Single DPPLL joint carrier phase compensation for few-mode fiber transmission,” *IEEE Photon. Technol. Lett.*, vol. 25, no. 14, pp. 1381–1384, Jul. 2013.
- [153] J. Vuong, P. Ramantanis, A. Seck, D. Bendimerad, and Y. Frignac, “Understanding discrete linear mode coupling in few-mode fiber transmission systems,” in *Proc. ECOC*, Geneva, Switzerland, 2011, paper Tu.5.B.2.
- [154] E. M. Ip and J. M. Kahn, “Fiber impairment compensation using coherent detection and digital signal processing,” *J. Lightw. Technol.*, vol. 28, no. 4, pp. 502–519, Feb. 2010.

Bibliography

- [155] E. Saygun and C. L. Nikias, "Blind equalization with gradually increasing filter length (GRINFIL)," in *Proc. Asilomar Conf. SSC*, Pacific Grove, CA, 1996, pp. 263–266.
- [156] F. Riera-Palou, J. M. Noras, and D. G. M. Cruickshank, "Linear equalisers with dynamic and automatic length selection," *Electron. Lett.*, vol. 37, no. 25, pp. 1553–1554, Dec. 2001.
- [157] M. Zeller, L. A. Azpicueta-Ruiz, and W. Kellermann, "Adaptive FIR filters with automatic length optimization by monitoring a normalized combination scheme," in *Proc. IEEE WASPAA*, New Paltz, NY, 2009, pp. 149–152.
- [158] Y. Gong and C. F. N. Cowan, "An LMS style variable tap-length algorithm for structure adaptation," *IEEE Trans. Signal Process.*, vol. 53, no. 7, pp. 2400–2407, Jul. 2005.
- [159] S. Haykin, *Adaptive Filter Theory*, 4th ed. New Jersey: Prentice Hall, 2002.
- [160] B. M. Haas and T. E. Murphy, "A simple, linearized, phase-modulated analog optical transmission system," *IEEE Photon. Technol. Lett.*, vol. 19, no. 10, pp. 729–731, May 2007.
- [161] T. R. Clark and M. L. Dennis, "Coherent optical phase-modulation link," *IEEE Photon. Technol. Lett.*, vol. 19, no. 16, pp. 1206–1208, Aug. 2007.
- [162] V. J. Urick, F. Bucholtz, P. S. Devgan, J. D. McKinney, and K. J. Williams, "Phase modulation with interferometric detection as an alternative to intensity modulation with direct detection for analog-photonic links," *IEEE Trans. Microw. Theory Tech.*, vol. 55, no. 9, pp. 1978–1985, Sep. 2007.
- [163] R. F. Kalman, J. C. Fan, and L. G. Kazovsky, "Dynamic range of coherent analog fiber-optic links," *J. Lightw. Technol.*, vol. 12, no. 7, pp. 1263–1277, Jul. 1994.
- [164] T. K. Fong, D. J. M. Sabido IX, R. F. Kalman, M. Tabara, and L. G. Kazovsky, "Linewidth-insensitive coherent AM optical links: design, performance, and potential applications," *J. Lightw. Technol.*, vol. 12, no. 3, pp. 526–534, Mar. 1994.
- [165] A. Caballero, D. Zibar, and I. T. Monroy, "Performance evaluation of digital coherent receivers for phase-modulated radio-over-fiber links," *J. Lightw. Technol.*, vol. 29, no. 21, pp. 3282–3292, Nov. 2011.
- [166] D. Zibar, X. Yu, C. Peucheret, P. Jeppesen, and I. T. Monroy, "Digital coherent receiver for phase-modulated radio-over-fiber optical links," *IEEE Photon. Technol. Lett.*, vol. 21, no. 3, pp. 155–157, Feb. 2009.

Bibliography

- [167] D. H. Brandwood, “A complex gradient operator and its application in adaptive array theory,” *IEE Proc., Parts F and H*, vol. 130, no. 1, pp. 11–16, Feb. 1983.
- [168] M. H. Hayes, *Statistical Digital Signal Processing and Modeling*. New York: John Wiley & Sons, 1996.

List of Publications

Journal Papers

1. *Adaickalavan Meiyappan*, Hoon Kim, and Pooi-Yuen Kam, “A low-complexity, low-cycle-slip-probability, format-independent carrier estimator with adaptive filter length,” *J. Lightw. Technol.*, vol. 31, no. 23, pp. 3806–3812, Dec. 2013.
2. *Adaickalavan Meiyappan*, Pooi-Yuen Kam, and Hoon Kim, “On decision aided carrier phase and frequency offset estimation in coherent optical receivers,” *J. Lightw. Technol.*, vol. 31, no. 13, pp. 2055–2069, Jul. 2013.
3. *Adaickalavan Meiyappan*, Pooi-Yuen Kam, and Hoon Kim, “A complex-weighted, decision-aided, maximum-likelihood carrier phase and frequency-offset estimation algorithm for coherent optical detection,” *Opt. Exp.*, vol. 20, no. 18, pp. 20102–20114, Aug. 2012.
4. *Adaickalavan Meiyappan*, Pooi-Yuen Kam, and Hoon Kim, “6-GHz radio-over-fiber upstream transmission using a directly modulated RSOA,” *IEEE Photon. Technol. Lett.*, vol. 23, no. 22, pp. 1730–1732, Nov. 2011.

Conference Papers

1. *Adaickalavan Meiyappan*, Pooi-Yuen Kam, and Hoon Kim, “A low-complexity carrier phase and frequency offset estimator with adaptive filter length for coherent receivers,” in *Proc. ECOC*, London, UK, 2013, paper P.3.6.
2. *Adaickalavan Meiyappan*, Pooi-Yuen Kam, and Hoon Kim, “Full-range and rapid-tracking carrier phase and frequency estimator for 16-QAM coherent systems,” in *Proc. OFC/NFOEC*, Anaheim, CA, 2013, paper OTu3I.4.
3. *Adaickalavan Meiyappan*, Pooi-Yuen Kam, and Hoon Kim, “Complex decision-aided maximum-likelihood phase noise and frequency offset compensation for coherent optical receivers,” in *Proc. ECOC*, Amsterdam, The Netherlands, 2012, paper P3.02.
4. *Adaickalavan Meiyappan*, Pooi-Yuen Kam, and Hoon Kim, “Performance of decision-aided maximum-likelihood carrier phase estimation with frequency offset,” in *Proc. OFC/NFOEC*, Los Angeles, CA, 2012, paper OTu2G.6.